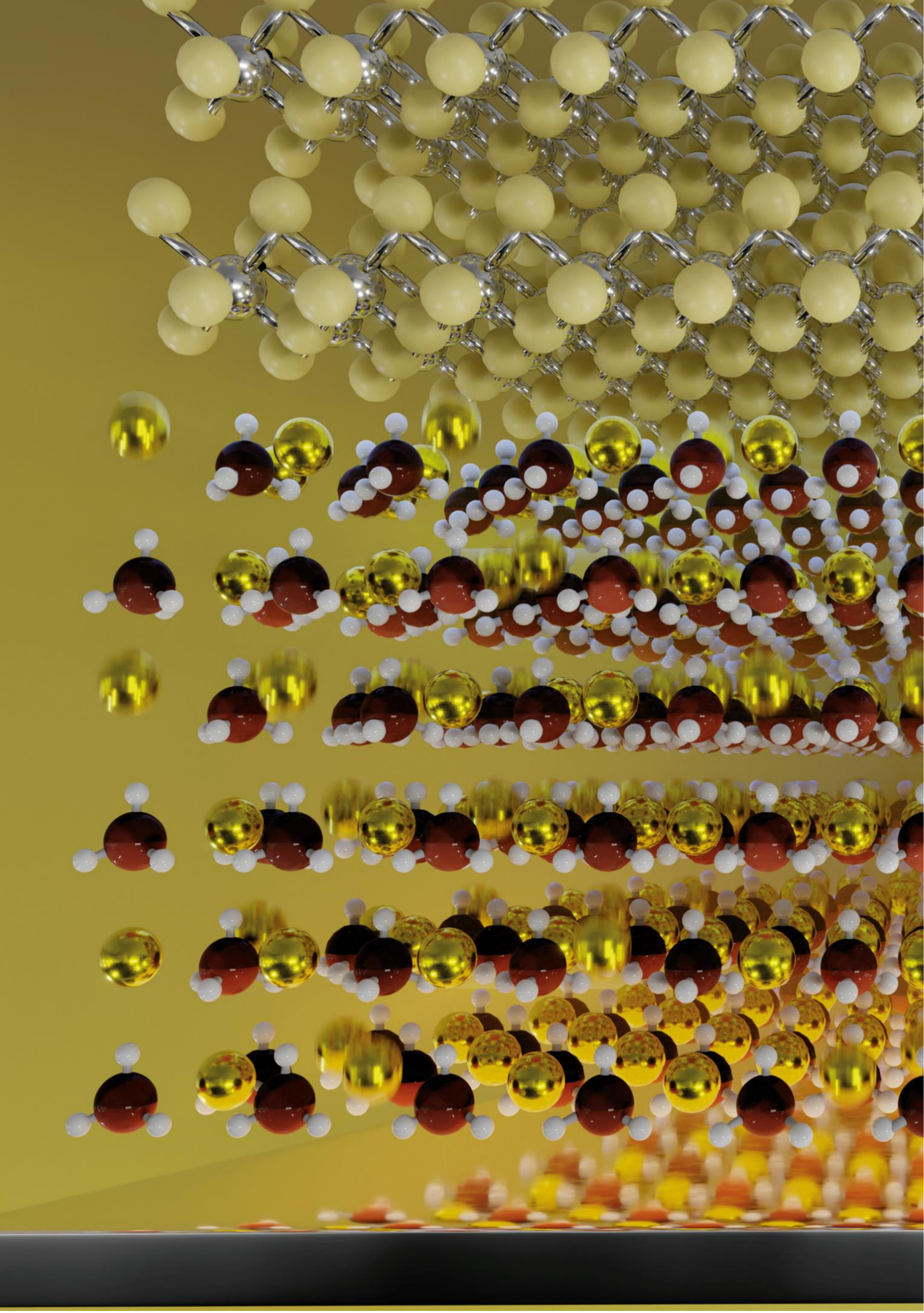

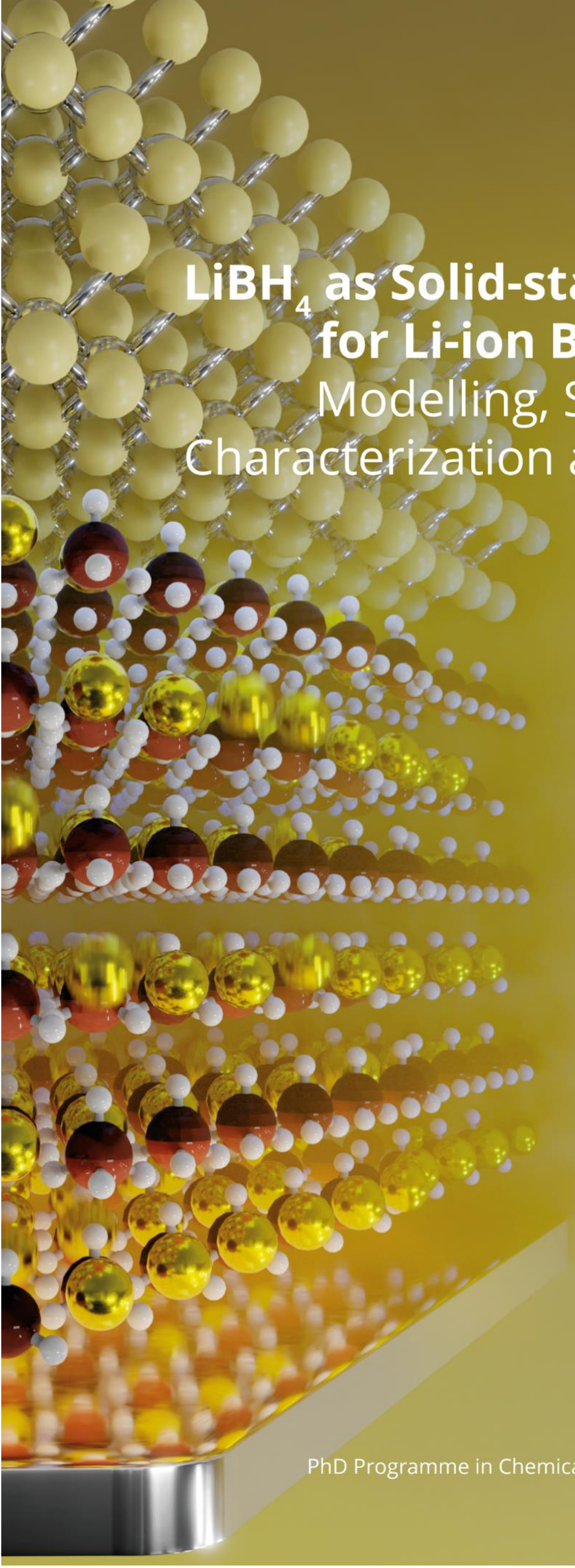

$LiBH_4$ as Solid-state Electrolyte for Li-ion Batteries:
Modelling, Synthesis, Characterization and Application

Valerio Gulino
Supervisor: Marcello Baricco

Università degli Studi di Torino
PhD Programme in Chemical and Materials Sciences XXXIII Cycle

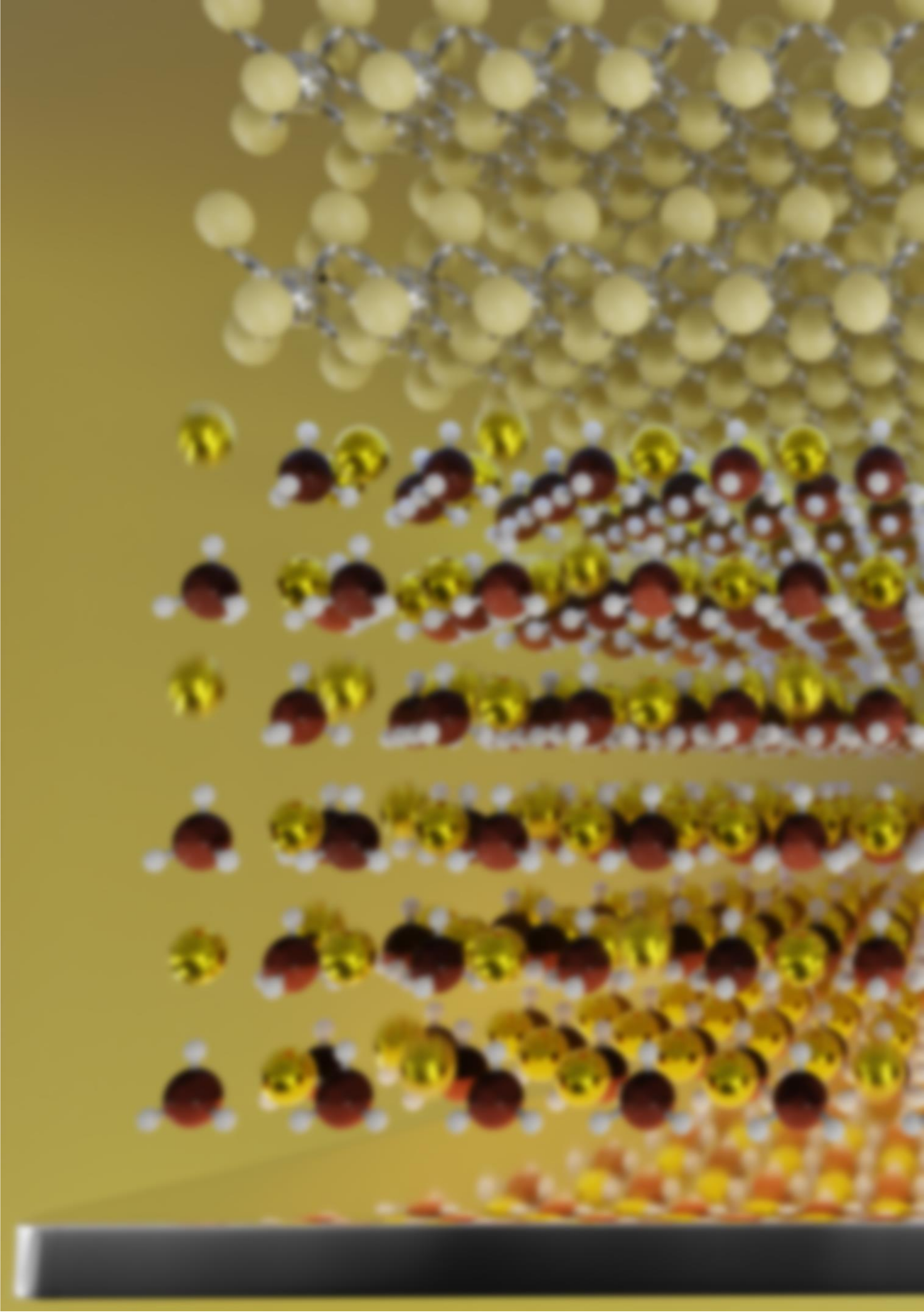

Università degli Studi di Torino

Doctoral School of the University of Torino

PhD Programme in Chemical and Materials Sciences XXXIII cycle

$LiBH_4$ as solid-state electrolyte for Li-ion batteries: modelling, synthesis, characterization and application

Candidate: Valerio Gulino

Supervisor: Prof. Marcello Baricco

Jury Members:
Prof. Peter Ngene
University of Utrecht
Inorganic Chemistry and Catalysis, Debye Institute for Nanomaterials Science
Prof. Mauro Sgori
Fiat Research Center
Group Materials Labs, Environment & Chemical Analysis, Innovation Aftertreatment & Batteries
Prof. Carlo Nervi
University of Turin
Department of Chemistry

Head of the Doctoral School: Prof. Alberto Rizzuti
PhD Programme Coordinator: Prof. Bartolomeo Civalleri

Torino, 09-10-2020

Table of content

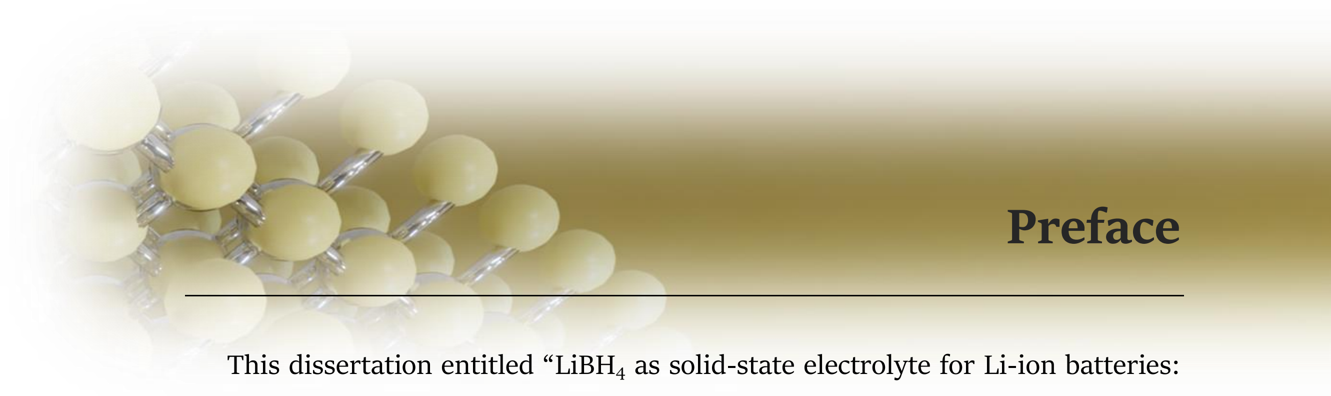

Preface

This dissertation entitled “$LiBH_4$ as solid-state electrolyte for Li-ion batteries: modelling, synthesis, characterization and application” has been submitted to the Doctoral School of the University of Torino at the University of Turin to fulfil the requirements for obtaining the PhD degree in Chemical and Material Science.

The results presented in this dissertation were obtained in the last 3 years as a PhD student of the XXXIII cycle (from October 2017 to September 2020) in the Metallurgy research group, under the supervision of Prof. Marcello Baricco, at the Department of Chemistry and NIS centre at the University of Turin.

In the beginning, PhD courses, schools, seminars, workshops and conferences attended, together with teaching activities, periods abroad, publications, oral and poster presentation presented during these 3 years are reported in a short bullet-point overview.

Chapter 1 introduces the field of energy storage in all-solid-state Li-ion batteries, and the motivation and goals of these thesis is presented.

Chapter 2 summaries the experimental and theoretical methods used in this thesis.

Chapter 3-8 contains the main results obtained during the PhD. The discussions and conclusions of the results are reported for each Chapter.

Chapter 3 is aimed to collect electrochemical characterizations of $LiBH_4$, reported in literature, and perform a statistical analysis.

Chapter 4 presents the results collected in order to define the $LiBH_4$-LiBr phase diagram.

Chapter 5 is aimed to explore the structural and electrochemical proprieties of the $LiBH_4$-LiBr-LiCl ternary system.

In **Chapter 6**, the effect of adding oxides to the $LiBH_4$ on the Li-ion conductivity of the mixture is presented

Chapter 7 shows the results collected in order to understand if is present a synergetic effect between adding halide and oxide to the $LiBH_4$.

Finally, **Chapter 8** reports the results of the incorporation of a synthetized solid-state electrolyte in a all-solid-state Li-ion battery.

Conclusions of this thesis are reported in the final **Chapter 9**.

PhD activities

Papers

I. Gulino, V.; Brighi, M.; Dematteis, E. M.; Murgia, F.; Nervi, C.; Černý, R.; Baricco, M. Phase Stability and Fast Ion Conductivity in the Hexagonal LiBH$_4$–LiBr–LiCl Solid Solution. *Chem. Mater.* 2019, *31* (14), 5133–5144. https://doi.org/10.1021/acs.chemmater.9b01035.

II. Gulino, V.; Barberis, L.; Ngene, P.; Baricco, M.; de Jongh, P. E. Enhancing Li-Ion Conductivity in LiBH$_4$-Based Solid Electrolytes by Adding Various Nanosized Oxides. *ACS Appl. Energy Mater.* 2020, *3* (5), 4941–4948. https://doi.org/10.1021/acsaem.9b02268.

III. Gulino, V.; Wolczyk, A.; Golov, A. A.; Eremin, R. A.; Palumbo, M.; Nervi, C.; Blatov, V. A.; Proserpio, D. M.; Baricco, M. Combined DFT and Geometrical–Topological Analysis of Li-Ion Conductivity in Complex Hydrides. *Inorg. Chem. Front.* 2020, *7* (17), 3115–3125. https://doi.org/10.1039/D0QI00577K.

IV. Gulino, V.; Brighi, M.; Murgia, F.; Ngene, P.; de Jongh, P. E.; Černý, R.; Baricco, M. Room temperature Solid-State Lithium-ion Battery using LiBH$_4$-MgO composite Electrolyte. *ACS Appl. Material & Interfaces*. submitted.

Talks

Presenting author is underlined.

I. Gulino V. - “Development of solid-state Li-ion conductor by investigation the change in crystalline structure” - Annual Metallurgy Group Lab. Meeting, Italy, Vaie (TO), 13/07/2018.

II. Gulino V. - “Development of solid-state Li-ion conductor by increasing the Li-ion conductivity of $LiBH_4$” - Annual Metallurgy Group Lab. Meeting, Italy, Vaie (TO), 17/07/2019.

III. M. Baricco, E.M. Dematteis, V. Gulino, J. Barale, N. Berti, C. Nervi, P. Rizzi “Complex hydride for energy storage” - AIMAT-INSTM 2019, Italy, Ischia (NA), 21-24/07/2019.

IV. Gulino V. – “Phase Stability and Fast Ion Conductivity in the Hexagonal $LiBH_4$–LiBr–LiCl Solid Solution” – EMRF (European Matrials Research Society) Fall Meeting 2019, Warsaw, Poland, 17/09/2019.

V. Gulino V. – “Development of novel solid-state Li-ion conductors by increasing the Li-ion conductivity of $LiBH_4$” – 2nd year PhD presentations, Turin, University of Turin, Department of Chemistry, Italy, 26/09/2019.

VI. Gulino V. – “Complex Hydrides as Solid-State Electrolyte for Li-ion Batterie” – Metallurgy Seminar, Turin, University of Turin, Department of Chemistry, Italy, 26/09/2019.

VII. E.Dematteis, V.Gulino, C.Nervi, M.Baricco – “Miscibility in $LiBH_4$” – 1st Int. Symposium "Hydrogenomics" combined with 14th Int. Symposium Hydrogen & Energy, Sapporo, Hokkaido, Japan, 2020, 5-10/01/2020.

Posters

Presenting author is underlined.

I. Gulino V., Dematteis E.M., Wolczyk A.R., Chierotti M., Nervi C., Baricco M. - “*Development of solid-state electrolytes by anion substitutions in lithium borohydride*” - Giornate dell’elettrochimica italiana GEI 2018, Italy, Sestriere (TO), 21-25/01/2018.

II. Gulino V., Dematteis E.M., Nervi C., Baricco M. - “*Development of solid-state electrolytes by anion substitutions in lithium borohydride*” - 1st International Symposium on Solid State Batteries, Switzerland, Dübendorf, EMPA, 28-29/05/2018.

III. Dematteis E.M., Gulino V., Santoru A., Pistidda C., Dornheim M., Baricco, M. - “*Solubility in Borohydrides: Role of Thermal Treatment in Mechanochemistry*” - 1st Workshop on Mechanochemistry of Metal Hydride, Norway, Oslo, University of Oslo, 30/05-01/06/2018.

IV. Dematteis E.M., Gulino V., Scaglione F., Santoru A., Pistidda C., Dornheim M., Nervi C., Baricco M. - “*Solubility in nanostructured Borohydrides prepared by Mechanochemistry*” - NanoInnovation Materiali Nanofasici 2018, Italy, Rome, 11-14/09/2018.

V. Gulino V., Brighi M., Dematteis E.M., Murgia F., Nervi C., Černý R., Baricco M. - “*Phase Stability and Fast Ion Conductivity in the Hexagonal $LiBH_4$–LiBr–LiCl Solid Solution*” - Gordon Research Seminar on Hydrogen-Metal System 2019, Spain, Barcellona, 02-03/06/2019.

VI. Gulino V., Brighi M., Dematteis E.M., Murgia F., Nervi C., Černý R., Baricco M. - “*Sviluppo di nuovi elettroliti solidi attraverso la sostituzione anionica nel litio boroidruro*” - Chimica Passione Periodica, Italy, Torino, University of Turi, 05/10/2019.

VII. Gulino V., Barberis L., Ngene P., Baricco M., de Jongh P.E. - “*Enhancement of the Li-ion Conductivity of $LiBH_4$ by mixing with Different Oxides*” - 2st Swiss & Surrounding Battery Days, Switzerland, Dübendorf, EMPA, 26-28/08/2019.

VIII. Gulino V., Barberis L., Ngene P., Baricco M., de Jongh P.E. - “*Enhancement of the Li-ion Conductivity of $LiBH_4$ by mixing with Different Oxides*” - EMRF (European Matrials Research Society) Fall Meeting 2019, Warsaw, Poland, 17/09/2019.

Award: Best Poster Presentation at Symposium Q.

IX. Gulino V., de Jongh P.E., Černý R., Baricco M. - “*Hydride as Solid-State Electrolyte for Li-ion Batteries*” - EIT Raw Materials Expert Forum on Sustainable Materials for Future Mobility, Turin, Italy, 07-09/10/2019.

Periods Abroad

- 07/07/2018-20/07/2018 Switzerland, Genève, Université de Genève, Laboratoire de Cristallographie, DQMP. Supervisor: Prof. Radovan Černý.
- 06/03/2019-10/06/2019 The Netherlands, Utrecht, Utrecht University, Inorganic Chemistry and Catalysis, Debye Institute for Nanomaterials Science. Supervisor: Prof Petra E. de Jongh, Dr. Peter Ngene
- 01/12/2019-15/12/2019 Switzerland, Genève, Université de Genève, Laboratoire de Cristallographie, DQMP. Supervisor: Prof. Radovan Černý.

Conferences Attended

- International Hydrogen Energy Agency meeting (IHEA), TASK32 - Italy, San Servolo (VE), 15-18/04/2018, 4days.
- 1st International Symposium on Solid State Batteries - Switzerland, Dübendorf, EMPA, 28-29/05/2018, 2 days.
- Gordon Research Seminar on Hydrogen-Metal System 2019 - Spain, Barcellona, 02-03/06/2019, 2 days.
- 2nd Swiss & Surrounding Battery Day - Switzerland, Dübendorf, EMPA, 26-28/08/2019, 3 days.
- EMRS Fall meeting 2019 - Warsaw, Poland, 16-19/09/2019, **4 days**.

  Finalist for the Graduate Student Award Symposium L

  Award: Graduated Student Award Symposium Q
- EIT Raw Materials Expert Forum on Sustainable Materials for Future Mobility - Turin, Italy, 07-09/10/2019, **3 days**.

PhD Courses and Schools Attended

- "*Solid State NMR: Basics and applications*", Roberto Gobetto, Michele Remo Chierotti, University of Turin, Department of Chemistry, 2018.
- "*CrisDi School: X RAYS diffractions*", Alessandro Pavese, University of Turin, Department of Chemistry, 2018.

- "*CrisDi School: X RAYS diffractions methods: Polyctistalline*", Marco Milanesio, University of Turin, Department of Chemistry, 2018.
- "*CrisDi School: The Rietveld method*", Angelo Agostino, University of Turin, Department of Chemistry, 2018.
- "*CrisDi School: In situ non-ambient conditions by single crystal XR diffraction: Polyctistalline*", Fernando Camara, University of Turin, Department of Chemistry, 2018.
- "*CrisDi School: Inorganic crystallochemistry*", Rossella Arletti, University of Turin, Department of Chemistry, 2018.
- "*CrisDi School: In situ/operando XRAY powder diffraction*", Rossella Arletti, University of Turin, Department of Chemistry, 2018.
- "*CrisDi School: Pair distribution functional analysis of complex, disorder and amorphous materials from total scattering data*", Monica Dapiaggi, University of Turin, Department of Chemistry, 2018.
- "*CrisDi School: Crystal growth beginners*", Linda Pastero, University of Turin, Department of Chemistry, 2018.
- "*Optimization and computation of thermodynamic proprieties and phase diagrams*", Marcello Baricco, University of Turin, Department of Chemistry, 2018.
- "*Electrochemical energy storage and conversion systems*", Mauro Sgroi, University of Turin, Department of Chemistry, 2018.
- "*Introduction to Scientific programming (in Python)*", Alessandro Erba, University of Turin, Department of Chemistry, 2018.
- "*Raman Day*", University of Turin, Department of Chemistry, 2018.

Seminars, Workshops Attended

- 2nd year PhD presentations, Italy, Turin, University of Turin, Department of Chemistry, 25/09/2017.

- "Biosensors and Catalysis: Applications of Nanoporous Gold"– Federico Scaglione, Italy, Turin, University of Turin, Department of Chemistry, 20/11/2017.
- "Trasferimento di Conoscenza ed Imprenditorialità come evoluzione della propria ricerca: dall'idea al Business Plan", Italy, Turin, Biblioteca Arturo Graf, 21/11/2018.
- "Recent advances in biosensor technologies", NIS Colloquium, Italy, Turin, University of Turin, Department of Chemistry, 22/11/2017.
- "Gender equality: don't change women, change the system", Italy, Turin, University of Turin, Department of Chemistry 24/11/2017.
- "A step-by-step approach to heterogeneous catalysts for olefin conversion", Alessando Piovano, Italy, Turin, University of Turin, Department of Chemistry, 04/12/2017.
- "Chemical Journeys", Italy, Turin, University of Turin, Department of Chemistry, 22/12/2017.
- "Effect of different processing routes on the properties of thermoelectric materials", Francesco Aversano, Italy, Turin, University of Turin, Department of Chemistry, 19/01/2018.
- "The small and wonderful world of nanomaterials: synthesis and characterization of novel ferromagnetic nanostructures", Matteo Cialone, Italy, Turin, University of Turin, Department of Chemistry, 09/03/2018.
- 2nd year PhD presentations, Italy, University of Turin, Department of Chemistry, 24-25/09/2018.
- "Elettrico, Idrogeno, gas, Ibrido. Tecnologie ed emissioni a confronto", TELIOS Fondazione Onlus, Italy, Turin, Sala Bobbio, ex Curia Maxima, 02/10/2018.
- "Chimica Passione Periodica: ENERGIA Rinnovabile, Pulita, Efficiente", Italy, Turin, University of Turin, Department of Chemistry, 04/10/2018.

- “Chimica Passione Periodica: MATERIALI Industria 4.0, Smart material, Additive Manufacturing”, Italy, Turin, University of Turin, Department of Chemistry, 06/12/2018.
- “Le potenzialità del Dottorato anche fuori dall'Accademia. Come valorizzare la figura del giovane ricercatore in azienda”, Italy, Turin, University of Turin, Department of Chemistry.
- “Aluminium alloys for additive manufacturing and their thermal treatments”, Dario Gianoglio, Italy, Turin, University of Turin, Department of Chemistry, 18/01/2019.
- “Synthesis and characterization of Ullmanite compounds”, Francesco Aversano, Italy, Turin, University of Turin, Department of Chemistry, 08/02/2019.
- “Materials and microstructures in Additive Manufacturing”, NIS Colloquium, Italy, Turin, University of Turin, Department of Chemistry, 08/02/2019.
- 2nd year PhD presentations, Italy, University of Turin, Department of Chemistry, 26-27/09/2019.
- “Metal powder for additive manufacturing”, Dr. Volker Uhlenwinkel, Italy, Turin, University of Turin, Department of Chemistry, 15/11/2019.
- “Al alloys for additive manufacturing”, Silvia Marola, Italy, Turin, University of Turin, Department of Chemistry, 25/11/2019.
- “Chemical Journeys”, Italy, Turin, University of Turin, Department of Chemistry, 20/12/2019.
- “Dealloying for the synthesis of nanoporous Molybdenum and Gold”, Deepti Raj, Italy, Turin, University of Turin, Department of Chemistry, 14/02/2020.

- “Hydrogen storage and compression systems based on metal hydrides”, Jussara Barale, Italy, Turin, University of Turin, Department of Chemistry, 15/03/2020.
- “Metal additive manufacturing: effect of rapid solidification on microstructure”, Livio Battezzati, Italy, Turin, University of Turin, Department of Chemistry, 16/06/2020.

Teaching Activities

- Laboratory of “Metallurgy”, Prof. Marcello Baricco e Alberto Castellero - 12-22/01/2018, 24h.
- Laboratory of “Selection and use of materials”, Prof. Paola Rizzi, 2-3/12/2019, 8h.

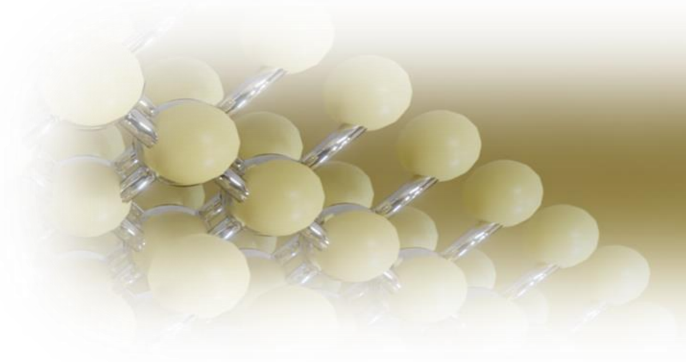

Chapter 1.

Introduction

1.1. Li-ion Batteries

Novel renewable sources are nowadays under continuous evolution and development to make possible a change in the steady rise of greenhouse gases and air pollutants in the atmosphere.[1] Energy demand, however, is still increasing worldwide, mainly from the emerging countries and renewable energy sources compete with oil and coal, which still represent the cheapest source of energy widely available. The development of good, clean and efficient materials for energy storage is the bottleneck for using only renewable energies, instead of fossil fuel, because of their intermittent production of energy over time and geography.[2]

This issue was addressed to many different systems in the past, like chemical and electrochemical storage (hydrogen storage and batteries) or mechanical (pumped-hydroelectric, compressed-air and flywheel) energy storage. Some of them met intrinsic limitations for the targeted application, such as slow kinetics for light solid-state hydrogen storage systems. Recently, the attention has been focused on electrochemical systems, as promising systems capable to store energy efficiently. Between 2010 and 2018, battery demand grew by 30% annually and reached a volume of 180 GWh in 2018. However, the market is expected to keep growing, at an estimated 25% annual rate, to reach a volume of 2,600 GWh in 2030 (**Figure 1.1**).[3]

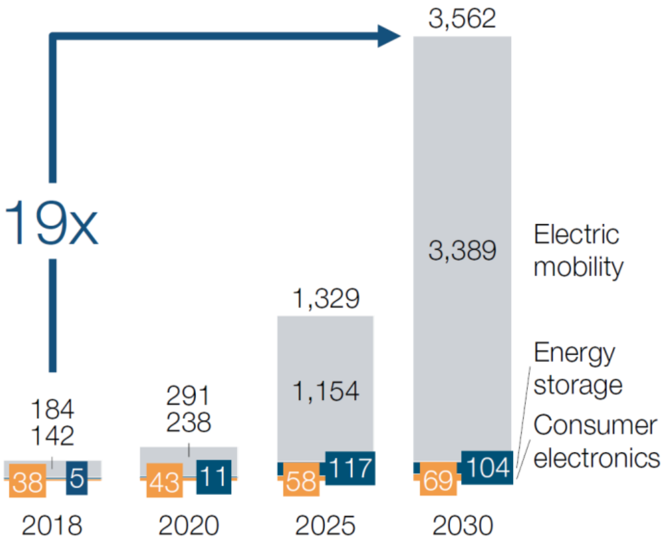

Figure 1.1. *Global battery industry demand (GWh) growth by application and by 2030. Taken for ref.*[3].

Lithium-ion batteries (LIB) use reversible electrochemical reactions to convert chemical energy into usable electrical energy, or to store electrical energy into chemical energy. In a commercial lithium-ion battery, the reactions are based on the transfer of Li^+ between a cathode, typically a layered transition metal oxide, and an anode, typically graphite (**Figure 1.2**).

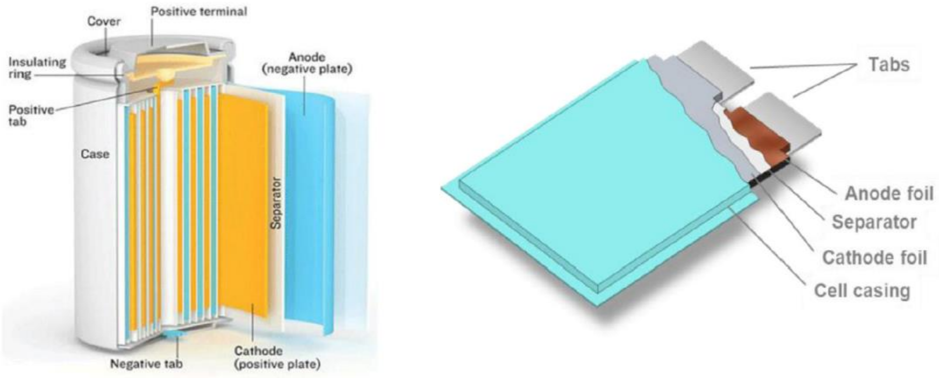

Figure1.2. *Li-ion battery configuration: Taken from ref.*[4].

The electrodes are separated by an electrolyte which blocks the transfer of electrons that would travel when an external load is applied but permits the movement of the ions. Finally, an insulator separator prevents the electrical short circuit.

Nowadays LIBs reach gravimetric energy density up to 250 Whkg^{-1} on the cell level, compared to 20 ÷ 40 Whkg^{-1} for lead-acid batteries which still dominate the market of rechargeable batteries, with their use as car starter batteries.[4] The high energy density of LIBs has enabled the widespread development of portable electronics.

The two main limitations of Li-ion batteries are related to the safety and the relatively limited abundance and inhomogeneous distribution of the elements contained in its components. In fact, nowadays, electrolytes typically consist of lithium salts dissolved in flammable organic solvents, for example in diethyl carbonate (DEC) or tetrahydrofuran (THF).[5] These safety concerns become particularly relevant for fast charging applications, where heat generation can be important. The second limitation is that the LIBs elements quickly become critical, *e.g.* the cobalt used in the cathode, whose known reserves could be quickly depleted at the current growth rate of the demand.[3] While lithium is more abundant, it is not evenly distributed around the earth, which can also cause significant price fluctuations.

1.2. Solid-state electrolytes

In addition to the research for novel electrode materials, capable to accommodate Li-ion reversibly and with a larger capacity, today many efforts have been invested in safety optimization, making electrolyte more stable in temperature and less prone to decompose, limiting in such a way the flammability risk. Solid-state electrolytes (SSE) were proposed as candidates to intrinsically be able to overcome such limitations. Their high thermal conductivity, generally higher for a solid then for a liquid, should avoid the formation of hot spot when high current is required and consequently limiting thermal runaway.

The use of SSE in an all-solid-state Li-ion battery (SSB) can also allow for the use of lithium metal as anode, in place of conventional graphite. Lithium metal possesses a higher theoretical specific capacity (3862 mA hg^{-1}) with respect to graphite (372 mA hg^{-1}), which could lead to a substantial gain of both gravimetric and volumetric energy density. In fact, with an organic liquid electrolyte, the plating of lithium metal upon charging of the battery tends to be highly nonuniform, with a needle-like (dendrites) or highly porous lithium deposition.[6] This can result in a rapid failure of the battery because of short-circuits if the dendrites penetrate through the separator and reach the cathode. In addition, the latter mechanism poses a serious safety concerns, as it can lead to a fire of the battery. For this reason, graphite was selected as anode insertion compound that allowed the development and commercialization by Sony in 1991 of the so-called Li-ion battery.[7]

1.2.1. Properties of a SSE

In summary, whether or not all-solid-state battery technology can meet the aforementioned expectations, will mainly depend on the properties of the solid electrolyte. Notably a solid electrolyte requires:[8,9]

- High Li-ion conductivity, of at least 10^{-3} S cm^{-1} at room temperature (RT).
- The high ionic conductivity should be combined with a low electronic conductivity, lower than 10^{-7} S cm^{-1} to prevent the self-discharge of the battery.
- Large electrochemical stability window, including stability towards alkali metals and high voltage cathodes, to increase the energy density.
- High thermal and chemical stability, to maintain a high level of safety.

- Processability and favorable mechanical properties to maintain a low cost of cell fabrication and reduce interface resistances.

Meeting simultaneously all these criteria represents a major challenge.

1.3. Conduction mechanism in solid

One of the major limitations of solid-state electrolyte is represented by their poor ionic conductivity, typically orders of magnitude lower than 10^{-3} S cm^{-1}, a low-limit benchmark required to an electrolyte. Therefore, improvements on the existing design principles of SSEs, from a structural standpoint, need to be made by a strong understanding over the structural properties governing ionic conduction in solids.[10]

Ionic conductivity (σ) is an intrinsic property describing charge transport by ion diffusion in the presence of an electric field.[11] The mechanism of ion conduction in solids can be described as a thermally activated jump of ions in point defect sites (either vacancies or interstitials), which was first described by Frenkel, Schottky and Wagner.[12] The jumping rate (Γ) can be expressed as the product of an attempt frequency ν , generally taken to be simply the vibration frequency ($10^{12} \div 10^{13}$ Hz)[13], and the statistical probability for the jump over an energy barrier of highness E_m.

$$\Gamma = \nu e^{-E_m/k_B T} \qquad \textbf{(1.1)}$$

where k_B is the Boltzmann constant and E_m represents the migration energy of the mobile specie. Equation **1.1** express an Arrhenius-type mechanism, as it is expected for a thermally activated process. However, E_m does not take into account the necessary energy that must be added to form a defect (interstitial or vacancy) called energy of formation (E_f).

The fraction of vacant sites (N_V) can be expressed:[13]

$$N_V = \sim e^{-E_f/k_B T} \qquad (1.2)$$

Under the presence of an electric field E, the energy barriers result then modified by the additional term $qdE/2$ (*i.e.* where q is the electric charge of the mobile ions and d the jumping distance), making asymmetric the jumping frequencies in the forward and backward direction (**Figure 1.3**), namely $\Gamma_f = \Gamma e^{-qdE/(2k_B T)}$ and $\Gamma_b = \Gamma e^{qdE/(2k_B T)}$.

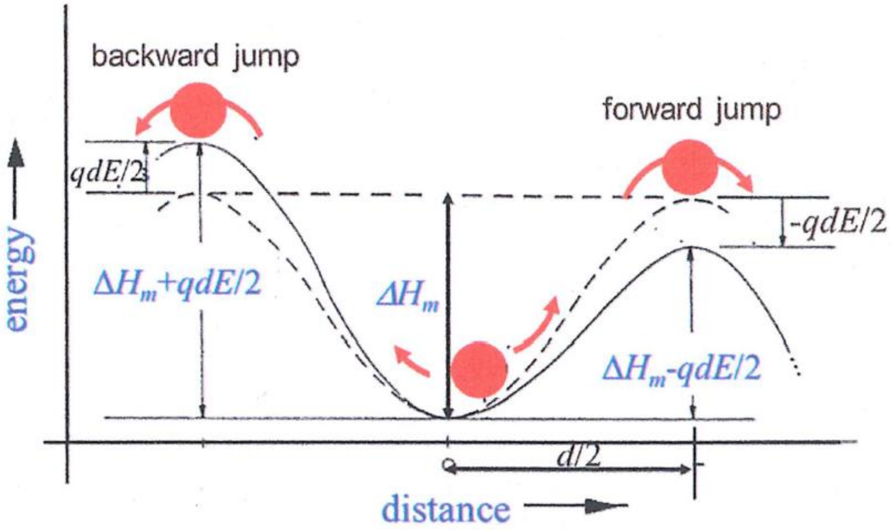

Figure1.3. *Model for the energy barriers deformation caused by an electric field E. The migration enthalpy ΔHm is shifted ±$qdE/2$ from the non-perturbed situation (dotted line) in both forward and backward direction. Taken from ref.*[14].

The ionic current density can be calculated as the difference between these two terms:

$$j = \frac{1}{2} cqd(\Gamma_f - \Gamma_b) \qquad (1.3)$$

where c is the concentration of mobile ions. The factor 1/2 takes into account the diffusion geometry but is in general $1/(2l)$, with l =1,2,3 for one, two three conduction mechanism dimensions, respectively. In standard conditions, the field strength is far below to be comparable with the thermal energy (*i.e.* $qdE \ll k_BT$), which simplifies Equation **1.3** into:

$$j = \frac{cq^2d^2\Gamma}{2lk_BT} \qquad (1.4)$$

Equation **1.4** is the Ohm's law expressing the ionic conductivity (σ). By combining Equations **1.4** and **1.1**, as:

$$\sigma = \frac{\sigma_0}{T} e^{-E_A/k_BT} \qquad (1.5)$$

where $E_A = H_m + H_f$ is the activation energy, while σ_0 is:[13]

$$\sigma_0 = \frac{cq^2d^2\nu}{2lk_B} e^{-\Delta S_m/k_BT} \qquad (1.6)$$

where ΔS_m is the migration entropy, considering that both E_m and E_f can be expressed as G=H-TS. To describe the translational ion motion, it was assumed an immobile sublattice, which defines the energy landscape where mobile ions move. This assumption is however partially incorrect, since temperature-activated dynamical process can also affect the fixed frame in some cases. Thus, for instance, complex ions like $[A_xB_y]^{-n}$ with covalent A-B bond, can be reoriented on their averaged position. If this property belongs to the anions, for instance, have been shown that this beneficially affects the cation mobility as, for instance, the "paddle-wheel" effect.[11,15]

1.4. State of art of SSE

Different classes of materials have been studied as possible candidates to be use as solid-state electrolyte in SSBs. **Figure 1.4** shows the performance of candidate families of solid electrolytes.

Among those, three have recently attracted most of the interest to develop an all-solid-state battery technology.[9] Oxides, such as lithium lanthanum titanate (LLTO),[16–19] often in the form of sintered ceramics, are characterized by a high ionic conductivity (1×10^{-4} S cm^{-1} at R*T*) and a good electrochemical stability.

However, they are hard materials which are difficult to manipulate in the view of the device integration.

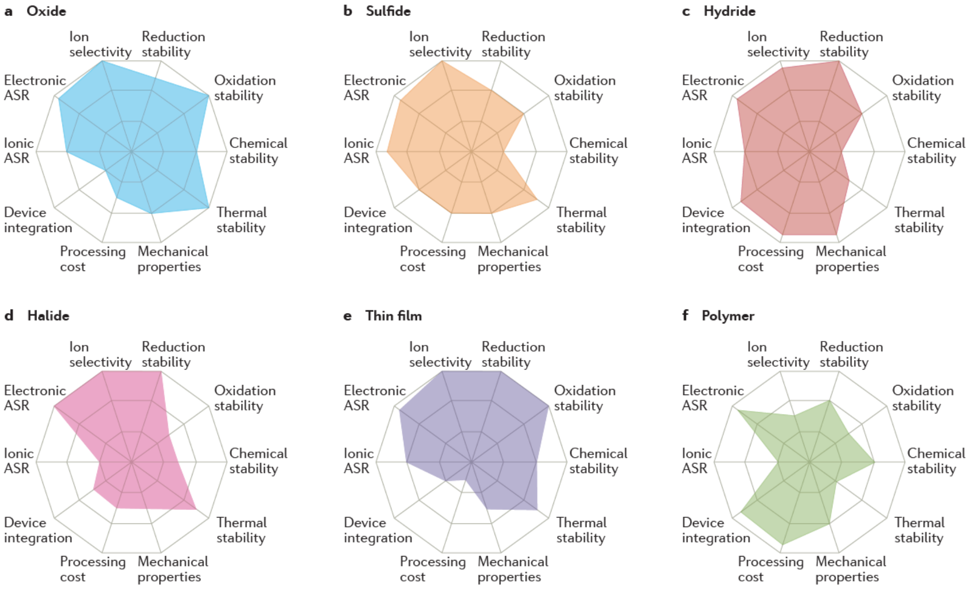

Figure 1.4. Performance of candidate families of solid electrolytes. Taken form ref.[20].

Sulfides, such as LGPS,[21] and thiophosphate have more recently emerged as one of the most promising family of solid electrolytes, as they combine high ionic conductivity and good mechanical properties. As an example, understanding the Young's modulus of solid electrolytes is essential for developing batteries.[22] In a LIB, the volume of the electrode active material particles changes during charging and discharging, causing a capacity fading. Contact between the electrodes and solid electrolytes could be maintained using a SSE that deforms elastically easily in response to the volume change, *i.e.* SSE with a low Young's modulus.[22] However, they mostly suffer from a low chemical and electrochemical stability, as can decompose releasing toxic H_2S in the presence of water. Finally, polymer electrolytes have achieved the highest level of device integration However, their low conductivity at room temperature only allows the cells to be cycled at 60-80◦C.[20]

Among the other families reported in **Figure. 1.4** hydrides are presented with some promising properties in terms of reduction stability as well as processability and device integration.

1.5. Complex Hydrides as solid-state electrolyte

Figure 1.5 presents the Li-ion conductivity of the solid electrolytes based on complex hydrides reported so far.

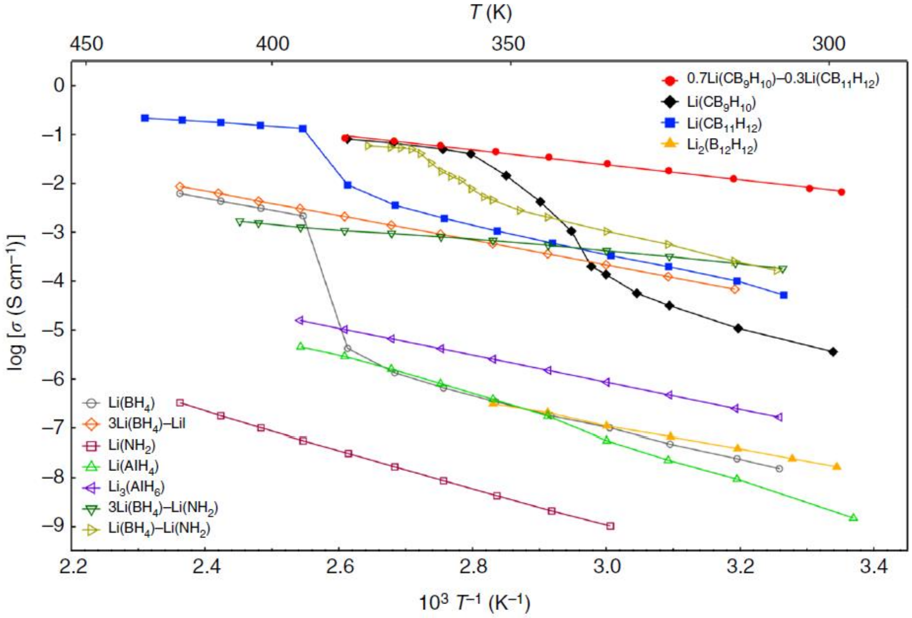

Figure 1.5. *Arrhenius plot of complex hydrides reported in literature, taken form ref.*[23].

The complex hydrides are superior candidates for battery solid electrolytes, in view of high energy density (lightweight compounds) and, in some case, of high Li-ion conductivity. Firstly, metal borohydrides, based on the complex anion as BH_4^-, has been studied and recently the concept was extended to higher boranes and then to carboranes $CB_9H_{10}^-$ and $CB_{11}H_{12}^-$. The structural versatility of complex hydride family makes it possible to synthesize a wide array of new structures in search of novel alkali-metal superionic conductors.

The work performed in this thesis is principally focused on the optimization of composition in different $LiBH_4$ binary and ternary.

1.5.1. $LiBH_4$ as solid-state electrolyte

$LiBH_4$ was synthetized for the first time in 1940 form Schlesinger and Brown.[24]. $LiBH_4$ is a white powder with a melting temperature of 278 ± 5 °C,[25] a lightweight material (0.666 g/cm^3 at 25 °C) and a strong reducing agent. It shows a polymorphic transition from an orthorhombic unit cell at room temperature, space group (s.g.) *Pnma*, to an the hexagonal unit cell, s.g. $P6_3mc$,[26] above 110 ± 2 °C.[25] The enthalpy of transition has been reported equal to 5.0 ± 0.9 KJ/mol.[25] The anion is homoleptic and hydrogen is covalently bound to boron, while an ionic bond is present between the Li^+ and the BH_4^- anion. The H-B-H angles are nearly the same as in the ideal tetrahedron (109.5°). Due to its high gravimetric and volumetric capacities of hydrogen, $LiBH_4$ has been largely studied as a solid-state hydrogen storage material.[27]

In 2007, Matsuo et al.[28] reported a drastic changes of the Li-ion conductivity of $LiBH_4$ above the phase transition temperature (see **Figure 1.5**). Despite the hexagonal polymorph having a remarkable ionic conductivity ($\sim 10^{-3}$ S cm^{-1} at 120 °C), the orthorhombic low temperature phase is much less conductive, showing a Li-ion conductivity of 10^{-8} S cm^{-1} at 30 °C, making a room temperature (*RT*) battery target unviable.[28] In addition to a high Li-ion conductivity at high temperatures, $LiBH_4$ has a large electrochemical window, being electrochemically stable up to 5 V *vs.* Li^+/Li.[27]

Ikeshoji et al.[29] explained, by first principles molecular dynamics calculations, that the enhanced Li conduction due to the phase transition of the $LiBH_4$. The hexagonal structure is made by B and Li atoms layers in the *a*-*b* plane, in which Li atom is stacked on a B atom and vice versa, as shown in **Figure 1.6**.

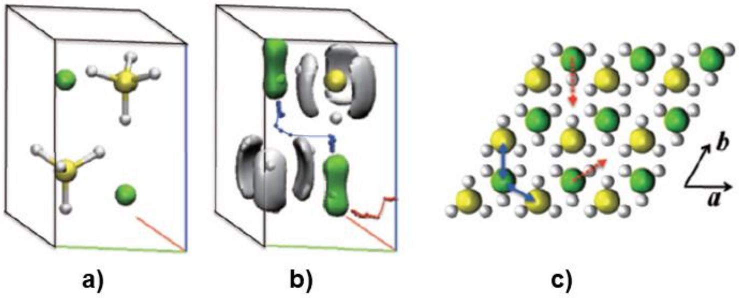

Figure 1.6. *a-b-c) High temperature phase structures of* $LiBH_4$*. b-c) The red lines/arrows indicate Li movement to the empty site (metastable site). The blue line/arrows indicate Li paths. Green region, Li; yellow region, B; white region, H. Taken from ref.*[29].

As can be seen in **Figure1.6b**, Li atoms are distributed in a double splitting, *i.e.* two equal Li atom position separated 0.9 Å along the hexagonal *c*-axis. It is possible to have a Li path connecting the Li positions that are the closest in the *a*-*c* direction (see blue arrows/lines in **Figure 1.6b** and **Figure 1.6c**). There are two types of triangles made by B atoms. One has a Li atom and another has an empty hole at the center, that is a metastable interstitial site.

Li atoms may diffuse in the following way. First, a Li atom moves to a metastable interstitial site by thermal excitation, leaving a vacancy (red arrows/lines in **Figure 1.6b** and **Figure 1.6c**). Then, another Li atom moves into this vacancy through the Li pathway (see blue arrows/lines in **Figure 1.6b** and **Figure 1.6c**) along *a* and *c* directions. The calculated energy of migration (E_m) is 0.31 eV.[29] Similar energies of migration (0.10-0.30 eV) for the orthodromic $LiBH_4$ have been reported by Cho et al.[30]. Therefore, it is the formation of the vacancy (*i.e.* the movement of the Li in the metastable site) that increases the activation energy in the o-$LiBH_4$, leading to a lower ionic conductivity.

In addition, the high Li-ion conductivity of the h-$LiBH_4$ is also due to the rapid reorientation of the BH_4^- anions.[31] Martelli et al.[32] reported that the BH_4^- anions, in the hexagonal phase, possess a frequency of rotational jumps (*i.e.* a rotation frequency) higher than in the orthorhombic phase. The rotational freedom of the BH_4^- have been reported to have positive effects on the Li^+ conductivity.[32] This "paddle-wheel" effect have been reported for complex ions like $[A_xB_y]^{-n}$ with covalent A-B bond.[11,15]

Different approaches have been used to increase the Li-ion conductivity of $LIBH_4$ at R*T*. Many studies showed that substitution of BH_4^- anion with halides (*e.g.* I^- and Br^-) or complex anions (*e.g.* NH_2^- and NH^{2-}) can either stabilize the hexagonal structure at R*T*, or promote the formation of new compounds with improved ionic conductivity at R*T*.[27,33–37] Considering the halogenation, $LiBH_4$-LiI hexagonal solid solutions showed a high conductivity at R*T*. Li-ion conductivity of ~10^{-4} S cm^{-1} at 30 °C has been reported for the mixture with 25 mol% of LiI.[38] The h-$Li(BH_4)_{1-\alpha}(I)_\alpha$ has been reported to be stable in the range of $0.18 \leq \alpha \leq 0.50$. Fast lithium ion conductivity is also retained in h-$Li(BH_4)_{1-\alpha}(Br)_\alpha$ hexagonal solid solutions, although the conductivity is reduced as the bromide content increases above x=0.29.[39] In the system $LiBH_4$-$LiNH_2$, two complex hydrides, $Li_2(BH_4)(NH_2)$ and $Li_4(BH_4)(NH_2)_3$, have been reported to be stable and exhibit lithium-ion conductivities higher than 10^{-4} S cm^{-1} at R*T*.[35,40] Wolczyk et al.[41] reported the stability at R*T* of a novel compound in the system $LiBH_4$-Li_2NH, *i.e.* $Li_5(BH_4)_3NH$, that shows a Li-ion conductivity close to 10^{-6} S cm^{-1} at *RT*.

Another approach is to increase the ionic conductivity of $LiBH_4$ by mixing it with oxides or by means of nanoconfinement.[42–45] Blanchard et al.[45] reported the effect of $LiBH_4$ confinement on Li-ion conductivity and mobility using an ordered mesoporous silica scaffold (MCM-41). Afterwards, Choi et al.[42,43] prepared $LiBH_4$-oxide nanocomposites by ball milling, followed by a heat treatment above the $LiBH_4$ melting point. Electrochemical impedance results obtained for nanocomposites with both SiO_2 and Al_2O_3, demonstrated that the Li-ion conductivity of $LiBH_4$ can be enhanced.

$LiBH_4$ was studied as SSE in several SSB,[46] using TiS_2[47] or sulphur[48] as cathode materials. These SSBs operate at temperature of about 120 °C, allowing a sufficient Li-ion conductivity given by the hexagonal polymorph. The working potential of both TiS_2 and S is about 2 V *vs.* Li^+/Li,[47,48] close to the oxidative limit of $LiBH_4$, which explains the sluggish, but progressive, observed capacity fading. In order to decrease the working temperature, Unemoto et al.[49], used a $LiBH_4$-P_2S_5 mixture, obtaining a poor cycling limited to 10 cycles. Das et al.[50] reported a SSB working at 55 °C, using $LiBH_4$ nanoconfined in silica nanoscaffold as SSE, obtaining 60 charge/discharge cycles.

Aim of the thesis

The aim of this thesis is to fill up the gap between the attractive materials properties of complex hydrides and their implementation into state-of-the art solid-state batteries. In order to achieve this goal, $LiBH_4$ has been chosen as starting material. The optimization of the electrochemical proprieties of this compound have been studied using different approaches.

The starting point was a statistical analysis of the experimental electrochemical data of $LiBH_4$ in order to obtain the values of the energies involved in the conduction process. Then, these values have been compared with the conduction energies calculated by theoretical approaches. Thus, different approaches to increase the Li-ion conductivity of the $LiBH_4$ has been used, showing the pros and cons for the novel mixtures reported herein.

Once the $LiBH_4$-LiBr phase diagram has been defined, the halogenation approach has been used to try to insert chloride in the $LiBH_4$-LiBr hexagonal phase and the effect of the composition on the electrochemical proprieties of the ternary system have been analyzed.

The effect of mechanochemical treatments of $LiBH_4$ with oxides has been analyzed with the aim to study the effect of the addition of the oxides on the Li-ion conductivity of the $LiBH_4$.

The combination of these two approaches has been explored in order to evaluate the presence of a possible synergetic effect.

Finally, once a promising SSE candidate has been individuated the implementation of it in a SSB has been studied.

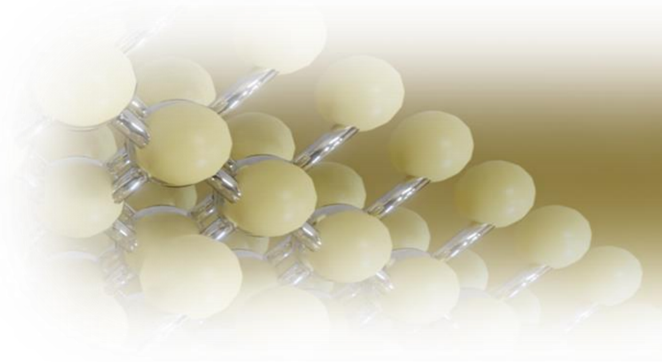

Chapter 2.

Synthesis and Characterizations Methods

In this chapter, the preparation and characterization techniques used in this thesis are presented. Samples prepared are not given here, but they are detailed in each chapter.

All samples synthetized in this thesis are substantially reactive at ambient condition and prone to decompose in presence of moisture. All manipulations and sample preparation were performed in an argon-filled glovebox (MBraun Lab Star Glove Box, supplied with pure 5.5 grade Argon), with a circulation purifier capable of maintaining O_2 and H_2O values typically < 0.1 ppm.

2.1. Mechanochemistry

Mechanochemical treatment, *i.e.* ball milling, is a sample preparation technique used to grind or mix materials as well as to induce solid-state chemical reactions. With respect other synthesis methods, it is considered an unconventional and green synthesis route, since it can be used to initiate chemical reactions or structural transition without the use of solvents.

Ball-milling was used as primary synthesis method for the totality of compounds reported in this thesis. In some cases, the milling step was used as an activation step, followed by a heat treatment which was necessary to obtain the complete solubilization between the starting materials.

The machine used in this work is a Fritsch Pulverisette 6 planetary mill. During the mechanochemical treatment, the jar turns in opposite direction respect the holder rotating plate. This rotation creates for the balls a planetary motion with trajectory passes through the center of the jar, resulting in high-energy impacts for the grinding balls. The high energy impacts may cause microstructural changes, creating new highly reactive surfaces, and introducing stress and strain in the material, increasing defect concentration and the interface area.[51] The dimensions of jar and balls as well as the speed rotation are important parameters in order to tune the impact energy values.

In this work, precursors are weighted giving a total mass of 1 g, resulting in a balls-to-sample mass ratio equal to 30:1. All samples were then ball milled (BM) in 80 mL tungsten carbide vials, with 30 tungsten carbide balls (10 mm diameter). In order to maintain the inert Ar atmosphere during the mechanochemical treatment, the jar was closed inside the glove box using an airtight seal. Different mechanochemical times have been used in base of the type of synthesis and are fully described in each of the following chapters. Periods of milling are always separated by 2 min breaks, to minimize possible heating effects and to allow heat dissipation.

2.2. X-ray Diffraction

Being the totality of the samples synthesized by mechano-chemistry powder X-ray powder diffraction (PXD) was measured with X-ray laboratory sources or with synchrotron radiation source (SR-PXD).

2.2.1. Laboratory X-ray diffraction

Laboratory X-ray powder diffraction (PXD) was extensively used as fingerprinting technique to identify the successful preparation of different samples synthetized or to check possible decomposition products. The *ex-situ* PXD patterns were collected at R*T* using a Panalytical X-pert Pro MPD (Cu

$K_{\alpha 1}$ = 1.54059 Å, $K_{\alpha 2}$ = 1.54446 Å) in Debye-Scherer geometry. Patterns were collected from 10° to 70° 2θ range, with a step size 0.016, a time step of 60 s for a total of 30 min per scan. 0.5 mm glass capillaries were filled with the sample powder and sealed under Ar atmosphere.

2.2.2. Synchrotron radiation: Petra III and ESRF

SR-PXD is a powerful technique for the study of complex hydrides stabilities as a function of temperature, decomposition mechanism or reactions,[52,53] and was used in **Chapter 3**. The *in situ* SR-PXD measurements were performed at the diffraction beamline P02, in the Petra III storage ring of DESY (Hamburg, Germany). Few milligrams of sample were packed in a 0.6 mm (inner diameter) single crystal sapphire capillary. The sample was heated up and cooled down at 5 °C/min. The wavelength and the detector geometry were calibrated using an LaB_6 external standard. The beamline provides a monochromatic X-ray beam (λ = 0.207157 Å) and is equipped with a PerkinElmer XRD 1621 plate detector (pixel size 200 µm × 200 µm, array 2048 × 2048 pixels). The raw 2D diffraction datasets collected were transformed and integrated to a 1D powder patterns with the FIT2D program using a mask to remove the undesired spots from the single-crystal sapphire tube and shadow from the sample holder.[54,55]

2.2.3. Rietveld Refinement

PXD patterns were refined by means of the Rietveld method in order to obtain structural information (*e.g.* lattice parameters and atom occupancy of crystallographic sites) and, in multi-phases diffraction profile, to obtain the mutual quantity of the phases. Experimental PXD pattern is fitted by least-square minimization routine by a theoretical line profile. The theoretical pattern is described by equations that depend on: a scale factor, the structure factor and the Lorentz polarization. The peaks shape is described by pseudo-Voigt function, a gaussian/Lorentzian summation, and the full width at half maximum is expressed by the Caglioti formula.[56] The preferential orientation could be also taken in account in the fitting process. An additional function can be use in order to describe of asymmetry due to axial divergence of the diffracted beam at low angles. The last term accounts for the background, that was simulated through a polynomial function with 3 or 4 parameters.

The Rietveld refinement of diffraction patterns has been performed using the MAUD (Materials Analysis Using Diffraction) software.[57] Reliability parameters R_{wp}, R_{exp} and χ^2, were used to evaluate the quality of the fitted patterns. The instrumental function, that is a function describing the peak broadening due to the instrumentation geometry, was determined using pure Si, for the *ex situ* measurements. Parameters were also refined to consider possible instrument misalignment.

The following sequence was applied for the refinement of parameters: (1) scale factor (2) background parameters (3) lattice constants (4) crystallites size (5) micro-strain.

2.3. High Pressure Differential Scanning Calorimetry

DSC was widely used in this work to determine thermal events (principally phase transition and decomposition). The identification of the transition temperature allowed to better understand changes that were observed with other techniques, such as X-ray diffraction or impedance spectroscopy. A 204 Netzsch HP-DSC, placed inside an Ar filled glove box, was used to perform High-Pressure Differential Scanning Calorimetry (HP-DSC) analysis, in order to evaluate the thermal stability behavior of the samples. Approximately 5–10 mg of sample was loaded into closed aluminum crucibles with a lid. Samples were heated and cooled in the desired temperature range at 5 or 20 °C/min under 2 or 10 bars of H_2. Depending on the sample, various thermal cycles were performed.

The instrument was calibrated in temperature and heat flow using the melting enthalpy and temperature of high purity standards (Bi, In, Sn, Zn). The same crucible, heating rate and H_2 pressure has been used for the calibration.

2.4. Infrared Spectroscopy

In this thesis, the Infrared spectra were collected in Attenuated Total Reflection (ATR-IR) mode with a Bruker Alpha-P spectrometer, equipped with a diamond crystal. The instrument was placed inside a nitrogen filled glove-box. All spectra were recorded in the 5000–400 cm^{-1} range with a resolution of 2 cm^{-1}. Reported data are an average of 64 scans.

2.5. Modelling

Nowadays, with increasing computational power and software development, modelling techniques are becoming more and more popular, and widely used for a screening of material properties.

2.5.1. Calphad Method

The Calphad method is based on a parametric description of the Gibbs free energy as a function of temperature and composition.[58] Literature data and experimental evidence are used as input data. In order to establish the Gibbs free energy of compounds with crystal structures different from the stable one (end-members), *ab-initio* calculations are often necessary. A process of optimization by best fitting allows the assessment of parameters in order to have the most reliable description of Gibbs free energy for all phases in the system based on the input values.

The Calphad method has been used in **Chapter 4** in order to perform the assessment of the $LiBH_4$-LiBr binary phase diagram, using the Thermo-Calc Software[59]. The calculations were done in collaboration with Dr. Erika Michela Dematteis, Dr. Marta Corno and Prof. Mauro Palumbo form the Department of Chemistry of the University of Turin.

2.5.2. Topological analysis

The Li-ion conductivity strictly depends on the energy barrier for diffusion, *i.e.* the minimum energy needed to complete a jump from one site to another in the crystal structure. Several approaches have recently been applied in the literature,[60–64] among which topological methods have been successfully applied to reveal new prospective Li- conductors.[65,66]

A combination of DFT calculations, performed with the program package Vienna Ab Initio Simulation Package (VASP).[67], and topological analysis of the migration maps, carried out with the ToposPro package[68], has been used to evaluate the migration energy (E_m). As described in **Chapter 1**, the Li-ion migration activation energy depends also on the energy of defect formation (E_f), calculated using DFT according to the formalism detailed in by Van de Walle et al.[69].

The *ab-initio* calculations performed in **Chapter 3** were done in collaboration with Prof. Mauro Palumbo form the Department of Chemistry of the University of Turin and the research group of Prof. Vladislav A. Blatov form the Samara Center for Theoretical Materials Science of the Samara University.

2.6. Electrochemical Impedance Spectroscopy

Electrochemical Impedance Spectroscopy (EIS) is a very commonly used technique for the study of intrinsic materials properties, such as the quantification of the ionic conductivity of electrolytes, both liquid and solid.

EIS is a technique used to probe the electrical response of a material that is subjected to an oscillating (sinusoidal) small ac voltage signal of fixed amplitude (*e.g.* in the 10 mV to 50 mV range), so that the response of the material remains linear. The response of the material can be probed over a large range of frequencies, typically in the range of a few mHz to ~10 MHz.

As a result of the applied field, the moving charges in the sample will generate a response current that oscillates with the same frequency but is shifted in phase, and V, I and Z can be expressed as:

$$V = V_0 e^{i\omega t} \tag{2.1.}$$

$$I = I_0 e^{i(\omega t - \varphi)} \tag{2.2.}$$

$$Z = Z' + iZ'' \tag{2.3.}$$

where $Z' = Z_0 \cos\varphi$ and $Z'' = Z_0 \sin\varphi$.

Often, the measured complex impedance is represented in a Nyquist plot of Z'' vs. Z' that can be fitted by the use of equivalent electrical circuits. In the case of an ideal ionic conductor, the impedance response can be approximated by a parallel RC circuit, with a resistance related to the ion generated current, in parallel with a capacitor related to the dielectric response of the material, giving rise the typical "semicircle" in the Nyquist plot.[70]

For such a circuit, the Nyquist plot will have the typical shape of a semi-circle as shown in **Fig. 2.1.a**, while the frequency dependence of the real and imaginary part of Z are shown in **Fig. 2.1b**.

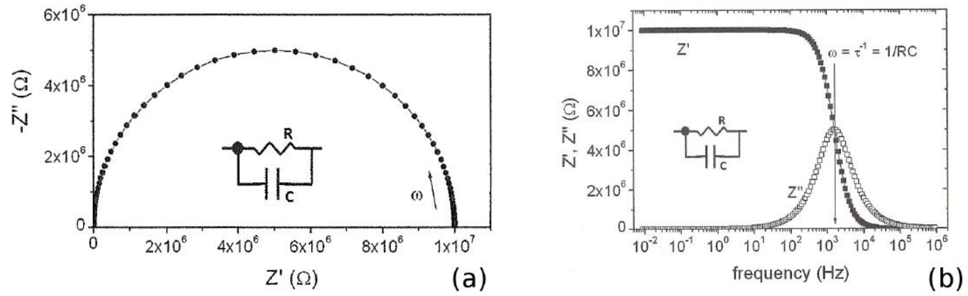

***Figure 2.1**. a) (a) Nyquist plot of the impedance for a parallel RC circuit representing the electrical response of an "ideal" ionic conductor. The values R = 10 MΩ and C = 10 pF are used in the plot (equivalent circuit shown in the inset) and the impedance frequency dependence of real (Z') and imaginary part (Z"). The value R=10MΩ and C=10pF are used in the plot. b) while the frequency dependence of the real and imaginary part of Z are shown Taken from ref.*[14].

On the Nyquist plot, the highest frequencies are on the left (near Z' = 0) while the lowest frequencies are on the right. A first characteristic value of the system can be found at the intersection of the Nyquist curve with the x-axis (Z'' = 0), where Z' = R. This value is related to the direct current conductivity of the material according to the equation:

$$\sigma = d/AR \qquad \textbf{(2.4.)}$$

where R is the resistance obtained from the fit of EIS data, d is the thickness of the sample, and A is its area. The conductivity then has the unit of $\Omega^{-1}\text{m}^{-1}$ or equivalently S m^{-1} (S cm^{-1} is more commonly used). Then, the frequency at which Z''reaches its maximum, is the characteristic frequency of the circuit, $\omega = 1/RC$. It corresponds to a characteristic relaxation time $\tau = RC$ of the system, relying to the Debye relaxation model of complex dielectric permittivity. The Debye-like dependency is often detected in the non-ideal form, where the capacitance is replaced by a constant phase element (CPE), graphically resulting into a shift of the circle center, below the real axis.

Finally, it is common to observe a linear tail following the semicircles towards the lowest frequencies. This tail is caused by the accumulation of ions at the electrodes through which the perturbation signal is applied. These electrodes are often chosen to block the diffusion of ions causing this polarization effect at sufficiently low frequencies. Such a fit can also be performed for measurements done at different temperatures to extract the activation energy of the thermally activated ionic conductivity of both processes. In hydroborates however, there is generally no significant grain boundary contribution.[71] A single resistance can be extracted which is related to the total, direct current ionic conductivity of the sample. Impedance spectroscopy can also be used to characterize devices involving not only the electrolyte but also diffusion processes through the electrode materials as well as the electrode-electrolyte interfaces. These contributions will add to the complexity of the measured signal.

The EIS measurement performed in **Chapter 5 and Chapter 8** were done in collaboration with the research group of Prof. Radovan Černý form the Laboratoire de Cristallographie, of the Université de Genève. The EIS spectra were collected using a HP4192A LF impedance analyzer (frequency range 5 Hz ÷ 2 MHz, applied voltage 10 mV) and a Novocontrol sample cell BDS 1200. Samples were compacted into pellets (diameter 10 mm, thickness 0.2-0.6 mm) with an axial hydraulic press at about 20-60 MPa. Gold disks were used as blocking electrodes. EIS was performed every 10 °C in the temperature range $\mathrm{R}T < T < 150$ °C. Two cycles were performed and analyzed for selected samples in order to verify the reproducibility of the measurements. Impedance data were analyzed via the EqC software,[72] following the data validation described in ref.[73].

The EIS measurement performed in **Chapter 6 and Chapter 7** were done in collaboration with the research group of Prof. Petra de Jongh form the Debye Institute for Nanomaterials Science of the Utrecht University. The EIS spectrum was collected using a PARSTAT 2273 potentiostat (frequency range 1 Hz ÷ 1 MHz, applied voltage 10 mV). Samples were compacted into pellets (diameter 13 mm, thickness 1-2 mm) using an axial hydraulic press with about 200 MPa pressure. Lithium foils (Sigma Aldrich, purity 99.9 %, 0.38 mm thick) were used as non-blocking electrodes. EIS was performed every 10 °C in the temperature range RT < T < 130 °C during the heating ramp, probing every 20 °C during cooling. Different EIS temperature-dependent cycles were performed to verify the reproducibility and the stability of measurements. Impedance data were analyzed via the EqC software,[72] following the data validation described in ref.[73].

2.7. DC polarization

In order to verify that the ionic conductors possess a negligible electronic conductivity, the electronic conductivity has been measured by dc-polarization.[50,74] Ionically-blocking electrodes are used to suppress the ionic transport so that only electronic species can pass through the system. The electronic conductivity has been measured at RT for the samples reported in **Chapter 6**. Samples were compacted into pellets (diameter 13 mm, thickness 1-2 mm) using an axial hydraulic press with about 200 MPa pressure and the electronic conductivity has been measured by using a PARSTAT 2273 potentiostat. A constant voltage of 0.5 V was applied across the pellet, using stainless steel blocking electrodes, and the resulting current was monitored as a function of time.

When the constant voltage is applied, the initial current consists on the sum of the ionic and electronic currents. After certain period of time, the steady-state current remaining is proportional, according to the Ohm's law, to the electronic resistance.

2.8. Cyclic voltammetry

Cyclic voltammetry (CV) is the study of the response current of a system to an applied voltage. In this thesis both methods were used, to estimate the electrochemical stability windows (ESW) of solid electrolytes. The oxidation stability or anodic limit of an electrolyte refers to its oxidation potential. When electrolyte decomposition occurs, oxidation currents can be measured at the working electrode, that is typically an inert working electrodes to avoid parasitic reactions other than the electrochemical oxidation.[75]

The CVs showed in this work were performed on a pelletized sample using metallic Li as self-reference electrode and Au as counter electrode. Despite it is known the existence of Li-Au alloy, potentially forming electrochemically by using gold as working electrode, preliminary tests were conducted not showing any detectable peak referring to such processes. Because of assembly difficulties, a reference electrode is rarely used in all-solid-state measurements.[76] The counter electrode thus also serve as a reference The potential of the Li/Li$^+$ redox couple then serves as a reference potential.

In the original reports of several well-known solid electrolyte phases, very high overestimated stability windows were reported.[77,78] This overestimation originates form two main factors that causes a very small decomposition currents. The fist factor is the low kinetics of the reaction occurring at the solid-solid interface between the solid electrolyte pellet and working electrode. The second is the interface between a solid electrolyte pellet and a flat metallic working electrode can result in a low contact surface area and thus a high interface resistance. In order to increase the probed surface the method described in the ref.[79]. Samples were prepared by mixing the desired compound with the carbon black (CB, Ketjenblack EC600JD, Akzo Nobel Chemicals) into an agate mortar (95:5 weight ratio). 8 mg of such mixture were pressed at 240 MPa with about 25 mg of the pure compound into an uniaxial hydraulic press (diameter 6 mm), forming a two-layers pellet. This approach increases effectively the active area where an electrochemical reaction could take place, increasing the resulting anodic peak in case of electrolyte oxidation. The obtained pellets were then tested in a two-electrode 3/4″ PTFE Swagelok-type cell, with a Lithium disk (99.9 %, Sigma-Aldrich) as the counter and reference electrode (SSE side) and a stainless-steel disk as working electrode (SSE+CB side). The cells were tested with a potentiostat/galvanostat Biologic MPG-2, after a 4 h rest at 60 °C. CV measurements have been performed into a voltage region $-1 < V < 5$ V *vs.* Li^+/Li, at a scanning rate between of 20 and 500 $\mu V\ s^{-1}$.

The CVs showed in this thesis (**Chapter 5 and Chapter 8**) were done in collaboration with the research group of Prof. Radovan Černý form the Laboratoire de Cristallographie, of the Université de Genève.

2.9. Galvanostatic cycling

Complementary to voltammetry methods, galvanostatic methods evaluate the voltage response of a system when it is subjected to a constant current.

2.9.1. Galvanostatic stripping/plating

The stability of solid electrolytes towards reduction is also often assessed via galvanostatic stripping plating experiments in which the electrolyte is placed in between two alkali metal electrodes.[80] A constant current is then applied to cycle the metal which gets striped (*i.e.* oxidized) from one electrode to be plated (*i.e.* reduced) on the opposite electrode. This current is applied alternatively in each direction for several minutes or hours and the response of the cell is recorded. The measured voltage is a result of the internal resistance of the cell to the flow of ions which comprises the bulk electrolyte resistance, and importantly the interface resistance. An incompatibility between the electrolyte and the alkali metal electrode, *i.e.* interface change, will thus be highlighted with a change of the resistance. An increasing overpotential reflects the continuous growth of a resistive layer as the electrolyte decomposes into a poorly ionic, but electron conducting compounds. A stable potential on the other hand can reflect the absence of reaction between the electrolyte or the formation of a passivating layer that does not grow after its initial formation. The stripping-plating experiment while giving valuable indications

2.9.2. Galvanostatic Cycling with Potential Limitation

Galvanostatic Cycling with Potential Limitation (GCPL) is a routine technique to study batteries or, more generally, electrochemical cells, by analyzing the voltage response of a system when it is subjected to a constant current, as long as the voltage remains within a defined range. The current adopted is expressed in the convenient unit of C/n where C is the capacity of the battery while n indicates the number of hours needed to completely discharge the system. The capacity (or total charge) is indeed measured in mA h and it is calculated as

$$C = \frac{mzF}{MM} \tag{2.5.}$$

that is measured in mA h g^{-1}, where m is mass of the electrochemical active material and MM its molar mass, z the number of transferred charges and F the Faraday constant.

The measured voltage change during a GCPL reflects the reactions taking place at the active electrode. The reactions between the electrodes active material and lithium ions can be a conversion, typically, to a binary alloy or the intercalation to a layered structure capable to accommodate mobile cations within different lattice planes. When an electrochemical active material starts absorbing a mobile cation a voltage plateau is expected. On the other hands, a single phase region of the phase diagram reflects an abrupt change in the cell voltage. The GCPLs measured in **Chapter 8** were performed, using a Biologic MPG-2, in collaboration with the research group of Prof. Radovan Černý form the Laboratoire de Cristallographie, of the Université de Genève.

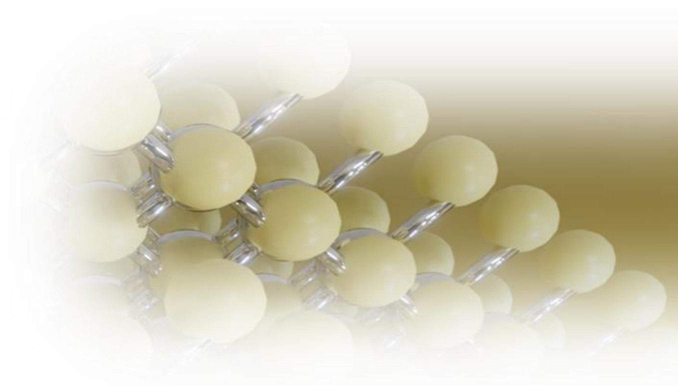

Chapter 3.

Combined DFT and Geometrical-Topological Analysis of Li-ion conductivity in Complex Hydrides

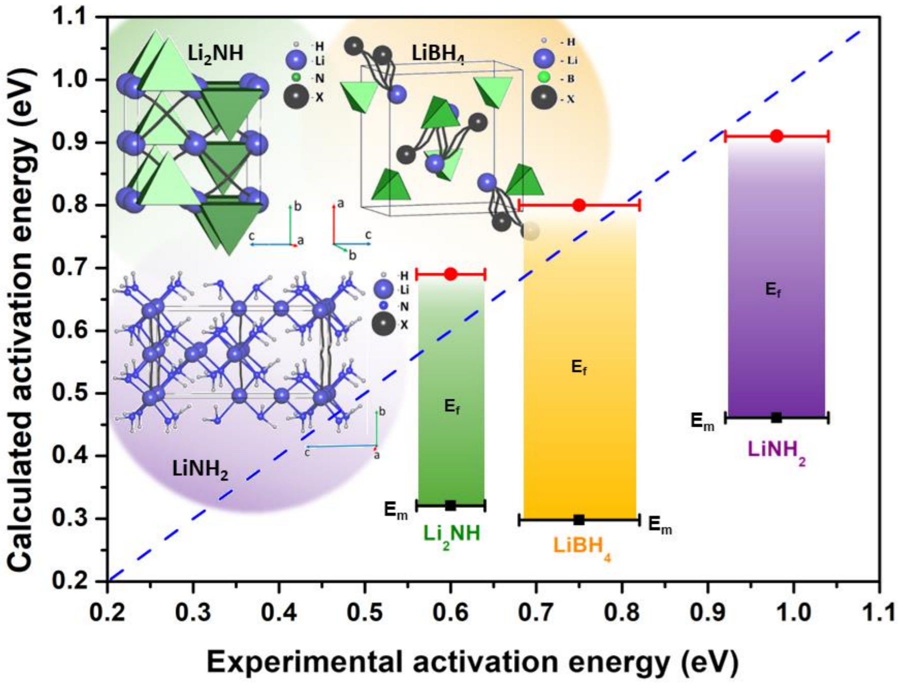

3.1. Introduction

In the last years, a large number of EIS measurement to study the Li-ion conductivity of the $LiBH_4$ have been reported in literature. This chapter is aimed to obtain an average value of the activation energies involved the Li-ion motion of $LiBH_4$, in both the hexagonal and orthorhombic phase. In addition, by a combined topological–DFT approach, the migration (E_m) and defect formation (E_f) energies of the o-$LiBH_4$ have been calculated, since the conduction mechanism in the hexagonal phase has been widely studied in literature.[29,32,49,81] Results on activation energy obtained using computational methods have been compared with those obtained experimentally in the literature, providing additional insight on the mechanisms of ion mobility in complex hydrides. This approach has been extended also to other complex hydrides proposed as SSE in literature.

3.2. Result and discussion

3.2.1. Statistical analysis

A survey of experimental data on Li-ion conductivity of $LiBH_4$ reported in the literature was performed. As experimental results of Li-ion conductivity and activation energy show significant scatter (see **Figure 3.1**), a statistical analysis was carried out before comparison with theoretical findings. The statistical analysis was performed in order to obtain the average value of activation energy (E_A), $\ln\sigma_0$ and Li-ion conductivity for $LiBH_4$, using literature data.[28,35,38,42,45,77,82–84]

As shown in **Figure 3.1**, several EIS measurements of the Li-ion conductivity $LiBH_4$ are reported in the literature, showing a significant scatter. As an example, data span from 5×10^{-8} S cm^{-1} to 7×10^{-7} S cm^{-1} at 70 °C, within more than an order of magnitude range. In addition, a difference of about 12.5 °C on the transition temperature has been highlighted. Unfortunately, details about experimental conditions regarding these measurements are often not reported in the original papers, hence results can arise from different experimental conditions and sample preparation methods.

A further experimental parameter to be considered is the application of mechanical milling. In fact, ball-milled samples show usually higher ion conductivity with respect to non-milled samples (**Figure 3.1**).[82,83]

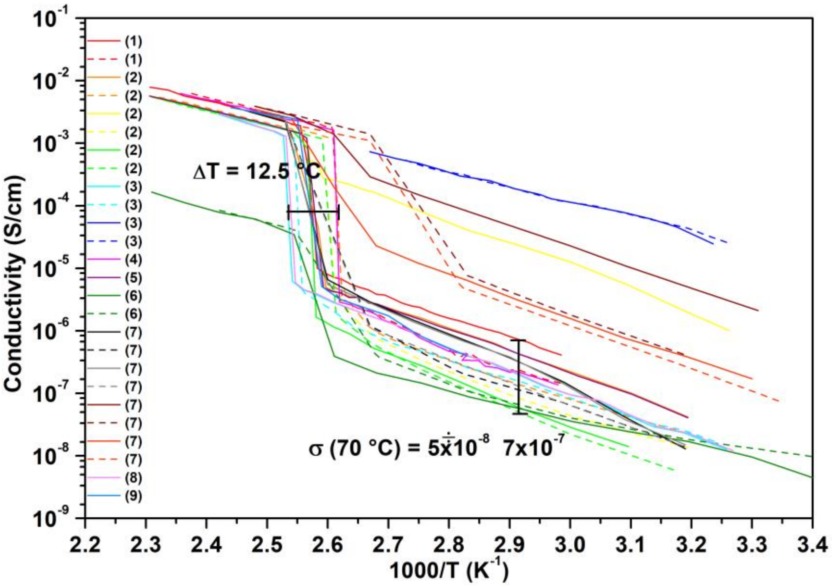

Figure 3.1. *Li-ion conductivity data of $LiBH_4$ reported in the literature. Solid and dash lines refer to the heating and cooling temperature-dependent EIS ramp, respectively. In the label: (1) Matsuo, M. et al. Appl. Phys. Lett.* ***2007****, 91; (2) Matsuo, M. et al. Appl. Phys. Lett.* ***2009****, 94; (3) Sveinbjörnsson, D. et al. J. Solid State Chem.* ***2014****, 211; (4) Miyazaki, R. et al. Solid State Ionics* ***2011****, 192; (5) Matsuo, M. et al. J. Am. Chem. Soc.* ***2009****, 131; (6) Gulino, V. et al. Chem. Mater. 2019, 31; (7) Gulino, V. et al. ACS Appl. Energy Mater. 2020, 3; (8) Blanchard, D. et al. Adv. Funct. Mater.* ***2015****, 25; (9) Choi, Y. et al. Phys. Chem. Chem. Phys.* ***2016****, 18.*

The main explanation of the increased Li-ion conductivity is that the mechanochemical treatment increases the defect concentration of the orthorhombic $LiBH_4$ (see **Chapter 6**).[83,84] The effect of ball milling on Li-ion conductivity in maintained if the sample is heated up to a temperature lower than the phase transition, as reported by Sveinbjörnsson et al.[83] On the contrary, the higher ionic conductivity due to the mechanical milling effect is reduced after the phase transition, as reported by Matsuo et al.[82]. In fact, once the milled samples undergo the phase transition, defects are recovered and the Li-ion conductivity decrease.[84] Therefore, the data of the ball-milled samples have been excluded in the calculation of the average values.

From EIS measurements reported in the literature, the activation energy (E_A) and the logarithm of the pre-exponential factor ($\ln \sigma_0$) were obtained by a linear fit of an Arrhenius plot for Equation **1.5**, by plotting the $\ln(\sigma T)$ as a function of 1000/T. A confidence interval was obtained from the linear fitting for both values of E_A and $\ln \sigma_0$. This interval was calculated using a confidence level of 99.99 %. in order to include all the experimental points inside the interval, *e.g.* as shown in **Figure 3.2**.

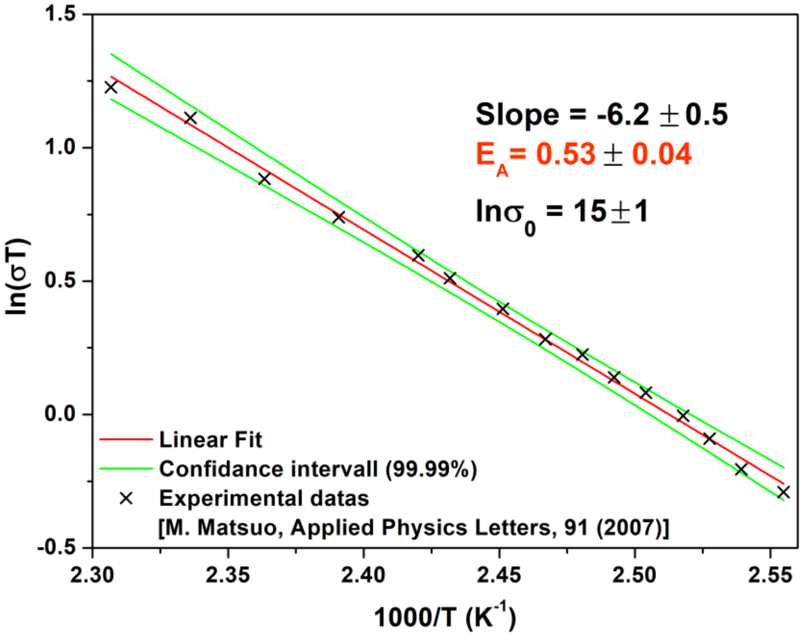

Figure* 3.2.** *Linear fit of the $LiBH_4$ hexagonal phase data of (1) Matsuo, M. et al. Appl. Phys. Lett.* ***2007*, 91.*

The activation energies obtained from single set of data are reported in **Table 3.1**, while the values of the logarithm of the pre-exponential factor are shown in **Table 3.2**.

EIS ramp	EIS cycle	Milled	E_A (eV) RT	C.I.	E_A (eV) HT	C.I.	Ref.
Heating	1st	No	0.69	0.04	0.53	0.04	(1)
Cooling	1st	No	0.81	0.09	0.50	0.04	(1)
Heating	1st	No	0.71	0.04	0.5	0.3	(2)
Cooling	1st	No	0.7	0.1	0.49	0.04	(2)
Heating	1st	**Yes**	**0.74**	**0.07**	**0.5**	**0.2**	(2)
Cooling	1st	**Yes**	**0.7**	**0.3**	**0.5**	**0.1**	(2)
Heating	2nd	**Yes**	**0.8**	**0.1**	**0.6**	**0.5**	(2)
Cooling	2nd	**Yes**	**0.9**	**0.2**	**0.5**	**0.1**	(3)
Heating	1st	No	0.77	0.04	0.7	0.7	(3)
Cooling	1st	No	0.7	0.1	0.5	0.2	(3)
Heating	1st	**Yes**	**0.51**	**0.07**	/	/	(3)
Cooling	1st	**Yes**	**0.51**	**0.05**	/	/	(3)
Heating	1st	No	0.8	0.1	0.50	0.03	(4)
Heating	1st	No	0.71	0.04	0.5	0.2	(5)
Heating	1st	No	0.50	0.1	/	/	(6)
Heating	1st	No	0.91	0.08	/	/	(7)
Heating	2nd	No	0.89	0.06	/	/	(7)
Heating	1st	**Yes**	**0.70**	**0.03**	/	/	(7)
Heating	2nd	**Yes**	**0.75**	**0.04**	/	/	(7)
Heating	1st	No	0.76	0.04	/	/	(8)
Average			**0.73**	**0.08**	**0.5**	**0.2**	
Average excluding bold data			**0.75**	**0.07**	**0.5**	**0.2**	

Table 3.1. *Activation energy (eV) calculated by linear fit of ln(σT) and 1000/T of literature data, for the RT and HT phase of* $LiBH_4$ *(99.99 % of confidence). CI is the confidence interval half width. The bold (red) data were excluded in the calculation of the average activation energy data. 1st and 2nd refer to the temperature-dependent EIS cycle data.*

EIS ramp	EIS cycle	Milled	$\ln\sigma_o$ RT	C.I.	$\ln\sigma_o$ HT	C.I.	Ref.
Heating	1st	No	15	1	15	1	(1)
Cooling	1st	No	18	3	15	1	(1)
Heating	1st	No	15	1	15	8	(2)
Cooling	1st	No	13	5	14	1	(2)
Heating	1st	**Yes**	**20**	**2**	**15**	**5**	(2)
Cooling	1st	**Yes**	**14**	**9**	**14**	**3**	(2)
Heating	2nd	**Yes**	**17**	**3**	**16**	**13**	(2)
Cooling	2nd	**Yes**	**20**	**8**	**14**	**2**	(3)
Heating	1st	No	16	1	19	9	(3)
Cooling	1st	No	14	4	14	6	(3)
Heating	1st	**Yes**	**15**	**2**	/	/	(3)
Cooling	1st	**Yes**	**14**	**2**	/	/	(3)
Heating	1st	No	18	3	15	1	(4)
Heating	1st	No	15	1	15	5	(5)
Heating	1st	No	6	4	/	/	(6)
Heating	1st	No	21	2	/	/	(7)
Heating	2nd	No	22	2	/	/	(7)
Heating	1st	**Yes**	**19.3**	**0.3**	/	/	(7)
Heating	2nd	**Yes**	**17**	**1**	/	/	(7)
Heating	1st	No	16	1	/	/	(8)
Average			**16**	**3**	**15**	**5**	
Average excluding bold data			**16**	**2**	**15**	**4**	

Table 3.2. *$\ln\sigma_o$ calculated by linear fit of $\ln(\sigma T)$ and $1000/T$ of literature EIS data, for the RT and HT phase of $LiBH_4$ (99.99 % of confidence). CI is the confidence interval half width. The bold (red) data were excluded in the second calculation of the average $\ln\sigma_o$. 1st and 2nd refer to the temperature-dependent EIS cycle data.*

Using the confidence interval for each EIS measurement, it was also possible to calculate a maximum and minimum value of $\ln(\sigma T)$, by using the maximum and minimum values, given by the confidence interval, of both E_A and $\ln \sigma_o$. From these values, it was possible to calculate σ at 30 °C and a confidence interval associated to it, as reported in **Table 3.3**.

EIS ramp	EIS cycle	Milled	$\ln(\sigma T)_{FIT}$	$\ln(\sigma T)_{MAX}$	$\ln(\sigma T)_{MIN}$	Ref.
Heating	1st	No	-11.40	-11.18	-11.63	(1)
Cooling	1st	No	-13.12	-12.59	-13.66	(1)
Heating	1st	No	-11.98	-11.78	-12.19	(2)
Cooling	1st	No	-12.78	-13.93	-11.63	(2)
Heating	1st	**Yes**	**-8.23**	**-7.85**	**-8.61**	(2)
Cooling	1st	**Yes**	**-13.48**	**-12.12**	**-14.84**	(2)
Heating	2nd	**Yes**	**-14.41**	**-13.80**	**-15.02**	(2)
Cooling	2nd	**Yes**	**-14.90**	**-13.49**	**-16.30**	(3)
Heating	1st	No	-12.95	-12.74	-13.16	(3)
Cooling	1st	No	-12.83	-12.23	-13.43	(3)
Heating	1st	**Yes**	**-5.04**	**-4.77**	**-5.31**	(3)
Cooling	1st	**Yes**	**-5.01**	**-4.82**	**-5.20**	(3)
Heating	1st	No	-13.17	-12.53	-13.81	(4)
Heating	1st	No	-12.01	-11.81	-12.21	(5)
Heating	1st	No	-12.90	-12.53	-13.26	(6)
Heating	1st	No	-13.31	-13.04	-13.58	(7)
Heating	2nd	No	-13.72	-13.44	-13.99	(7)
Heating	1st	**Yes**	**-7.25**	**-6.36**	**-8.13**	(7)
Heating	2nd	**Yes**	**-11.81**	**-11.24**	**-12.37**	(7)
Heating	1st	No	-12.90	-12.68	-13.12	(8)
Average ln(σT)			**-11.66**	**-11.25**	**-12.07**	**C.I.**
Average σ at 30 °C			**2.85x10^{-8}**	**4.30x10^{-8}**	**1.89x10^{-8}**	**1.21x10^{-8}**
Average ln(σT) excluding bold data			**-12.76**	**-12,54**	**-12,97**	**C.I.**
Average σ at 30 °C excluding bold data			**9.5x10^{-9}**	**1.18x10^{-8}**	**7.66x10^{-9}**	**2.07x10^{-9}**

Table 3.3. *ln(σT) and Li-ion conductivity at 30 °C (303.14 K) calculated using the data (1000 E_A/k_B and $\ln\sigma_o$) obtained by the linear plot of ln(σT) and 1000/T of literature data (see* ***Table 3.1*** *and* ***Table 3.2****). 1st and 2nd refer to the temperature-dependent EIS cycle data. CI is the confidence interval half width, calculated averaging the $\ln(\sigma T)_{MAX}$ and the $\ln(\sigma T)_{MIN}$.*

This type of analysis has been expanded also to other complex hydride compounds studied in literature, *i.e.* $LiNH_2$, Li_2NH, $Li_2(NH_2)(BH_4)$ and $Li_4(NH_2)_3(BH_4)$, and the results are reported in **Table 3.4**.

From the statistical analysis, it was possible to obtain average values, for each compound, of the Li-ion conductivity at 30 °C, the activation energy (E_A) and the logarithm of pre-exponential factor (ln σ_0) (**Table 3.4**). For the $LiBH_4$ compound, the data obtained from literature EIS measurements of ball-milled $LiBH_4$, have been excluded in the calculation of the average value. Note that for $Li_5(BH_4)_3NH$ only one measurement has been reported in the literature. Therefore, the value reported in **Table 3.4**, is not an average value, but corresponds to the value associated to the single measurement reported by Wolczyk et al.[41]. In some cases, the confidence interval for E_A is > 0.05, which is relatively high compared to the corresponding values for E_A (*i.e.* up to 10%) and confirms the existence of a large scatter in experimental results from different sources.

Compound	**σ at 30 °C** (S cm^{-1})		**E_A (eV)**		**ln σ_0**	
$LiBH_4$	9.5×10^{-9}	$\pm 2.07 \times 10^{-9}$	0.75	± 0.07	16	± 2
$LiNH_2$	5.36×10^{-11}	$\pm 4.11 \times 10^{-11}$	0.98	± 0.06	19	± 2
Li_2NH	3.66×10^{-4}	$\pm 8.92 \times 10^{-5}$	0.60	± 0.04	21	± 2
$Li_2NH_2BH_4$	1.01×10^{-4}	$\pm 1.63 \times 10^{-5}$	0.69	± 0.06	23	± 2
$Li_4(NH_2)_3BH_4$	1.54×10^{-4}	$\pm 4.09 \times 10^{-5}$	0.37	± 0.02	10.1	± 0.6
$Li_5(BH_4)_3NH$	1.29×10^{-7}	$\pm 8.33 \times 10^{-8}$	0.73	± 0.03	18	± 2

Table 3.4. *The average values of Li-ionic conductivity at 30 °C, activation energy (E_A) and ln σ_0 obtained by the statistical analysis performed for the different investigated complex hydrides.*

3.2.2. Comparison between computed and experimental data

Possible relationships between values obtained experimentally and reported in the literature, (*e.g.* ionic conductivity at 30 °C and activation energy) and values calculated from the theoretical approaches output are investigated, in order to obtain some insight into the link occurring between Li^+ ion conductivity and the topological properties of the corresponding crystal structures.

To investigate this point, theoretical results for the defect formation and migration energies, previously reported in the literature, for $LiBH_4$, $LiNH_2$ and Li_2NH, has been collected in **Table 3.5**. Note that no data have been found in the literature for $Li_2BH_4NH_2$, $Li_4BH_4(NH_2)_3$, and $Li_5(BH_4)_3NH$ compounds, so the analysis has been limited to $LiNH_2$, $LiBH_4$ and Li_2NH complex hydrides. **Table 3.5** reports also the E_m and E_f calculated in this work.

	Ref	**E_f Li_i^+ or V_{Li}^-(eV)**	**E_f Frenkel pair (eV)**	**Min. distance (Frenkel pair)**	**E_m (eV)**	**E_A (eV)**
$LiNH_2$	(85)	0.51	0.65	0.85 Å	0.2-0.3	0.71-0.81
	(86)	0.57	0.72	/	0.46	1.03
	(87)	0.52	0.79	/	0.44	0.96
	(88)	0.49$^{\#}$	0.97	/	0.22-0.42	0.71-0.91
	(89)	/	/	/	0.38	/
	PW	0.45	0.90	∞	0.46	0.91
o-$LiBH_4$	(90)	0.5	0.95	4.2 Å	0.3	0.8
	(30)	0.6$^{\#}$	1.2 0.88	∞ 4 Å	0.1-0.3	0.7-0.9
	PW	0.5	1.0	∞	0.30	0.80
Li_2NH	(89)	0.24$^{\#}$	0.48	/	0.17-0.47	0.41-0.71
	PW	0.37	0.74	∞	0.32	0.69

$^{\#}$Calculated dividing by 2 the E_f Frenkel pair. PW stands for "Present Work"

Table 3.5. *Defect formation and migration energies reported in the literature and calculated in this work for the considered systems. E_f is the formation energy for a single vacancy (V_{Li}^-), or equivalently for a single interstitial Li_i^+ and for a Frenkel couple (see the text for details). E_m is the migration energy of Li ions calculated in this work. Where available, the minimum distance between the vacancy and the interstitial atom in a Frenkel couple is also reported. Note that the formation energy of Frenkel pair with finite distance (or not reported in the original paper) do not equal two times the formation energy of a single defect. E_A has been calculated by adding to the E_m the calculated E_f for a single vacancy.*

Cho et al.[30] reported similar E_m values for $LiBH_4$, in the range 0.1-0.3 eV, depending on the diffusion mechanism and paths. As discussed in **Chapter 1** (see paragraph 1.5.1) this value in similar to the one calculated for the hexagonal phase (0.31 eV)[29]. The value of 0.3 eV reported by Hoang et al.[90] is matching our result. For $LiNH_2$, several results are available from different authors within the range 0.20-0.46 eV, with our calculated value falling in the range, but close to the highest value.

The relevant possible defects for Li-ion conductions are neutral lithium vacancies (V_{Li}), neutral lithium interstitials (Li_i) and the corresponding plus/minus one charged defects (V_{Li}^-, V_{Li}^+, Li_i^-, Li_i^+). In all studies reported in **Table 3.5** and in the present work, the combination of V_{Li}^- and Li_i^+, also known as a Frenkel pair, has been found to be the most stable. We then assume this as a common mechanism for all examined compounds.

Regarding the defect formation energies, it is worth noting that different approaches can be used to obtain such energies from the DFT calculations. For example, most of the values in **Table 3.5** have been calculated following an approach proposed by Van de Walle et al.[69], and used in our own calculations. This method has been used in refs.[85–90]. Another approach can be used for computing the formation energy of defect pairs, such as Frenkel or Schottky couples, used by. Cho et al.[30]

Note that for $LiNH_2$, several theoretical values are available, and a certain scatter can be observed in **Table 3.5**. As different computational parameters and program codes were used, it is difficult to clearly identify possible reasons for these differences, which can be considered as differences in the experimental measurements. Note also that, in some cases,[30,85,90] a specific distance was assumed between the vacancy and the interstitial in the Frenkel couple, which may account for part of the discrepancies found.

In order to estimate the activation energy, the energies of formation for V_{Li}^- calculated in this work (**Table 3.5**) have been added to the calculated migration energy and the results are reported in the last column in **Table 3.5**.

A comparison between computed and experimental values for the activation energy for $LiNH_2$, $LiBH_4$ and Li_2NH complex hydrides is shown in **Figure 3.3**.

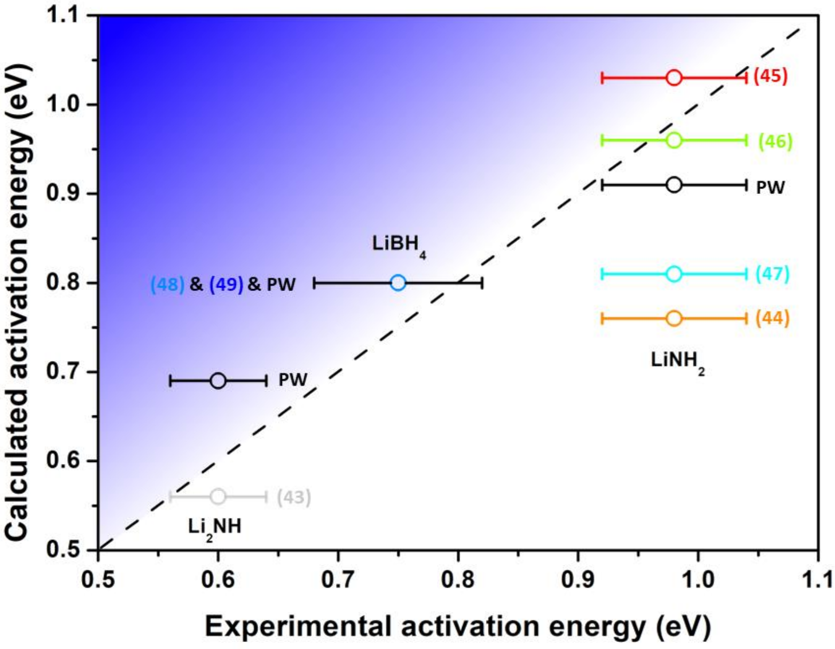

Figure 3.3. *Activation energy calculated as a function of the values obtained from the statistical analysis of literature data, where different colors indicates different references, PW ("present work") indicates the data calculated in this work. The dashed line is a guide for the eyes to show the correspondence of calculated and experimental values.*

A satisfactory correspondence between theoretical and experimental values can now be observed when considering the experimental error bar. Despite the large scatter observed in both experimental and theoretical values, it appears reasonable to confirm that the Li-ion conduction mechanism theoretically considered in this work is realized in the complex hydrides.

3.3. Conclusions

In this chapter the energy of migration of the $LiBH_4$, Li_2NH, $Li_2BH_4NH_2$, $Li_4BH_4(NH_2)_3$ and $Li_5(BH_4)_3NH$ structures have been calculate by theoretical approaches. In addition, a statistical analysis of the literature data has been performed for each compound in order to obtain the average values for the activation energy, ln σ_0 and Li-ion conductivity at 30 °C., that will be used in the following chapter as a reference. A correlation between the experimental and calculated values for Li-ion mobility has been evidenced for $LiNH_2$, $LiBH_4$ and Li_2NH complex hydrides, suggesting that the topological analysis can adequately explain the ion conductivity in complex hydrides.

Chapter 4.

Theoretical and Experimental Study of LiBH4-LiBr Phase Diagram

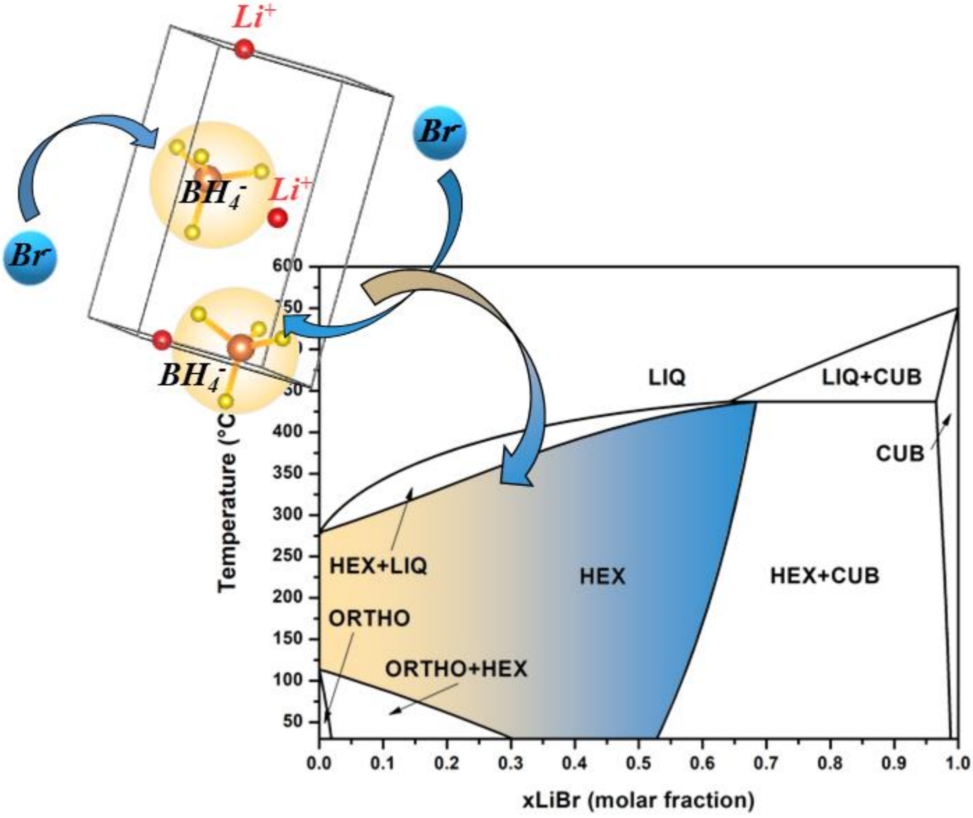

4.1. Introduction

The use of the Calphad[58] approach allows the determination of different thermodynamic properties, *e.g.* heat capacity (C_p),[25,91] and the definition of phase diagrams as a function of temperature and composition.[92,93]

Regarding the binary $LiBH_4$-LiBr phase diagram, few experimental data and no thermodynamic characterizations are present in the literature. Therefore, in the present chapter, we explore this binary system, combining experimental and theoretical techniques, in order to determine the binary phase diagram. Literature, experimental and ab-initio data have been used for a thermodynamic assessment of the system using the Calphad approach and the assessment allows to establish phase stabilities and limits of solubility in a wide temperature and composition range.

4.2. Results and discussion

4.2.1. Synthesis

$LiBH_4$ (purity >95% from Sigma-Aldrich) and LiBr (purity >99% from Sigma-Aldrich), were mixed in different ratios and by different methods, as reported in **Table 4.1**. LiBr were previously dried by heating at 120 °C under dynamic vacuum, in order to avoid the presence of the phase $LiBr{\cdot}H_2O$.[94]

Name	Composition		Synthesis
	$LiBH_4$	LiBr	
s1	0.7	0.3	BM 1.5 h + AN 2h 250 °C
s2	0.6	0.4	BM 1.5 h + AN 2h 250 °C
s3	0.5	0.5	BM 1.5 h + AN 2h 250 °C
s4	0.4	0.6	BM 1.5 h + AN 2h 250 °C
s5	0.6	0.4	Hand mixed

Table 4.1. *Composition and synthesis conditions of the samples prepared.*

All samples were mixed for periods of 10 min of milling separated by 2 min breaks (in order to reach the equilibrium conditions), at 350 r.p.m. Samples were annealed (AN) at 250 °C for 2 h in a quartz tube under static vacuum, with a heating/cooling rate of 5 °C/min.

4.2.2. Monophasic samples

Recently, the hexagonal solid solution h-Li$(BH_4)_{1-\alpha}(Br)_\alpha$ has been demonstrated to be stable in the range $0.3 < x < 0.5$.[39,77] Samples ***s1***, ***s2*** and ***s3*** have been synthetized in order to verify the monophasic zone limits reported in literature.

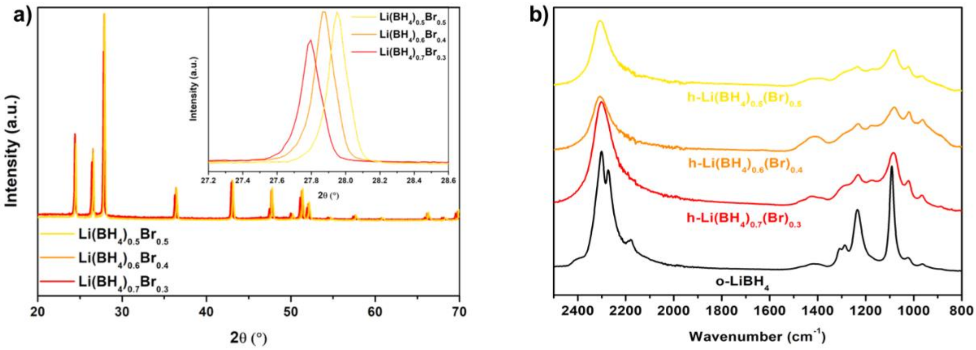

Figure 4.1. *a) PXD patterns of the monophasic samples,* ***s1, s2*** *and* ***s3*** *inside the solubility range of the h-Li$(BH_4)_{1-\alpha}(Br)_\alpha$ hexagonal solid solution. b) IR–ATR spectrum of pure $LiBH_4$ (bottom) and of samples* ***s1, s2*** *and* ***s3****.*

Figure 4.1a shows PXD pattern of the samples ***s1***, ***s2*** and ***s3***, after the synthesis (ball milling followed by a thermal treatment). In all patterns, the high temperature phase of $LiBH_4$ is stabilized at room temperature and it is the only phase present. The hexagonal solid solutions have smaller cell parameters with respect to pure $LiBH_4$, indicating the presence of bromide anions inside the structure. In fact, the radii of Br anions are smaller, compared to BH_4^- (Br^-=1.96 Å with respect BH_4^-=2.03 Å).[36]

In order to study the changes in the vibrational properties of lithium borohydride, due to the stabilization of the hexagonal phase by halide additions, IR-ATR spectroscopy was performed on samples ***s1***, ***s2*** and ***s3*** and the result is shown in **Figure 4.1b**, together with the spectrum for pure o-$LiBH_4$. The IR-ATR spectrum of as-received o-$LiBH_4$ shows two main absorption bands, corresponding to the B–H stretching (2400–2000 cm^{-1} region) and the B–H bending (1600–800 cm^{-1} region) vibrational modes, as reported in the literature.[94–98] IR-ATR spectrum of solid solution samples shows differences in the BH_4^- bending and stretching regions, with respect to the spectrum of o-$LiBH_4$, *i.e.* a decrease of the number of the components related to $\tilde{\nu}_2$ and $\tilde{\nu}_3$ fundamental modes. Furthermore, new peaks are present at ~1170 cm^{-1} and 1020 cm^{-1}, indicating a slight shift of the fundamental modes of BH_4^- owing to the presence of Br^- anions, according to the literature.[94,98] Finally, it is worth noting that pure halide vibrational modes cannot be observed in the investigated spectral range.

4.2.3. h-$LiBH_4$-LiBr biphasic zone

In order to define the composition limits of the bromide rich biphasic zone, samples ***s4*** has been synthetized by mechanochemical treatment followed by a suitable annealing.

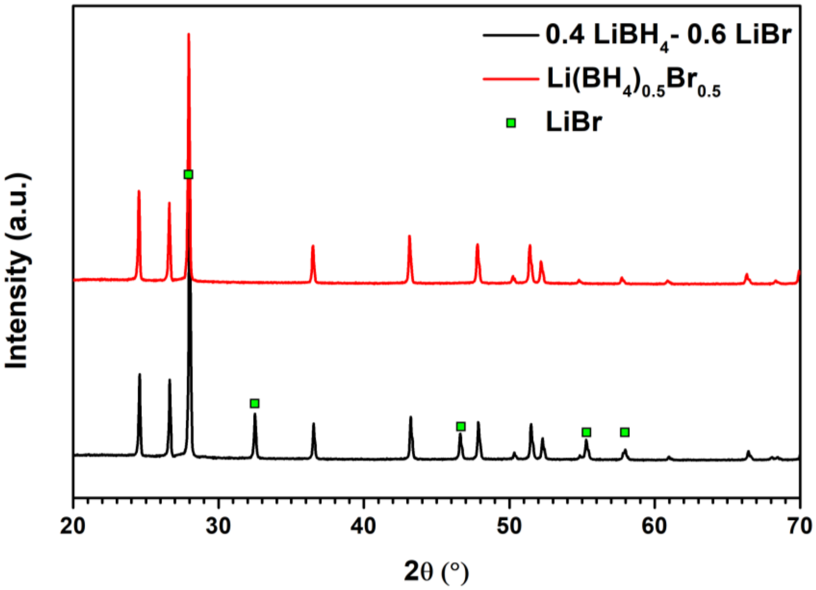

Figure 4.2. *PXD patterns of the monophasic samples* ***s3*** *(red line), inside the solubility range of the h-$Li(BH_4)_{1-\alpha}(Br)_\alpha$ hexagonal solid solution, and sample* ***s4*** *(black line).*

Figure 4.2 show the PXD pattern of sample ***s4*** collected after the synthesis, while the pattern of sample ***s3*** is shown for comparison. The PXD analysis of sample ***s4*** shows that two different phases are stable: h-$Li(BH_4)_{1-x}(Br)_x$ hexagonal solid solution and pure cubic LiBr ($Fm\bar{3}m$). It is possible to exclude any solubilization of BH_4^- inside the cubic structure of the LiBr, since the cell parameter of the cubic phase (a = 5.5082 Å) is equal to that of pure LiBr. The lattice parameter of the pure LiBr (a = 5.5035 Å) has been obtained by a Rietveld refinement of the starting material. In **Figure 4.2**, for the sample ***s4***, the lattice paraments of the hexagonal solid solution are slightly smaller than for the sample ***s3*** (a = 4.1853 Å c = 6.6915 Å for sample ***s4*** and a = 4.1935 Å c = 6.7019 Å for sample ***s3***), indicating that a the solubility limit of the h-$Li(BH_4)_{1-\alpha}(Br)_\alpha$ monophasic zone can be redefined slightly higher that $x<0.5$.

In order to explore the evolution of the biphasic zone limits as a function of temperature, a *in situ* SR-PXD measurement was performed on sample ***s4*** (**Figure 4.3**).

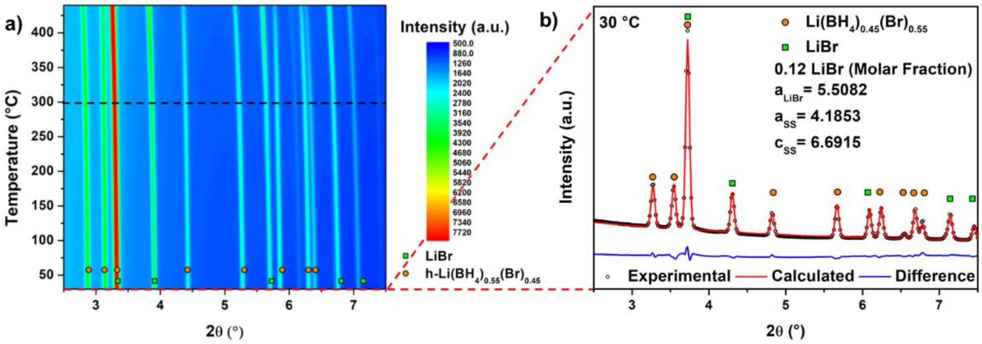

Figure 4.3. *a) in situ SR-PXD data for sample* ***s4*** *heated from RT to 450 °C (heating rate 5 °C/min). b) Rietveld refinement of sample* ***s4*** *at RT (R_{wp} 3.23 %).*

In order to obtain the structural information and composition of the h-$Li(BH_4)_{1-\alpha}(Br)_{\alpha}$ as a function of temperature, Rietveld refinement has been performed on PXD patterns measured at different temperatures. Starting from the pattern collected at R*T* (**Figure 4.3b**), in the refinement, the hexagonal solid solution has been considered isostructural to the hexagonal polymorph of $LiBH_4$ ($P6_3mc$),[26] which was used as initial structural model. The room temperature lattice parameters of the h-$Li(BH_4)_{1-\alpha}(Br)_{\alpha}$ hexagonal solid solution further confirms the higher Br^- content than sample ***s3***. In fact, in *R*T pattern (**Figure 4.3b**), the h-$Li(BH_4)_{1-\alpha}(Br)_{\alpha}$ lattice parameters are smaller compared to those obtained for sample ***s3***. Initially, the Br^- occupied the same *2b* site of the BH_4^- anions (x = 0.3333, y = 0.6667, z = 0.553)[26], but after the refinement a small increase of the z coordinate was detected. In this worth nothing that the strong X-ray scattering of the Br^- give an unambiguous and robust identification of the position and occupancy of the anion. The position of the Br^- anion after the refinement was x = 0.3333, y = 0.6667 and z = 0.605 and the occupancy equal to 0.55, throughout the temperature range. The difference in the *z* position was already detected by Cascallana-Matias et al.[39], confirming the goodness of the refinement.

The molar fraction of the LiBr at room temperature has been evaluated to be equal to about 0.12, while that of the h-$Li(BH_4)_{1-\alpha}(Br)_\alpha$ is equal to 0.88. These results are in agreement considering the molar balance:

$$f\ Li(\alpha\ BH_4 \cdot (1-\alpha)\ Br) + (1-f)\ LiBr = 1 \tag{4.1}$$

where f and $(1-f)$ are the molar fractions of the hexagonal solid solution h-$Li(BH_4)_{1-\alpha}(Br)_\alpha$ and of the LiBr, respectively; α and $(1-\alpha)$ are the molar fractions in the hexagonal structure, that is, occupancy, of BH_4^- and Br^-, respectively. Resolving the molar balance, considering the composition $Li(BH_4)_{0.45}(Br)_{0.55}$ or the phases molar fraction, the results confirm the output of the Rietveld refinement. These results indicated that a solubility stability range of $0.3<x<0.55$ for $Li(BH_4)_{1-x}(Br)_x$ can be defined at R*T*.

Once the structure and composition were resolved, by the Rietveld refinement it was possible to evaluate the lattice constants and the unit cell volume of the two phases as a function of temperature, and results are shown in **Figure 4.4a**. **Figure 4.4b** shows the phases molar fraction as a function of temperature.

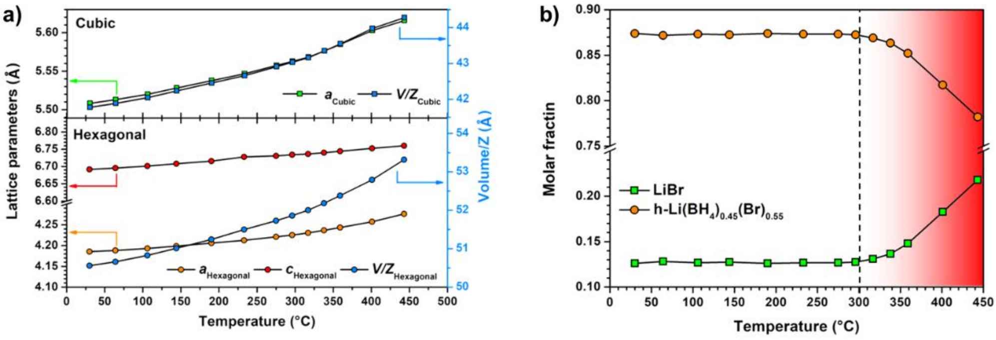

Figure 4.4. *a) lattice parameters and unit cell volume (V/Z) as a function of temperature for the two phases. b) Molar fraction as a function of the temperature.*

Below 300 °C, in situ SR-PXD (**Figure 4.3**) shows that no further solubilization of Br^- into h-$Li(BH_4)_{1-\alpha}(Br)_\alpha$ occurs. In fact, the molar fractions, calculated by Rietveld refinement, of the cubic LiBr, as well as of the hexagonal solid solutions, remains practically constant (**Figure 4.4b**). Above 300 °C, the molar fraction of the LiBr increases, indicating that a possible decomposition of the hexagonal solid solution occurred. It is possible to assume that during the decomposition, the LiBr is de-solubilized from the hexagonal solid solution. The Rietveld refinement results obtained for the last pattern collect during the fast cooling, at about 170 °C, exclude a possible melting of the hexagonal solid solution (**Figure 4.5**). In fact, the molar fractions of the two phases is slightly higher than that obtained at 450 °C, 0.23 of LiBr, indicating that the decomposition likely proceeds also during the cooling.

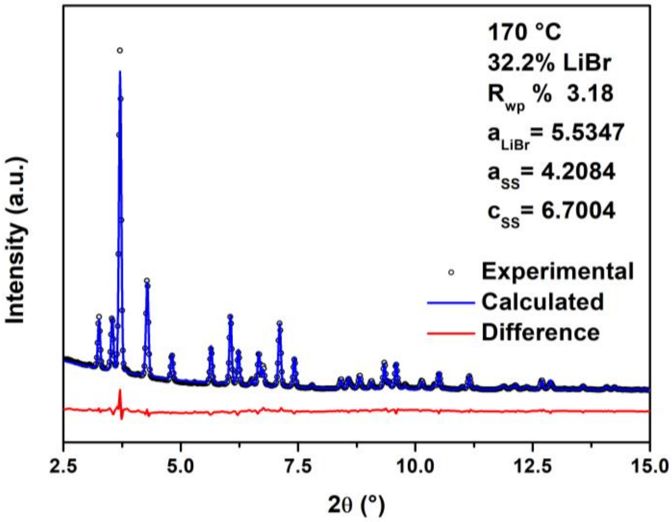

Figure 4.5. *Rietveld refinement of sample* ***s4*** *at 170 °C during the cooling ramp* (R_{wp} *3.18 %).*

The volumetric thermal expansion coefficient of the pure hexagonal $LiBH_4$ phase has been reported to be equal to $\alpha = 2.9 \times 10^{-4}$ K^{-1},[99] and can be define as:

$$\frac{\Delta V}{V} = \alpha \times \Delta T$$

From the data reported in **Figure 4.4a** we estimate a volumetric thermal expansion coefficient for the $Li(BH_4)_{0.45}(Br)_{0.55}$ hexagonal solid solution equal to 1.13×10^{-4} K^{-1}, indicating that the presence of the Br^- slightly reduces the volumetric thermal expansion coefficient of the hexagonal phase. Arnbjerg et al.[100] also reported, for h-$Li(BH_4)_{1-\alpha}(Cl)_\alpha$ solid solution, a reduction of the volumetric thermal expansion coefficient (1.33×10^{-4} K^{-1} for $Li(BH_4)_{0.71}(Cl)_{0.29}$ and 1.99×10^{-4} K^{-1} for $Li(BH_4)_{0.58}(Cl)_{0.42}$). On the other hand, the volumetric thermal expansion coefficient of the LiBr has been reported to be equal to 1.5×10^{-4} K^{-1},[101] and it was calculated equal to 1.31×10^{-4} K^{-1} for sample ***s4***, in agreement with the literature data, confirming, indirectly, the value of α calculated for the $Li(BH_4)_{0.45}(Br)_{0.55}$ solid solution.

Figure 4.6 shows that lattice parameters and the unit cell volume (V/Z) as a function of the molar fraction of the bromide inside the h-$Li(BH_4)_{1-\alpha}(Br)_\alpha$ hexagonal solid solution. These values have been calculated by Rietveld refinement of the PXD of samples ***s1***, ***s2*** and ***s3***, together with that of the R*T* SR-PXD pattern of sample ***s4***. The lattice parameters and the unit cell volume linearly decrease increasing the bromide concentration, according to the difference in the anion dimensions. By a linear fit it was possible to define three equations describing the lattice parameters and cell volume as a function of the bromide content inside the hexagonal solid solution. With the value of the volumetric thermal expansion coefficient of the hexagonal $LiBH_4$, it was possible to extrapolate the value of volume equal 106.5 Å^3 at R*T* (corresponding to a unit cell volume of 53.3 Å^3). The value of the cell volume is higher with respect that of sample ***s1*** (51.8 Å^3), further confirming the reduction of the volume due to the formation of the solid solution.

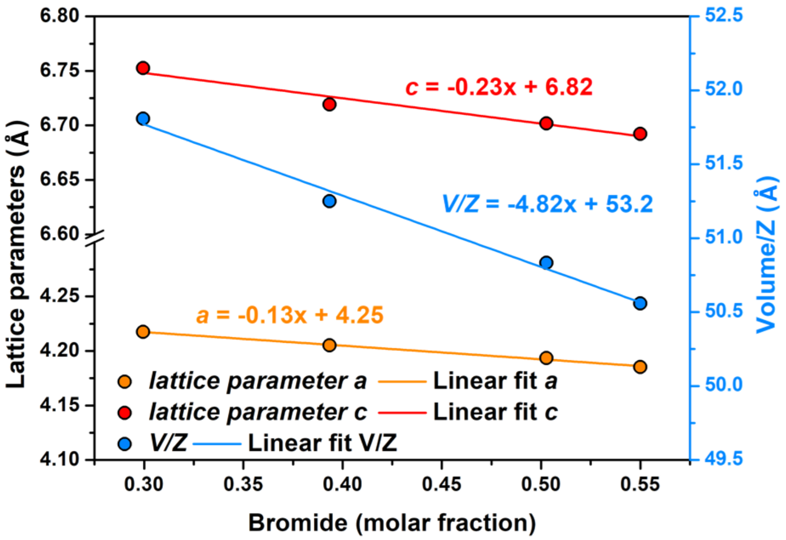

Figure 4.6. *Lattice parameters and unit cell volume (V/Z) as a function of the bromide (molar fraction) content inside the monophasic h-Li(BH$_4$)$_{1-\alpha}$(Br)$_\alpha$ hexagonal solid solution. Equations reported was obtained by the linear fit of the data.*

4.2.4. Enthalpy of Mixing

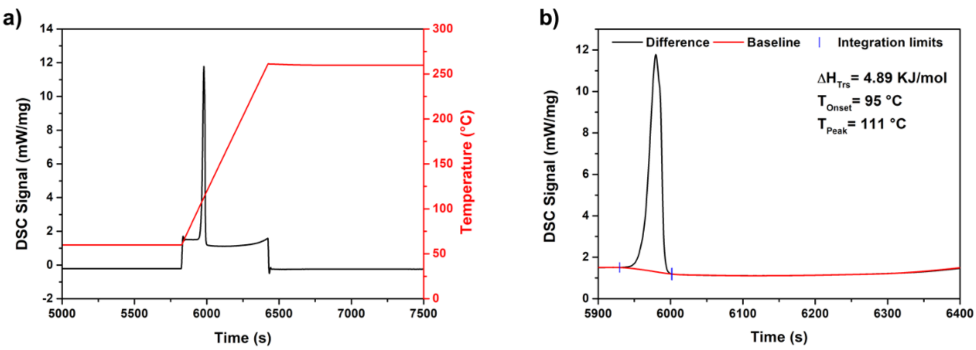

Figure 4.7. *HP-DSC trace of LiBH$_4$ heated at 20 K/min from RT to 260 °C followed by a 2.5 h isotherm at 260 °C.*

Figure 4.7. shows the DSC signal of pure LiBH$_4$. The integration of endothermic peak, due to the phase transition, at T_{Peak}= 111 °C (T_{Onset} = 95 °C)

provides a transition enthalpy (ΔH_{Trs}) of 4.89 KJ/mol. This value, as well as the T_{Peak} and T_{Onset}, is in agreement with the average value reported by El Kharbachi et al.[25] (5.3 ± 0.9 KJ/mol).

In order to assess the $LiBH_4$-LiBr phase diagram, a value of enthalpy of mixing is needed. For this reason, sample ***s5*** has been prepared by hand mixing (HM) LiBr and $LiBH_4$ in molar fraction 0.4-0.6, respectively, in an agate mortar for about 5 min, in order to avoid the formation of the hexagonal solid solutions. In fact, Rude et al.[94] reported that a small amount of h-$Li(BH_4)_{1-\alpha}(Br)_\alpha$ was already stabilized at R*T*, after 15 min of HM. **Figure 4.8** shows the Rietveld refinement of sample ***s5*** HM, indicating that the mixture is formed by 71 % of LiBr that correspond to a molar fraction of 0.38, in agreement with the composition prepared. It is worth noting that due to the high difference in the scattering factors the quantitative analysis possesses a quite high error. In any cases, the pattern shows that the only two phases present after the HM are pure cubic LiBr and pure orthorhombic $LiBH_4$.

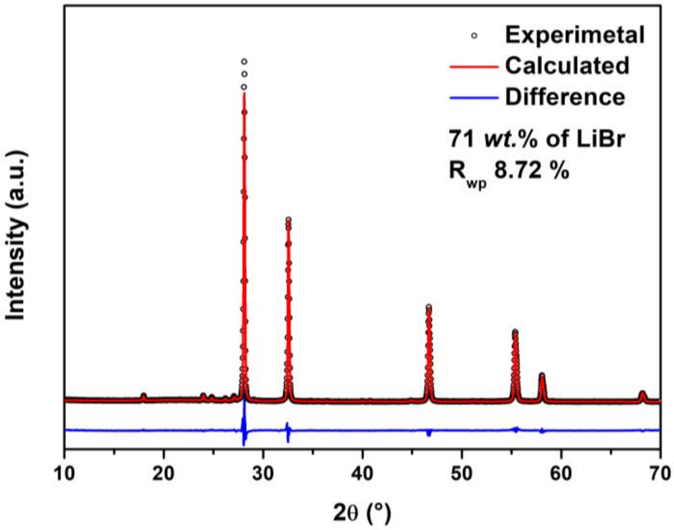

Figure 4.8. *Rietveld refinement of sample* ***s5*** *after 5 min of HM.*

Samples ***s5*** was analyzed using DSC in order to detect the enthalpy of mixing. The fixed temperature program was the following: a) a 2.5 h isotherm, near room temperature (60 °C), in order to equilibrate the DSC signal; b) a fast heating ramp (20 °C/min), in order to reduce the temperature range in which the thermal activated process could occurs and c) a 2.5 h isotherm, at the maximum temperature reached during the heating ramp (250 ÷ 350 °C), to ensure that the possible activated thermal process could be completed. The same temperature program was repeated two times, in order to have a DSC signal that can be use as baseline for the signal integration.

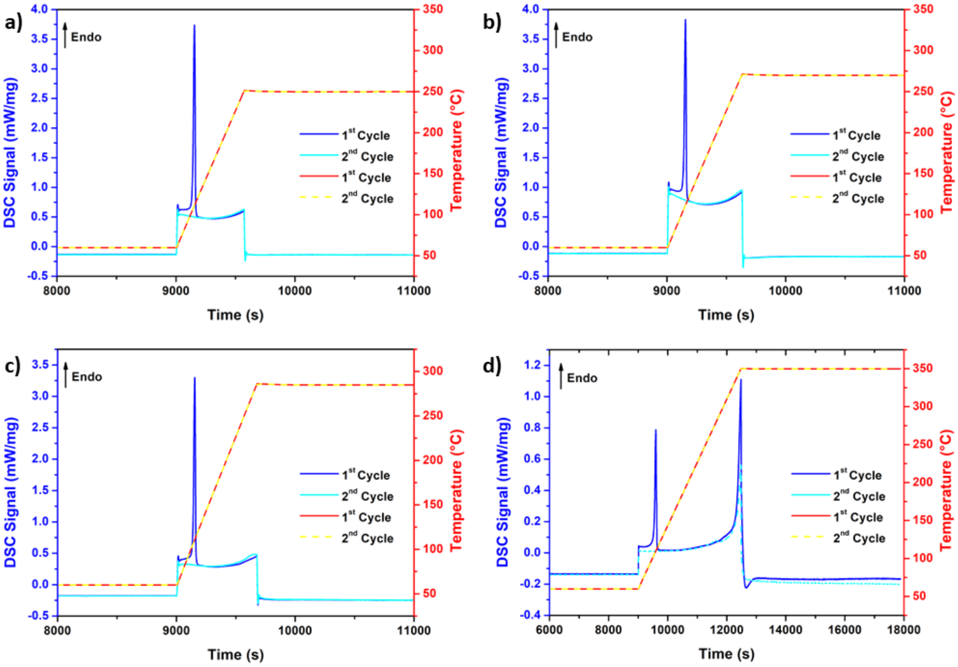

Figure 4.9. *HP-DSC trace of sample **s5** heated at 20 K/min from RT to a) 250 °C, b) 270 °C c) 285 °C and d) 350 °C, followed by an isotherm at the same temperature.*

Figure 4.9 shows the DSC signal of sample **s5** using different isotherm temperature (250, 270, 285 and 350 °C). The isotherm temperatures have been chosen in order to be close to the melting temperature of the pure $LiBH_4$

(278 °C)[25], in order to maximize the range in which the exothermic event could be detected.

In all the calorimetric analysis of sample **s5**, during the heating ramp, the endothermic peak due to the phase transition of the $LiBH_4$ was detected. The peak (T_{Peak}) and onset (T_{Onset}) temperatures, as well as the enthalpies of transition (ΔH_{Trs}), for the different calorimetric analysis (**Figure 4.9**), are reported in **Table 4.2**.

T Isotherm	ΔH_{Trs+Cp}	ΔH_{Trs}	ΔH_{Trs}	ΔH_{Cp}	T_{Peak}	T_{Onset}	ΔH_{Mix}^{a}	ΔH_{Mix}^{b}
°C	KJ/mol	KJ/mol	KJ/mol_{LiBH_4}	J/mol	°C	°C	J/mol	J/mol
250	3.71	3.01	5.02	744	111	93	-302	-302
270	3.52	2.83	4.72	684	111	94	-471	-471
285	3.35	2.69	4.48	660	111	95	-792	-636
350	/	2.71	4.51	/	110	95	/	

Table 4.2. *ΔH, peak and onset temperatures collected during the DSC analysis.*
[a] *integration terminated before the start of the high temperature isotherm.*
[b] *integration terminated when the exothermic at the ended.*

Another important evidence is that during the second cycle, the endothermic peak is not present anymore, meaning that the reaction of stabilization of the h-$LiBH_4$ phase, by the formation of the h-$Li(BH_4)_{1-\alpha}(Br)_\alpha$ solid solution, was completed after the first cycle, or at least that all the $LiBH_4$ is stabilized at R*T*. It is worth nothing that the cooling ramps, from the high temperature isotherms down to 60 °C, were collected, but they have been not reported since no thermal events were detected, confirming the formation of the solid solution.

Figure 4.9d shows that an additional endothermic peak at T_{Onset} slightly higher than 300 °C is present. This evidence indicates that, at temperatures higher than 300 °C, the sample starts to decompose, confirming the results reported in **Figure 4.3**. Differently form the other performed calorimetric analysis, during the high temperature isotherm (350 °C), the signal of the first and second cycle are not overlapped. The signal of the first cycle seems to show a continuous endothermic event, indicating that the decomposition proceeds also during the isotherm. In addition, during the second heating cycle the decomposition endothermic peak is still present. These results suggest that data obtained from these measurements cannot be used for further analysis.

Figure 4.9 shows that during the isotherm at 60 °C no thermal events were detected. In addition, excluding **Figure 4.9d**, the DSC signal during the first and the second cycle, in both isothermal steps (60 °C and high temperature), are perfectly overlapped. During the second cycle, no thermal events are present. Therefore, it was possible to use the second cycle ad a baseline for the integration of the endo/exothermic events present in the first cycle. The differences between the first and the second DSC scan, highlighting the integrated regions, are reported in **Figure 4.10**.

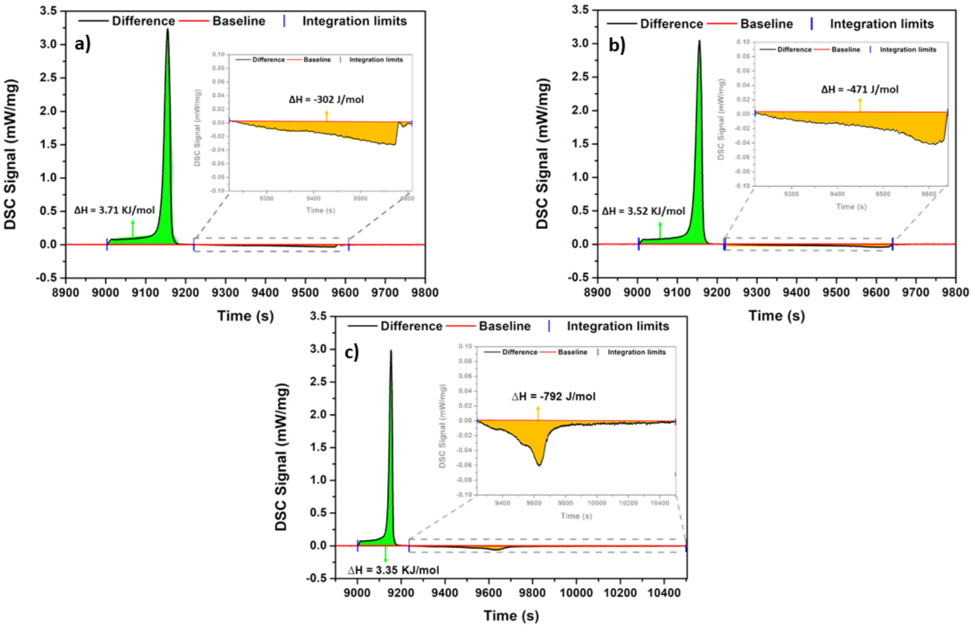

Figure 4.10. *Integration of the DSC signal after the subtraction of the second cycle from the first cycle for the calorimetric analysis with the isotherm at a) 250 °C, b) 270 °C and c) 285 °C.*

Figure 4.10 shows that the difference between the first and the second cycle of the calorimetric analysis is composed by an endothermic signal, based on two overlapped contributions, and an exothermic signal (see **Table 4.2** for the values of integrated signals). As said before, the endothermic signals can be assigned, in part, to the transition for the orthorhombic to the hexagonal phase of the pure $LiBH_4$. The second contribution to the endothermic event is present before the phase transition (**Figure 4.10**), in the temperature range of 60 to 120 °C. This difference can be explained considering that the molar heat capacity (C_p) of the orthorhombic phase is higher with respect the C_p of the hexagonal phase.[102] In fact, during the first cycle the $LiBH_4$ is still in the orthorhombic phase, while during the second one, the $LiBH_4$ have been stabilized in its hexagonal phase.

In **Table 4.2** the ΔH_{Trs+Cp} corresponds to the integration of the signal of the of the entire endothermic signal, thus including the two endothermic contributions (see also **Figure 4.10**). The values of ΔH_{Cp} refer to the contribution due to the difference in the heat capacity between the orthorhombic and hexagonal phase of the $LiBH_4$. Using the equations describing the heat capacity as a function of temperature, of the two phases of $LiBH_4$, reported by El Kharbachi et al.[102], it was possible to calculated the ΔH difference due to the different heat capacity observed in $LiBH_4$ for the two phases. The calculation performed provided a ΔH equal to 237 J/mol, in the temperature range of 60 to 120 °C, considering that the enthalpy can be described as:

$$\Delta H = \int_{T_1}^{T_2} C_p(T)\, dt \qquad (4.2)$$

Since the sample **s5** is composed also by LiBr, the C_p of this compound (48.112 J/mol K at RT, taken constant as a function of the temperature)[103] has been taken in account in the calculation, considering the LiBr molar fraction of the sample. It is worth noting that this value, *i.e.* 237 J/mol, is smaller with respect the values of ΔH_{Cp} obtained from the integration (660÷744 J/mol). This difference could be explained considering two factors. The first one is that the C_p of both the orthorhombic and hexagonal phase have been extrapolated to higher and lower temperature, respectively, with respect the phase transition temperature. In addition, it should be considered that, during the second cycle, the DSC signal refers to the h-$Li(BH_4)_{1-\alpha}(Br)_\alpha$ and no to the pure h-$LiBH_4$. Therefore, even though the LiBr C_p has been taken in account, the h-$Li(BH_4)_{1-\alpha}(Br)_\alpha$ could have a lower C_p value than the pure h-$LiBH_4$, leading to a higher difference.

The values of ΔH_{Trs}, normalized for the $LiBH_4$ molar fraction (KJ/mol_{LiBH4}), indicate that before the phase transition no solubilization occurs. In fact, the values obtained from the integration are comparable to that of the pure $LiBH_4$ (see **Figure 4.7**).

Figure 4.11 shows the overlapped DSC signals after the subtraction of the first and second signals. After the phase transition an exothermic event is present and it has been assigned to the enthalpy of mixing (ΔH_{Mix}) due to the formation of the h-$Li(BH_4)_{1-\alpha}(Br)_\alpha$ solid solution. Results of the integration are reported in **Table 4.2**.

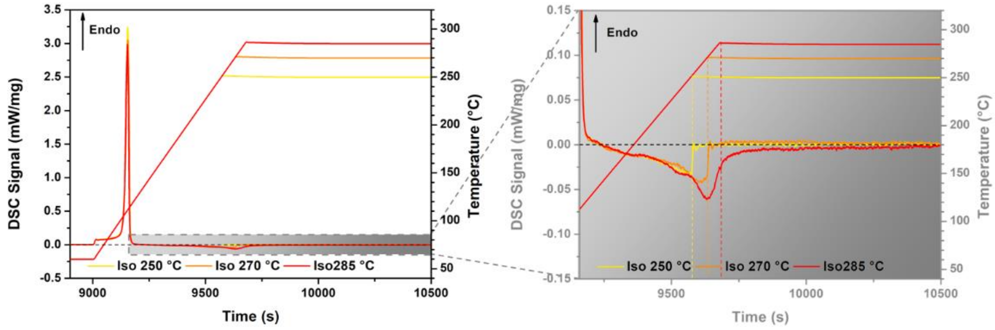

Figure 4.11. *Overlapping of the DSC signals after the subtraction of the second cycle from the first cycle for the calorimetric analysis.*

Increasing the temperature of the isotherm, the exothermic peak further increases in enthalpy, reaching a maximum value when the isotherm was set at 285 °C. Regarding the calorimetric analysis in which the isotherm were fixed at

250 °C and 270 °C, the exothermic event closed at the end of the heating ramp, while for the isotherm at 285 °C, the exothermic event proceeds during the isotherm.

In order to understand if ΔH_{Mix} equal to 792 J/mol could be assigned to the complete reaction of formation of h-$Li(BH_4)_{0.6}(Br)_{0.4}$, the reaction was followed by PXD (**Figure 4.12**).

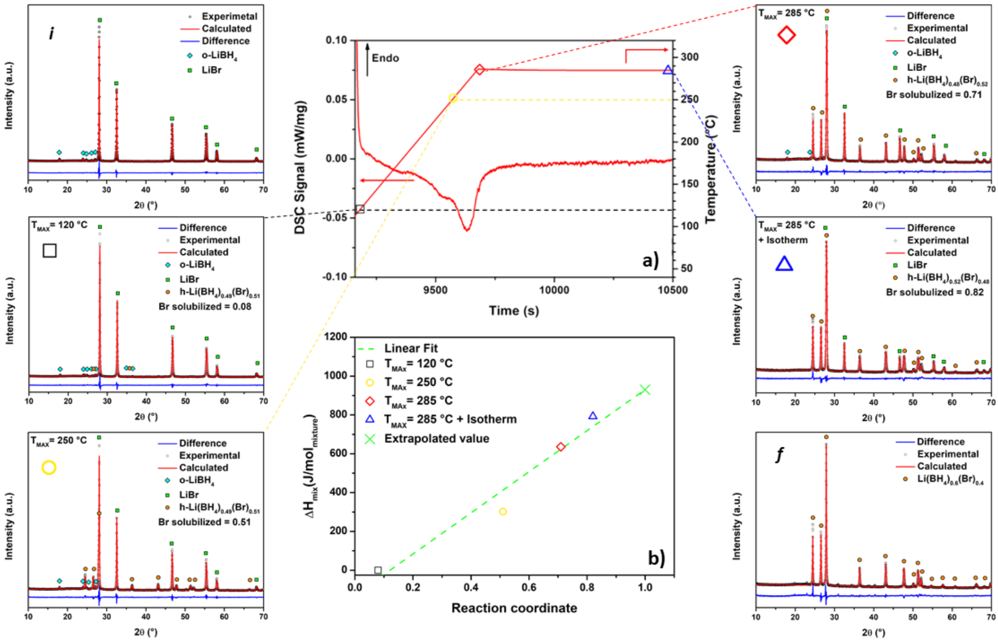

__Figure 4.12.__ a) DSC signal after the subtraction of the second cycle from the first cycle for the calorimetric analysis. b) Reaction coordinate as a function of the ΔH_{Mix}. Pattern collected after i) HM; f) complete calorimetric analysis (__Figure 4.9c__) (; square) heating to 120 °C; circle) heat treatment to 250 °C; rhombus) heating to 285 °C; triangle) heating to 285 °C followed by an 8 min isotherm at the same temperature.

Figure 4.12a shows the DSC signal (also reported in **Figure 4.11** and **Figure 4.10c**) and the indication, on the temperature signal, of at which temperature the patterns were collected. The patterns ***i*** and ***f***, were collected after HM (see also

Figure 4.8) and after the calorimetric analysis reported in **Figure 4.9c**. The pattern ***f*** shows that, after the calorimetric analysis, the reaction was completed and the h-$Li(BH_4)_{0.6}(Br)_{0.4}$ solid solution has been fully formed. The other patterns in **Figure 4.12** were collected when sample **s5** has been heated up (20 K/min) to the target temperatures. The heating ramp was always preceded by a 2.5 h isotherm at 60 °C in order to reproduce the temperature program of the calorimetric analysis. The pattern indicated by the square symbol, was collected after a heating of sample **s5** to 285 °C followed by an 8 min of isotherm at the same temperature. The 8 min of isotherm corresponds to the time in which the integration was ended (**Figure 4.10c**), in order to have a PXD pattern collected when the exothermic event ended and that corresponds to a ΔH_{Mix} equal to 792 J/mol. For each pattern the Rietveld refinement was performed. The composition of the $Li(BH_4)_{1-x}(Br)_x$ hexagonal solid solutions was calculated by a using the equations describing the hexagonal lattice petameters as a function of the bromide content (see **Figure 4.6**) and the lattice parameters obtained by a preliminary refinement. Once the composition of the hexagonal solid solution has been defined, it was possible to obtain the wt.% and the molar fractions of the different phases. Increasing the maximum temperature reached during the heating, the amount of LiBr and o-$LiBH_4$ continuously decreased, while the amount of the hexagonal solid solution increased. The composition of the hexagonal solid solution remained constant during the reaction and equal to about $x = 0.51$.

The reaction coordinate in **Figure 4.12b** corresponds to the fraction of the LiBr solubilized in the hexagonal solid solution and it has been calculated using the molar fraction of residual cubic LiBr obtained by the Rietveld refinement.

Since samples were treated with the same temperature programs used during the DSC analysis, it was possible to correlate the reaction coordinate obtained by Rietveld refinement with the ΔH_{Mix} values reported in **Table 4.2**. The enthalpy of mixing corresponding to the pattern collected after the heating at 120 °C has been consider equal to zero. Actually, a small amount of the hexagonal solid solution was already observed, suggesting that the reaction might be already initiated during the heating up to the $LiBH_4$ phase transition. The pattern collected after the heating to 285 °C followed by an isotherm of 2 h (pattern ***f***) , that corresponds with the end of the integration and a ΔH_{Mix} equal to 792 J/mol, shows that the 82 % of the LiBr has been solubilized in the solid solution. This result indicates that the value of the ΔH_{Mix} obtained by the calorimetric analysis cannot be assigned to a complete solubilization reaction. **Figure 4.12b** shows the ΔH_{Mix} values reported in **Table 4.2** as a function of the reaction coordinate. By a linear fit of the data collected, the value corresponding to a complete formation reaction of h-$Li(BH_4)_{0.6}(Br)_{0.4}$ solid solution has been estimated equal to 930 J/mol (**Figure 4.12b**). Using a confidence of 95 %, the value can be reported with an error of ± 160 J/mol, *i.e.* 0.9 ±0.2 KJ/mol.

4.2.5. Phase Diagram

The thermodynamic assessment, performed by Dr. Erika Michela Dematteis, of the pseudo-binary $LiBH_4$–LiBr system focused on the modelling of hexagonal solid solution phase supported by experiments. Few literature and experimental data available together with already assessed database have been used as the input for a preliminary assessment and description of the pseudo-binary phase diagram. The corresponding orthorhombic and hexagonal LiBr end-members have been determined by DFT calculations and the obtained experimental enthalpy of mixing for the hexagonal solid solution allowed to determine the interaction parameter. LiBr turns out to be mostly insoluble into the orthorhombic phase and $LiBH_4$ has been considered insoluble into the cubic phase. The literature only reports few data supporting the solubility of LiBr into the orthorhombic structure up to 0.10

molar fraction. For this reason, positive parameters in the excess Gibbs free energy function of the orthorhombic and cubic phase have been introduced.

Figure 4.13 shows the calculated $LiBH_4$–LiBr phase diagram as a result of the preliminary Calphad analysis and assessed parameters. Interaction parameters (Ω) for the solid solutions based on the regular solution model, as well as the stability end LiBr members, are reports in the inset. Results evidenced a solubility limited to 0.01 molar fraction for LiBr into orthorhombic $LiBH_4$. It is worth noting that the experimental solubility limits of the hexagonal phase on the LiBr-rich side is in good agreement with the *in-situ* experimental investigation, even if they deviate towards higher content of LiBr at high temperatures. Since the liquid phase has not been assessed but considered as ideal (Ω_{LIQ} = 0), the calculated values of the liquidus temperature at 0.5 results overestimated with respect to the literature value.

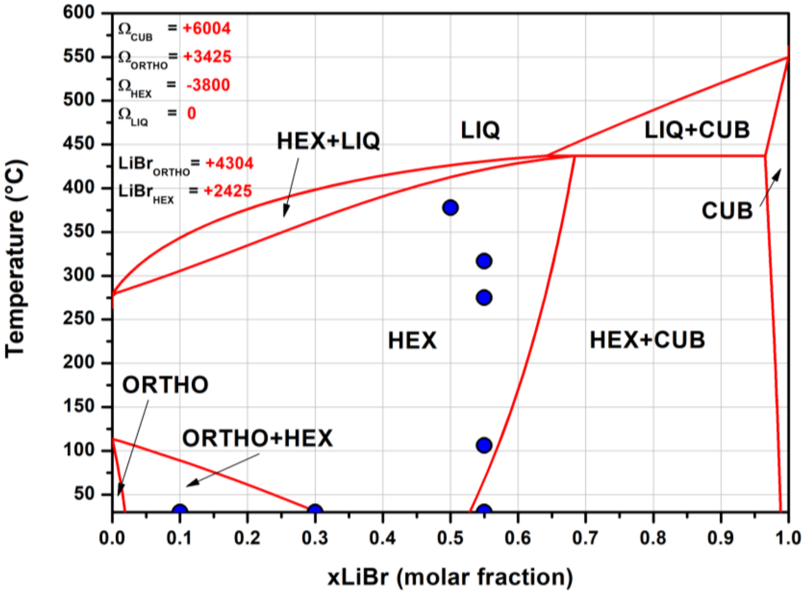

Figure 4.13. *Assessed phase diagrams for the $LiBH_4$–LiBr system. Blue circles indicate the experimental and literature data used for the assessment.*

4.3. Conclusions

The binary phase diagram $LiBH_4$-LiBr has been explored by means of PXD, *in situ* SR-PXD and DSC. The monophasic zone of the hexagonal $Li(BH_4)_{1-x}(Br)_x$ solid solution has been defined equal to $0.3 < x < 0.55$ R*T*. The monophasic zone has been explored and the dependence of the lattice parameters on the solid solution composition has been described by suitable equations. The biphasic zone $Li(BH_4)_{0.45}(Br)_{0.55}$-LiBr has been explored by *in situ* SR-PXD and defined practically constant up to 300 °C. In fact, at this temperature, a decomposition of the hexagonal solid solution occurs, and it has been confirmed also by calorimetric analysis. In order to perform the assessment of the phase diagram, a value of the enthalpy of mixing has been estimated.

A hand mixed sample ($0.6LiBH_4$-0.4LiBr) has been analysed by DSC in order to detect the exothermic peak due to the reaction of the formation of the hexagonal solid solution. Using the ΔH_{Trs} obtained by the calorimetric analysis, it was possible to conclude that the stabilization of the hexagonal solid solution starts after the phase transition (110 °C). The combination of calorimetric analysis and PXD allowed to define a ΔH_{Mix} equal to 0.9 ±0.2 KJ/mol for the complete formation of the $Li(BH_4)_{0.6}(Br)_{0.4}$ solid solution.

Finally, the $LiBH_4$-LiBr pseudo binary system has been described in all composition and temperature range, however the liquid phase has been considered as ideal resulting in an overestimated liquidus temperature at 0.5.

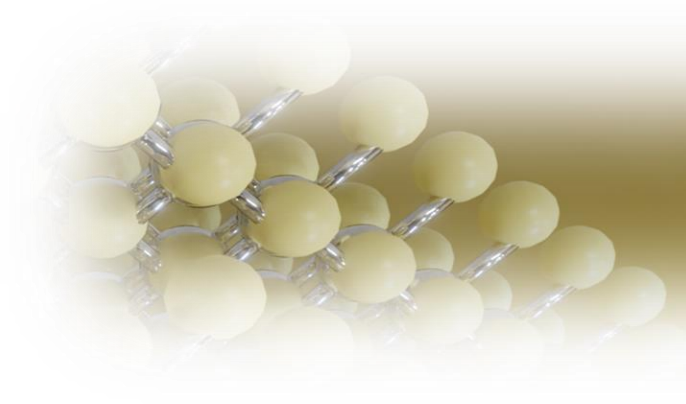

Chapter 5.

Phase Stability and Fast Ion Conductivity in the Hexagonal $LiBH_4$–LiBr–LiCl Solid Solution

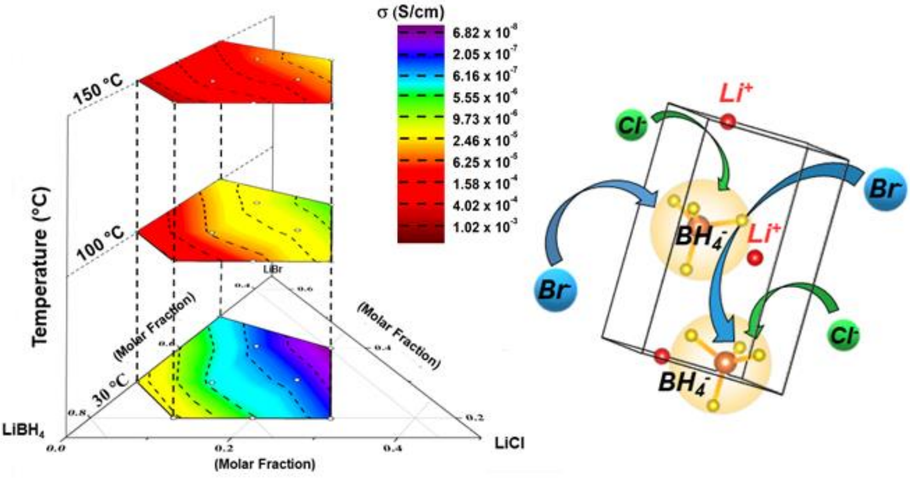

5.1. Introduction

As described in the introduction, halogenation represents a successful strategy to stabilize the $LiBH_4$ conducting phase at R*T* and in the previous chapter the $LiBH_4$-LiBr phase diagram has been defined. However, only the heavy Br^- and I^- anions seems to achieve this task, while the use of the lighter Cl^- would be preferred. For this reason, in order to reduce the mass of the electrolyte in solid-state batteries, *i.e.* increase the energy density, the ternary $LiBH_4$-LiBr-LiCl phase diagram was investigated and it is discussed herein. An insight on the system is presented, in order to understand phase stability and the solubility limits of the hexagonal solid solution. Once the phase diagram has been defined, a complete electrochemical characterization as a function of the halogen content has been performed, in order to assess how halogenation affect the operational voltage window.

5.2. Results and discussion

5.2.1. Synthesis

$LiBH_4$ (purity > 95 % from Sigma-Aldrich), LiBr (purity > 99 % from Sigma-Aldrich), LiCl (purity > 99 % from Merck) and LiI (purity > 99 % from Sigma-Aldrich) were mixed in different ratios, as reported in **Table 5.1**. Before mixing, LiCl and LiBr were dried at 120 °C in a furnace under dynamic vacuum. Sample ***s4*** was prepared to verify the Vegard's law in the LiBr-LiCl binary system[104].

All mixtures were ball milled for 1,5 hours at 350 r.p.m., in periods of 10 min separated by 2 min breaks. In order to reach the equilibrium conditions, all samples were annealed (AN) at 250 °C for 2 h in a quartz tube under static vacuum, with a heating/cooling rate of 5 °C/min.

Sample Name	Composition (Molar Fraction)		
	$LiBH_4$	LiBr	LiCl
s1	0.33	0.33	0.33
s2	0.38	0.33	0.29
s3	0.38	0.33	0.29
s4		0.50	0.50
s5	0.80	0.20	
s6	0.70	0.30	
s7	0.60	0.40	
s8	0.50	0.50	
s9	0.40	0.60	
s10	0.60	0.20	0.20
s11	0.22	0.58	0.20
s12	0.22	0.19	0.59
s13	0.60	0.10	0.30
s14	0.21	0.69	0.10
s15	0.40	0.50	0.10
s16	0.40	0.40	0.20
s17	0.49	0.41	0.10
s18	0.50	0.30	0.20
s19	0.50	0.20	0.30
s20	0.60	0.30	0.10
s21	0.70	0.20	0.10

Table 5.1. *Composition of the investigated samples.*

5.2.2. Structural characterization

Figure 5.1a shows PXD patterns of a $LiBH_4$-LiBr-LiCl equimolar mixture (sample ***s1***) after BM (bottom) and after AN (top). After ball milling (BM), the high temperature hexagonal phase of $LiBH_4$ is already stabilized at R*T*, but main diffraction peaks of the orthorhombic phase, stable at *RT,* are still present in the pattern.

The relative amount of the hexagonal phase cannot be directly determined by Rietveld analysis at this stage, since its composition is unknown. Nevertheless, it is hereby confirmed that a mechanochemical treatment of the $LiBH_4$-LiBr-LiCl system allows the stabilization of the high temperature hexagonal phase at *RT*. However, the presence of PXD peaks related to LiBr and LiCl $Fm\bar{3}m$ cubic phase (*a* = 5.50 Å and *a* = 5.14 Å, respectively) denotes an incomplete solubilization of halide anions.

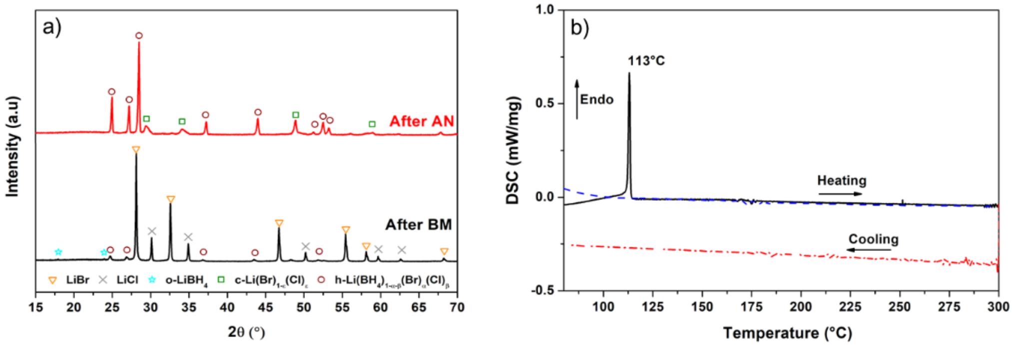

Figure 5.1. *a) X-ray diffraction patterns of sample* ***s1*** *after ball milling (bottom) and after annealing (top). b) HP-DSC trace of sample* ***s1*** *after ball milling. The solid and dash-dot lines show the results of the first heating and cooling ramps, respectively, while the dash line refers to the second heating ramp.*

The calorimetric analysis of the sample ***s1*** after BM (**Figure 5.1b**) shows an endothermic peak due to the phase transition of $LiBH_4$ at 113 °C (peak temperature), confirming the presence of residual orthorhombic $LiBH_4$ in the ball milled mixture. The peak integration provides an enthalpy of transition of 1.5 kJ/mol. This value corresponds to about 28 % of the tabulated value (5.3 kJ/mol),[105] indicating that most of $LiBH_4$ is already in the hexagonal phase after BM. The observed phase transition is irreversible, suggesting that a heating up to 300 °C is suitable to promote the complete stabilization of $LiBH_4$ in the hexagonal phase as solid solution. In fact, PXD performed after AN (**Figure 5.1a**), does not show any diffraction peak related to the orthorhombic phase.

Bragg peaks of the hexagonal solid solution after AN are shifted to higher 2θ values compared those observed after BM (**Figure 5.1a**), suggesting a contraction of the unit cell. In the PXD pattern obtained after AN, a cubic phase corresponding to the $Li(Br)_{1-\varepsilon}(Cl)_{\varepsilon}$ cubic solid solution is still present, with a lattice parameter (a = 5.25 Å) lying between those of pure LiCl and LiBr compounds. The LiBr-LiCl phase diagram reported in literature,[104] presents a complete solid solution and a liquidus curve with a thermal minimum at 522 °C, y_{LiCl} = 0.36. Equimolar sample ***s4*** was prepared to verify the Vegard's law in the LiBr-LiCl binary system. An *in situ* PXD measurement was using a Aanton-Paar XRK 900 reactive chamber, under dynamic vacuum (**Figure 5.2**). Patterns were collected in both heating and cooling ramp, in a temperature range RT < T < 400 °C with a heating/cooling rate of 5 °C/min. During heating, the cubic solid solution is formed at 250 °C, resulting stable during the cooling down to RT, confirming the reported phase diagram.[104] The cell parameter obtained by Rietveld refinement does follow the Vegard's law.

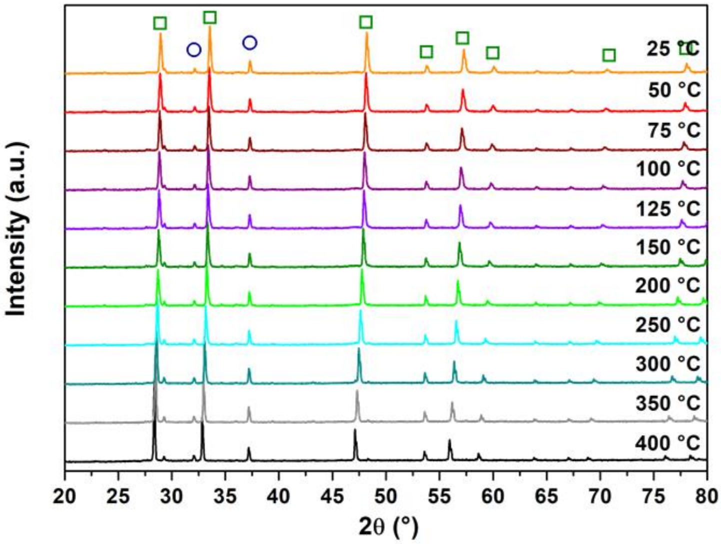

Figure 5.2. *PXD patterns of sample* ***s4*** *collected during the cooling ramp. Calcium Oxide (CaO, purity >99% from Sigma-Aldrich) was used as internal standard. Symbols: blue circles refers to CaO, while green squares to* $Li(Br)_{1-\varepsilon}(Cl)_{\varepsilon}$.

Having verified that Vegard's law holds for such system, the composition of the cubic solid solution (**Figure 4.1a**) resulting from the value of the lattice parameter corresponds to $LiBr_{0.28}Cl_{0.72}$.

In order to calculate the composition of the hexagonal solid solution in the mixture, the following molar balance has been solved:

$$f\ \times Li[\alpha Br\cdot\beta Cl\cdot(1-\alpha-\beta)BH_4]+(1-f)\ \times Li[\varepsilon Cl\cdot(1-\varepsilon)Br]=1 \qquad \mathbf{(5.1)}$$

where f and $(1-f)$ are the molar fractions of the hexagonal solid solution $Li(BH_4)_{1-\alpha-\beta}(Br)_{\alpha}(Cl)_{\beta}$ and of the cubic solid solution $Li(Br)_{1-\varepsilon}(Cl)_{\varepsilon}$, respectively; α, β and $(1-\alpha-\beta)$ are the molar fractions in the hexagonal structure, *i.e.* occupancy, of Br^-, Cl^- and BH_4^- anions, while ε and $(1-\varepsilon)$ refers to molar fraction of Br^- and Cl^- in the cubic structure of the $Li(Br)_{1-\varepsilon}(Cl)\varepsilon$ solid solution. Equation (**5.1**) is not solvable with a linear method. In order to overcome this problem, a self-consistent iterative method has been applied. To start with, the occupancy of Cl- (β) in the hexagonal structure has been taken equal to 0.2 and the composition of Li(Br)1-ε(Cl)ε cubic solid solution, calculated from the lattice parameter as mentioned above, has been fixed (*i.e.* ε = 0.72). In this way, the equation $f\times\alpha+(1-f)\times 0.28=f\times\beta+(1-f)\times 0.72=0.33$ has been solved to obtain a starting value for the occupancy of Br^- (α) in the hexagonal structure. The estimated compositions of both phases (*i.e.* α, β and ε values) have been used as starting parameters for performing the Rietveld refinement.

For the Rietveld refinement of the PXD patterns, the structural model of the hexagonal polymorph of $LiBH_4$ (*P6₃mc*) was used to describe the structure of h-$Li(BH_4)_{1-\alpha-\beta}(Br)_{\alpha}(Cl)_{\beta}$ solid solution, where Br^- and Cl^- ions were constrained to lie on the same boron position (2*b* Wyckoff site). The value of the molar fraction (f) obtained from the refinement has been then used in equation (**5.1**) to obtain a new starting value for α. The process has been repeated recursively until a convergence was reached, leading to a relative phase fraction and compositions corresponding to 14 *wt.* % of c-$LiBr_{0.28}Cl_{0.72}$ solid solution and 86 *wt.* % of h-$Li(BH_4)_{0.39}Br_{0.33}Cl_{0.28}$ (**Figure 5.3**).

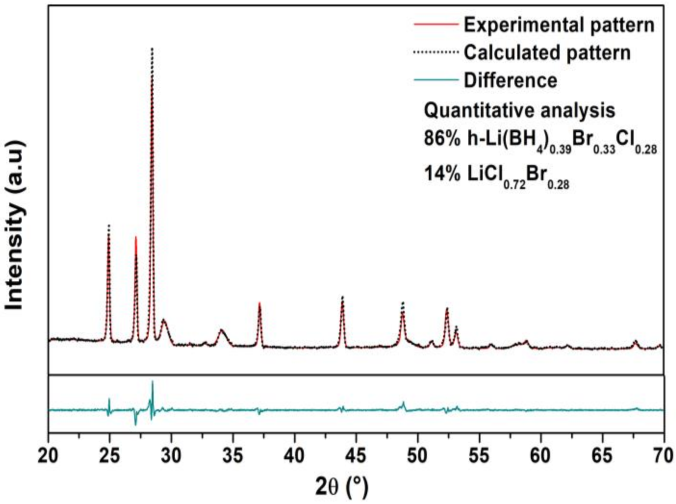

Figure 5.3. *Rietveld refinement of PXD pattern of sample* ***s1*** *after AN. (Rwp 11.66 %, χ 2.10).*

The lattice parameters of the hexagonal phase are a = 4.12 Å and c = 6.57 Å, corresponding to a cell volume equal to 96 $Å^3$.The value of cell volume of pure h-$LiBH_4$ at *RT* has been evaluated equal to 106 $Å^3$, using the volumetric thermal expansion coefficient of 2.9 $\times 10^{-4}$ K^{-1}.[99] A contraction of the cell volume of the hexagonal solid solution is expected after halogenation, due to the smaller ionic radii of Cl^- ($r(Cl^-)$ = 1.81 Å) and Br^- ($r(Br^-)$ = 1.96 Å)[106] compared to that of $BH4^-$ ($r(BH4^-)$ = 2.03 Å)[107-109].

On the basis of the calculated compositions of the hexagonal solid solution in sample ***s1***, a $(LiBH_4)_{0.39}(LiBr)_{0.33}(LiCl)_{0.28}$ (sample ***s2***) mixture has been synthetized to obtain a single phase hexagonal solid solution. **Figure 5.4a** shows the PXD diffraction patterns of the BM and AN sample. The results of the Rietveld refinement of AN sample is shown in **Figure 5.4b**.

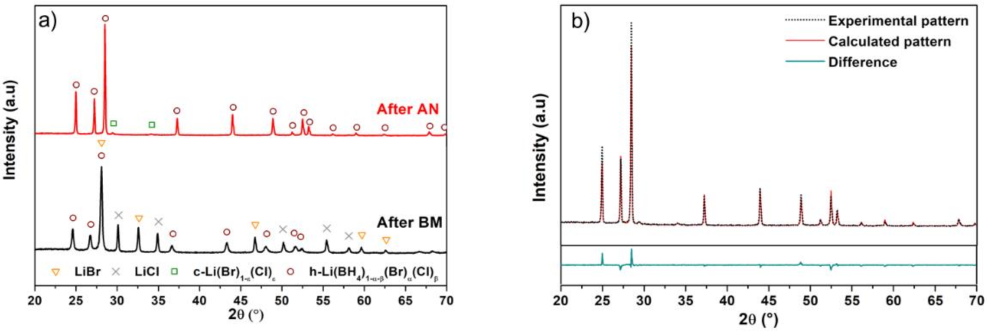

Figure 5.4. *a) X-ray diffraction patterns of* $(LiBH_4)_{0.39}(LiBr)_{0.33}(LiCl)_{0.28}$ *mixture (sample* ***s2****) after ball milling (bottom) and after annealing (top). b) Results of the Rietveld refinement of sample* ***s2*** *after AN (Rwp=8.34 %,* χ*=1.65).*

In the pattern of sample after BM, diffraction peaks of o-$LiBH_4$ are not present, indicating that all $LiBH_4$ is in the hexagonal phase. As evidenced in the PXD pattern of ***s2*** sample AN, the estimated limit of solubility for the ternary solid solution is confirmed by the presence of a basically single hexagonal phase (*i.e.* only 2 *wt.* % of $LiBr_{0.38}Cl_{0.62}$ is still present). For the first time, a single hexagonal solid solution of h-$LiBH_4$ containing two different halide anions (Br^- and Cl^-) has been obtained at R*T*. The stability of the solid solution was evaluated over time, *i.e.* after about one-year, at R*T* and a very similar X-ray diffraction pattern was obtained for the sample ***s2***, indicating long-term stability of the solid solution.

In order to study the changes in the vibrational properties of lithium borohydride, due to the stabilization of the hexagonal phase by halide additions, IR-ATR spectroscopy was performed on AN sample ***s2*** and the result is shown in **Figure 5.5**, together with the spectrum for pure o-$LiBH_4$. In fact, changes in the IR-ATR spectrum reflect a change in the site symmetry of the BH_4^- anions, due to the formation of a solid solution.

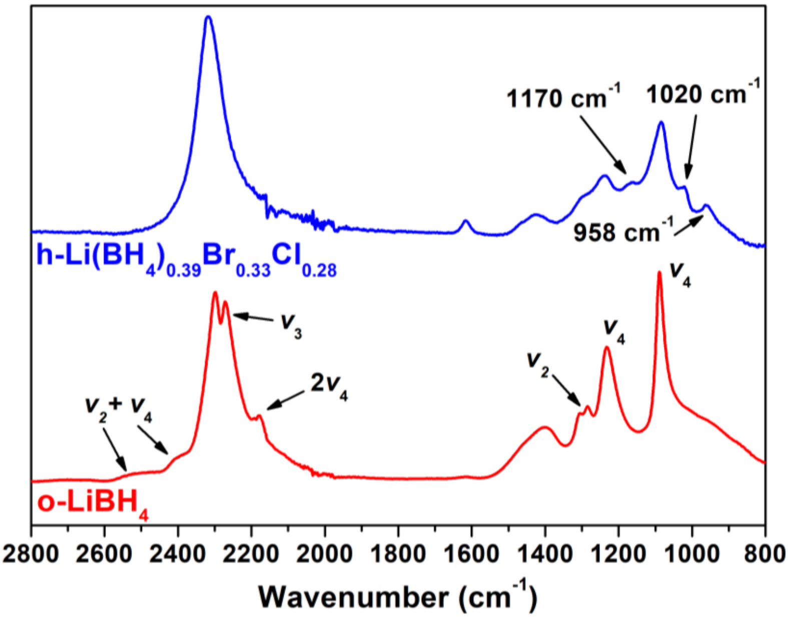

Figure 5.5. *IR-ATR spectrum of pure LiBH$_4$ (bottom) and sample* ***s2*** *after AN (top). IR active modes are indicated in the figure and described in the text.*

The isolated BH_4^- anion has an ideal tetrahedral symmetry, T_d. However, the vibrational modes are split in the crystalline state due to lowering of the site symmetry from T_d to C_s, *i.e.* the degenerate fundamental modes $\tilde{\nu}_2$, $\tilde{\nu}_3$, and $\tilde{\nu}_4$ split into several components.[94,110] The IR-ATR spectrum of as-received o-LiBH$_4$ shows two main sets of IR absorption bands, due to B–H stretching (2400–2000 cm^{-1} region) and B–H bending (1600–800 cm^{-1} region) vibrational modes, as reported in the literature.[94–98] In h-LiBH$_4$ structure, the BH_4^- anions have C_{3v} site symmetry and $\tilde{\nu}_3$ has only two components, while the mode $\tilde{\nu}_2$ is doubly degenerate.[94] Therefore, the changes in the spectrum of hexagonal solid solution could be related to the change of BH_4^- site symmetry.

The IR-ATR spectrum of sample **s2** after AN shows differences in the BH_4^- bending and stretching regions with respect to the spectrum of o-LiBH$_4$, *i.e.* a decrease of the number of the components related to $\tilde{\nu}_2$ and $\tilde{\nu}_3$ fundamental modes. A similar behaviour has been observed by Rude et al. for the hexagonal phase of $LiBH_4$ stabilized at *RT* by Br^-[94] and I^-[98] substitutions. Furthermore, new peaks are present at ~1170 cm^{-1}, 1020 and 958 cm^{-1}, indicating a slight shift of the fundamental modes of BH_4^- owing to the presence of Br^- and Cl^- anions, according to the literature.[94,98] Finally, it is worth noting that pure halides vibrational modes cannot be observed in the investigated spectral range.

Usually, both mechanical and thermal treatments are necessary to obtain a single lithium borohydride-halide hexagonal solid solution.[94,98,111] However, after 24 h of milling, a complete solid solution h-$Li(BH_4)_{0.667}Br_{0.333}$ was successfully obtained by Sveinbjörnsson et al.[39] In order to investigate the feasibility to form a 3-anions hexagonal phase only by mechanochemistry, the same composition of the sample ***s2*** was ball milled for different times (sample ***s3***).

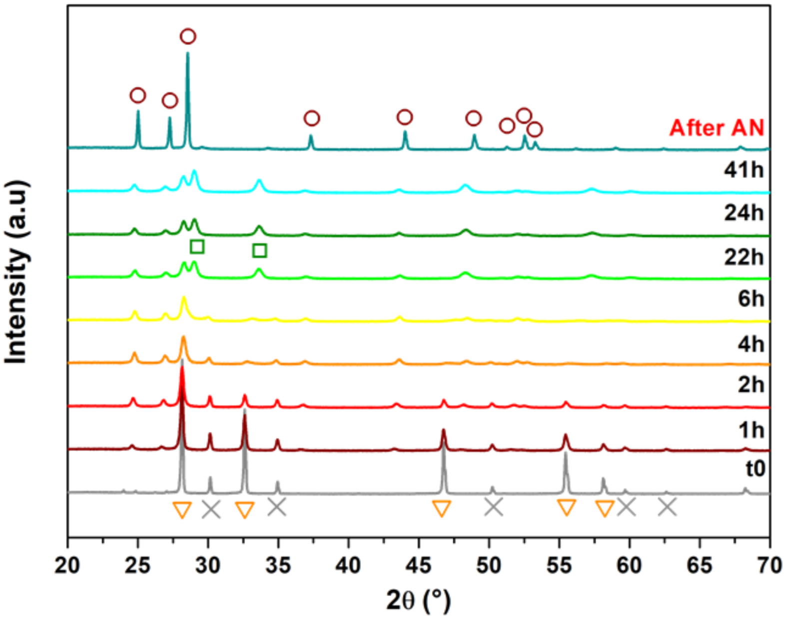

Figure 5.6. *Effect of the milling time on sample* ***s3****. Symbols: triangles LiBr; cross LiCl; circles h-*$Li(BH_4)_{1-\alpha-\beta}(Br)_\alpha(Cl)_\beta$*; squares* $Li(Br)_{1-\varepsilon}(Cl)_\varepsilon$.

Figure 5.6 shows the effect of the increasing milling time on the formation of the hexagonal solid solution. After 1 h of milling, the hexagonal solid solution is already formed, as observed for sample ***s2***. Upon further milling, the progressive dissolution of LiBr and LiCl into h-$LiBH_4$ is observed, as evidenced by a gradual intensity decrease of Bragg peaks of halide phases. The mechanochemical treatment alone failed to promote the complete solubility of both Br^- and Cl^- halide anions in the hexagonal solid solution. In fact, even after 41 h of ball milling, residual $Li(Br)_{1-\varepsilon}(Cl)_{\varepsilon}$ is still present, which disappears after annealing.

A small difference in ionic radius is promoting the formation of solid solutions.[112] Indeed, for $LiBH_4$-LiI and $LiBH_4$-LiBr systems, that have similar anionic radii, a significant miscibility is expected and confirmed experimentally, with the stability of the hexagonal phase at *RT*.[37,39,94,98] On the other hand, Cl^- anion is miscible in h-$LiBH_4$ only at temperatures close to 100 °C.[113] In fact, the radii of BH_4^- and Cl^- differ significantly. It can therefore be concluded that the presence of Br^- in the solid solution promotes the Cl^- solubilisation.

5.2.3. Solubility limits in the $LiBH_4$-LiCl-LiBr system

In order to have an optimized control of the synthesis process and to obtain single phase samples, the solubility limits at *RT* of the hexagonal solid solution in the $LiBH_4$-LiCl-LiBr system have been investigated. Several samples prepared by BM + AN (**Table 5.1**) have been analyzed by PXD, determining the phase amount and compositions by Rietveld refinement, following the procedure described above. By solving equation (**5.1**) (see paragraph 4.2.2) the solubility limits of the hexagonal solid solution were defined. The calculated mutual molar quantity of phases has been checked with respect to the level rule,[114] confirming the reliability of calculations.

As determined in **Chapter 4**, the $Li(BH_4)_{1-\alpha}(Br)_{\alpha}$ hexagonal solid solution is stable at *RT* as a single phase from $\alpha = 0.30$ to $\alpha = 0.55$. For concentrations

$\alpha > 0.55$, the hexagonal solid solution coexists with cubic LiBr (sample ***s9***). For the sample ***s9***, the lattice parameter of LiBr was refined as a_{LiBr} = 5.50 Å, which turns out equal to that of the pure compound, indicating no solubility of BH_4^- in the cubic structure of LiBr. For $\alpha < 0.3$, an orthorhombic o-$Li(BH_4)_{1-\alpha}Br_\alpha$ phase is present together with the hexagonal solid solution, with lower cell parameters with respect to those of pure o-$LiBH_4$, in agreement with Cascallana-Matias et al.,[39] who observed a single orthorhombic phase for $\alpha < 0.1$.

In order to define the solubility limits in the hexagonal $Li(BH_4)_{1-\alpha-\beta}(Br)_\alpha(Cl)_\beta$ solid solution, samples ***s10-s14*** were prepared. All samples are biphasic, containing both hexagonal and halide cubic solid solutions, with the exception of $(LiBH_4)_{0.6}(LiBr)_{0.2}(LiCl)_{0.2}$ (sample ***s10***), which shows a single hexagonal phase. In order to explore in details the hexagonal solid solution, the monophasic zone was mapped with seven different samples (sample ***s15-s21***), in which a single hexagonal phase was observed.

The maximum chloride concentration obtained in the h-$Li(BH_4)_{1-\alpha-\beta}(Br)_\alpha(Cl)_\beta$ solid solution amount to β = 0.31 in sample ***s13***, where h-$Li(BH_4)_{0.45}(Br)_{0.24}(Cl)_{0.31}$ phase coexists with the cubic solid solution c-$Li(Br)_{0.17}(Cl)_{0.83}$. $(LiBH_4)_{0.6}(LiBr)_{0.1}(LiCl)_{0.3}$ (sample ***s13***) contains pure LiCl and the hexagonal solid solution h-$Li(BH_4)_{0.62}(Br)_{0.1}(Cl)_{0.28}$, representing the limit of the biphasic zone.

Figure 5.7 shows the obtained ternary phase diagram at *RT*. The diagram is composed by: (*a*) hexagonal h-$Li(BH_4)_{1-\alpha-\beta}(Br)_\alpha(Cl)_\beta$ monophasic zone; (*b*) cubic c-$Li(Br)_{1-\varepsilon}(Cl)_\varepsilon$ monophasic zone (on LiBr-LiCl axis); (*c*) orthorhombic o-$Li(BH_4)_{1-\alpha}(Br)_\alpha$ monophasic zone (on $LiBH_4$-LiBr axis); (*d*) biphasic zone (*Cub+Hex*), in which are present h-$Li(BH_4)_{1-\alpha-\beta}(Br)_\alpha(Cl)_\beta$ in equilibrium with c-$Li(Cl)_{1-\varepsilon}(Br)_\varepsilon$; (*e*) biphasic zone (*Hex+Ort*), where h-$Li(BH_4)_{1-\alpha-\beta}(Br)_\alpha(Cl)_\beta$ and the orthorhombic solid solution (o-$Li(BH_4)_{0.9}Br_{0.1}$) are present; (*f*) biphasic zone (*LiCl+Ort*), containing o-$Li(BH_4)_{1-\alpha}Br_\alpha$ and LiCl; (*g*) triphasic zone, where h-$Li(BH_4)_{0.62}(Br)_{0.1}(Cl)_{0.28}$, o-$Li(BH_4)_{1-\alpha}Br_\alpha$ and pure LiCl phases are in equilibrium.

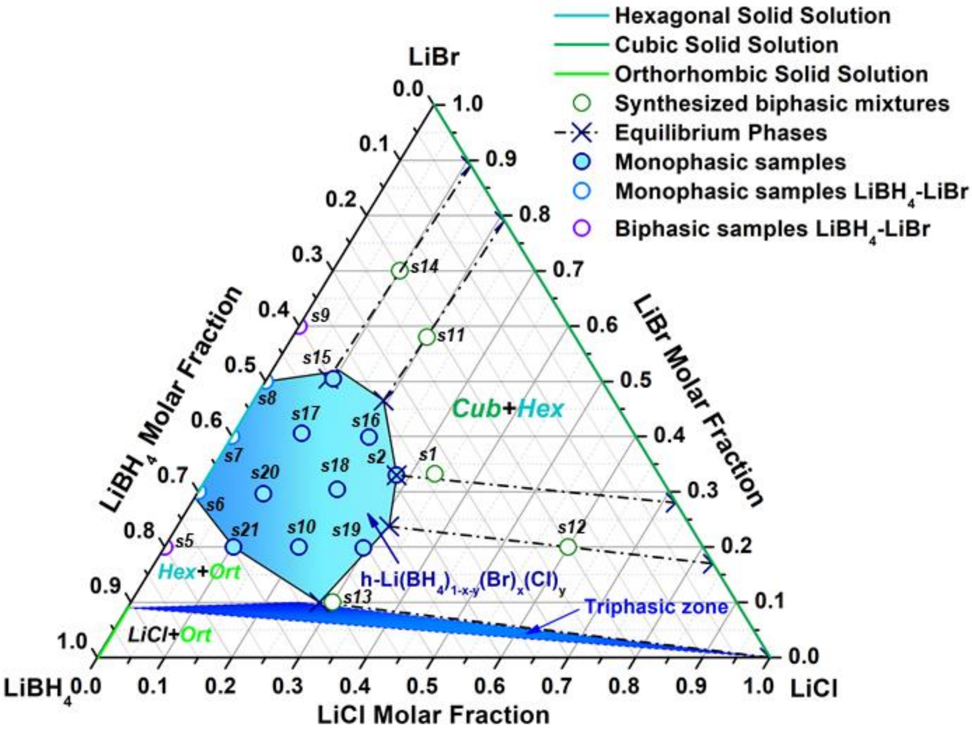

Figure 5.7. *Ternary phase diagram of $LiBH_4$-LiBr-LiCl system at room temperature, obtained by X-ray diffraction analysis. Light filled area is the monophasic zone of hexagonal $Li(BH_4)_{1-\alpha-\beta}(Br)_\alpha(Cl)_\beta$ solid solution. Dark filled area indicates a triphasic zone, where $Li(BH_4)_{0.62}(Br)_{0.1}(Cl)_{0.28}$, o-$Li(BH_4)_{0.9}Br_{0.1}$ and pure LiCl are present.*

Since the unit cell volume is expected to affect the Li-ion conductivity, as observed in different systems,[111,115,116] lattice parameters of h-$Li(BH_4)_{1-\alpha-\beta}(Br)_\alpha(Cl)_\beta$ solid solutions were determined from the Rietveld refinement. In order to highlight the effect of composition, the values of lattice constants and volume obtained for sample ***s6*** have been taken as a reference and data are reported as relative variations

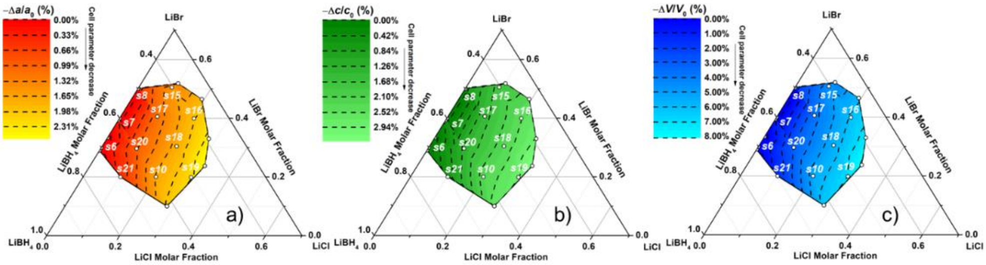

Figure 5.8. *RT maps of a) –(Δa)/a₀ % cell parameter b) –(Δc)/c₀ % c cell parameter and c) –(ΔV)/V₀ % volume of the hexagonal solid solution h-*$Li(BH_4)_{1-\alpha-\beta}(Br)_\alpha(Cl)_\beta$ *obtained by Rietveld refinement.* a_0, c_0 *and* V_0 *refer to the parameters of sample* ***s6*** *taken as a reference. Δ represents the variation of the cell parameters and volume with respect to the reference values. Dashed lines correspond of the values and lines shown in the legend.*

Figure 5.8, shows that both *a* and *c* lattice constants, as well as the volume, of the hexagonal solid solution decrease with increasing of the concentration of both halides, as discussed above. The contraction of lattice parameters is nearly linear with increasing Cl^- concentration. When Br^- replaces the borohydride anions, the decrease of lattice parameters and volume is less pronounced with respect to Cl^-.

5.2.4. Li-ion conductivity

In order to investigate the trend of Li-ion conductivity as a function of composition and temperature, temperature-dependent EIS measurements were performed. As an example, data obtained for sample ***s20*** are reported in **Figure 5.9**. The impedance spectrum is composed, close to room temperature (30 °C), by a single arc in the Nyquist plot (**Figure 5.9a**), while, at a higher temperature (110 °C), an additional linear dispersion is visible in the low frequency region (**Figure 5.9b**).

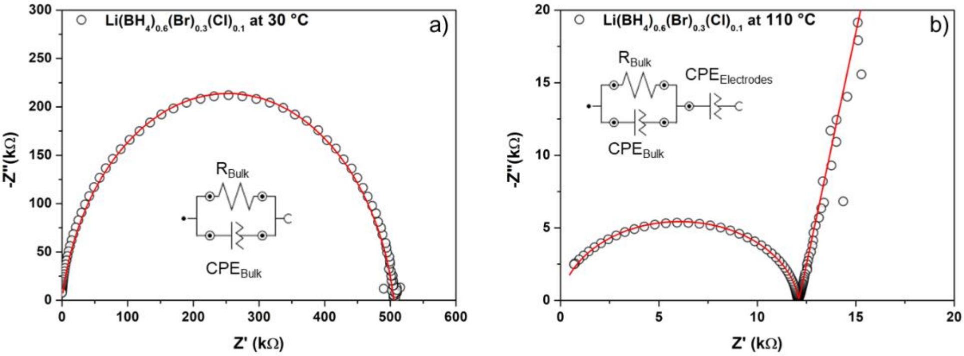

Figure 5.9. *Impedance spectra shown on the Nyquist plot for the sample **s20** collected at a) 30 °C and b) 110 °C. The insets show the equivalent electrical circuits used to fit the data.*

Results of Li-ion conductivity obtained for different compositions of the hexagonal solid solution as a function of inverse temperature are reported in **Figure 5.10**.

As expected, for single-phase samples containing the hexagonal solid solution, the change in the conductivity due to the polymorphic transition, as observed for pure $LiBH_4$, disappears. h-$Li(BH_4)_{0.7}(Br)_{0.2}(Cl)_{0.1}$ (sample ***s21***) shows the highest value for conductivity (1.3×10^{-5} S cm^{-1} at 30 °C) inside the ternary solid solution range. It is worth noting that this value is three orders of magnitude higher than that of pure $LiBH_4$ at *RT*. In any cases, considering also the binary solid solution, $Li(BH_4)_{0.7}(Br)_{0.3}$ (sample **s6**) shows the highest value for Li-ion conductivity at *RT*. As shown in **Figure 5.10**, the conductivity values for several compositions in the solid solution range are greater than that of pure hexagonal $LiBH_4$, in the same temperature range.

As shown in **Figure 5.10**, the conductivity increases with temperature, as expected for a thermally activated process. Plots of ln (σT) as a function of 1000/T show a linear trend, in agreement with equation (1). So, the activation energy (E_A) for Li-ion conductivity was obtained by a linear fit of the Arrhenius plot and the results are shown as a function of composition in **Figure 5.11**. The lowest values of activation energy are observed for the $LiBH_4$-LiBr solid solutions (*e.g.* 0.45 eV for sample ***s7***).

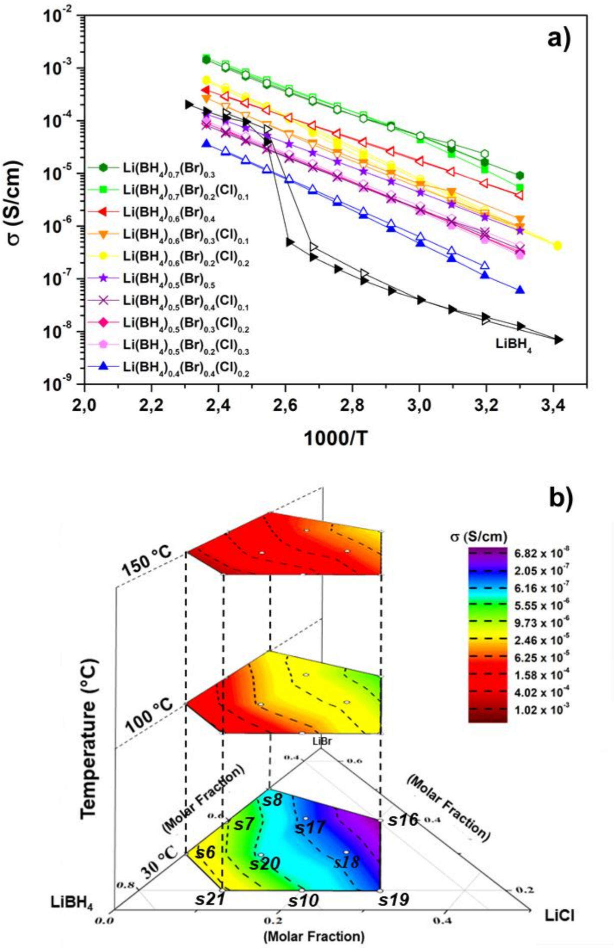

Figure 5.10. *a) Li-ion conductivity of samples in the hexagonal solid solution in the $LiBH_4$-LiBr-LiCl system. Open symbols represent the cooling ramp, close symbols the heating one. b) Contour map of Li-ion conductivity as a function of composition for three selected temperatures. Iso-conductivity dashed lines correspond to the values and lines shown in the legend.*

Collected data show that a correlation exists between composition and ionic transport properties, as represented by the Li-ion conductivity and activation energy. Decreasing the BH_4^- content in the hexagonal solid solution, the Li-ion conductivity of the sample decreases, meaning that the presence of BH_4^- anions in the structure promotes the Li-ion mobility. The **Figure 5.10** also shows that, the conductivity does not dependent on Br^-/Cl^- ratio. In fact, in the hexagonal structure, BH_4^- possess rapid reorientation,[31,117] so that the rotational freedom of the BH_4^- could have positive effects on the Li^+ conductivity (see also **Chapter 1**, paragraph 1.5.1)

The activation energy does not dependent on BH_4^-/Br^- ratio (**Figure 5.11**), but it increases with increasing the content of Cl^- in the hexagonal solid solution, reaching values higher than 0.6 eV (*e.g.* 0.63 eV for sample ***s10***). It is clear that the addition of Cl^- in the h-$Li(BH_4)_{1-x}(Br)_x(Cl)_y$ phase increases the activation energy for the Li-ion jump, without affecting significantly the Li-ion conductivity.

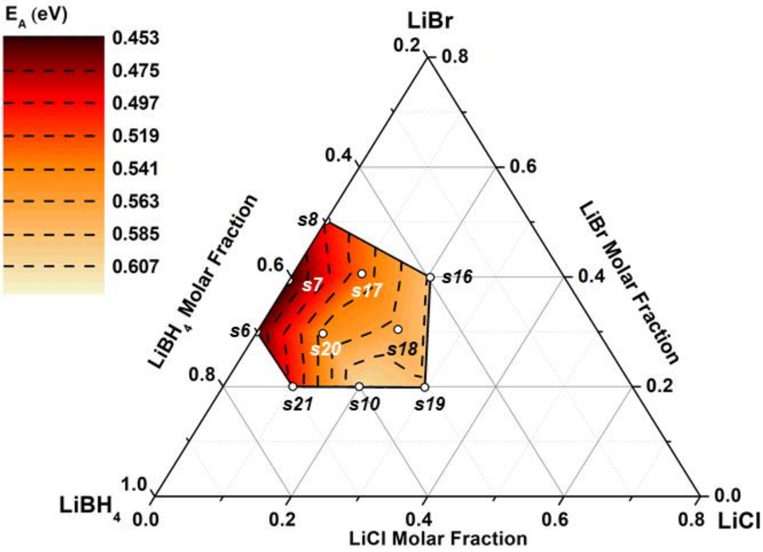

Figure 5.11. *Contour map of activation energy for Li-ion conductivity for samples in the hexagonal solid solution in the $LiBH_4$-LiBr-LiCl system as a function of composition. Iso-activation energy dashed lines correspond of the values and lines shown in the legend.*

As shown previously, the dissolution of Cl^- anion in the hexagonal structure decreases the cell volume, does not affect significantly the ionic conductivity, but increases the activation energy. Using conventional hopping theory,[118] the pre-exponential factor σ_0 can be defined as (see also Equation **1.6**):

$$\sigma_0 = \frac{cq^2d^2\nu}{2lk_B} e^{-\Delta S_m/k_B T} \qquad \textbf{(5.2)}$$

In the case of ionic conductors, the substitution with more polarizable anions in the sublattice causes a softening of the lattice.[115,116] This leads to a lower oscillation frequency of the moving cation, that decreases both the migration entropy and enthalpy (*i.e.* the activation energy).[115,116] This is clearly valid in $Li(BH_4)$-LiX systems (where X = Br and I) since the polarizability of BH_4^- results bigger than Cl^- (3.90 and 2.96 $Å^3$, respectively) but smaller than Br^- and I^- (4.16 and 6.43 $Å^3$, respectively).[119]

In order to elucidate the relation between anions polarizability and conduction mechanism in the hexagonal solid solution, the Mayer-Neldel plot (M-N) was built, plotting the natural logarithm of the pre-exponential factor, against the activation energy E_A (**Figure 5.12**).

The M-N rule is an empirical law that describes a group of physical properties that are Arrhenius-like dependent,[120] recently analysed to show the interplay between ionic conductivity and lattice rigidity in different compounds as argyrodites and LGPS thiophosphates.[21,115,121] According to Yelon et al.[122], in the M-N plot the stiffer the lattice, the flatter the slope.

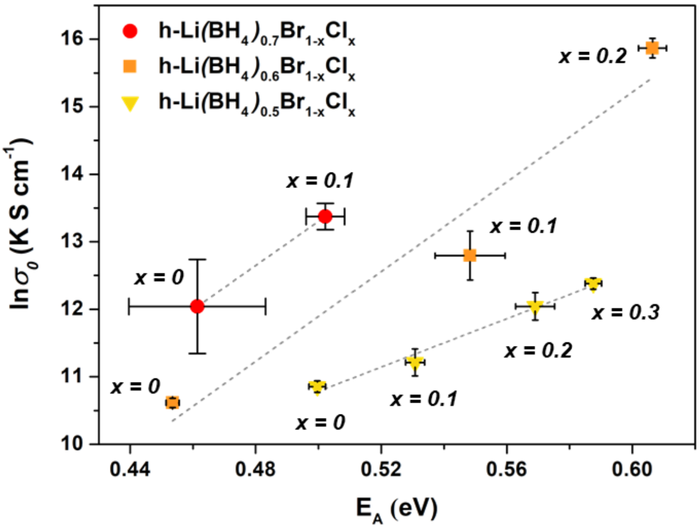

Figure 5.12. *Plot of the logarithm of the pre-exponential factor ($ln\sigma_0$) as a function of activation energy (E_A) for samples in the hexagonal solid solution for the $LiBH_4$-LiBr-LiCl system. Error bars have been obtained from the linear fit of Arrhenius plot. Dashed lines are a guide for the eyes.*

Hence, from **Figure 5.12**, three regions can be defined, corresponding to three different degrees of lattice stiffness, according to the amount of BH_4^- in the structure. When the borohydride is replaced by the halide, the lattice rigidity increases. According to **Figure5.12**, the edge between *soft* and *hard* hexagonal lattice can lie between $0.5 < BH_4^- < 0.6$ per formula unit. On the other hand, **Figure 5.11** and **Figure 5.12** clearly show that, once the BH_4^- content is fixed, the activation energy scales up with the amount of chloride in the structure. This phenomenon can be explained in terms of a stronger local electrostatic interaction, being Cl^- more electronegative than Br^-, and consequently locally “pinning” the mobile Li^+. Next to this, also the volume shrink experienced by the unit cell upon Cl substitution (**Figure 5.8**) shows the same trend as the activation energy. This is a logical consequence when the conduction pathway is left unchanged but in a smaller volume, the mobile lithium is indeed forced to make the same jump across a smaller bottleneck during its diffusion.

It is worth noting that, increasing the Cl^- content in the hexagonal solid solution, the density of the electrolyte decreases, as shown in **Figure 5.13a**. The density (ρ) of the samples was evaluated using the occupancy of the *2b* site of h-$LiBH_4$, the weight of the anion and the obtained cell volume. The density of the h-$Li(BH_4)_{0.7}(Br)_{0.2}(Cl)_{0.1}$ (sample ***s21***) and h-$Li(BH_4)_{0.7}(Br)_{0.3}$ (sample ***s6***) has been calculated equal to 1.19 and 1.32 g/cm^3, respectively, but the Li-ion conductivity is almost the same (**Figure 5.13b**). So, the addition of Cl^- in the hexagonal solid solution leads to lighter ion conductors with similar conductivity, suggesting possible applications of these fast ion conductors as electrolytes to increase the energy density in Li-ion solid-state batteries.

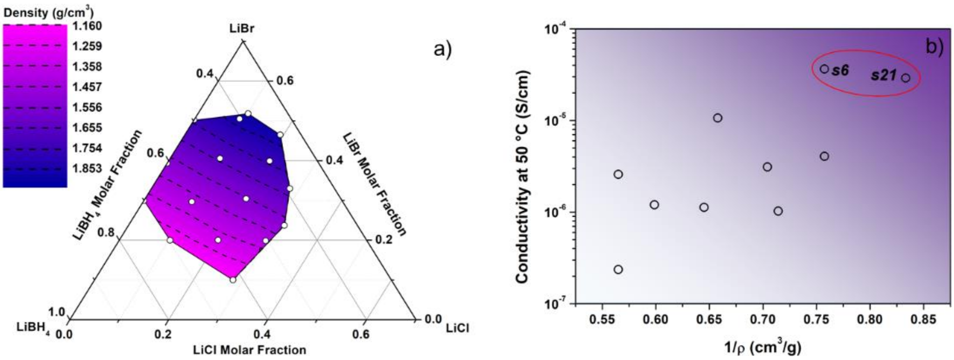

Figure 5.13. *a) Contour map of density of samples in the hexagonal solid solution in the $LiBH_4$-LiBr-LiCl system as a function of composition. Iso-density dashed lines correspond of the values and lines shown in the legend. b) plot of Li-ion conductivity at 50 °C with respect to the inverse of the density. The oval highlights the samples having a low density and, at the same time, a high conductivity.*

5.2.5. Cyclic voltammetry

To better understand the electrochemical stability upon halide substitution, with respect these of pure $LiBH_4$, different cross checks were performed on samples **s6** (corresponding to $Li(BH_4)_{0.7}Br_{0.3}$) and pure $LiBH_4$. The CVs were executed at 120 °C, in order to achieve the hexagonal conducting phase of $LiBH_4$. **Figure 5.14a** shows that the obtained CV for $LiBH_4$ has an electrochemical window of 2.1 V *vs.* Li^+/Li, which is narrower than that reported by Matsuo et al.[27] (5 V *vs.* Li^+/Li). This result could be surprising, but, recently, this values has been confirmed by Asakura et al.[78] In addition, Unemoto *et al.*[47] observed an electrochemical process at 2.1 V, but the authors referred to it as "side-reaction". **Figure 5.14a** indeed shows to which extent a decomposition process can be hidden by the plating process: the continuous and the dash-dot lines refer to two-layer pellet (with carbon) and simply bulk $LiBH_4$, respectively. The oxidation event, starting at 2.08 V is visible in both measurements, but amplified nearly hundred times by the larger accessible interface thanks to the carbon addition. The other peaks, occurring at low potential, refer to the insertion into graphite (< 0.9 V *vs.* Li^+/Li)[123]. It was not possible to identify the cathodic event at 2.2 V, which is however visible only in presence of carbon.

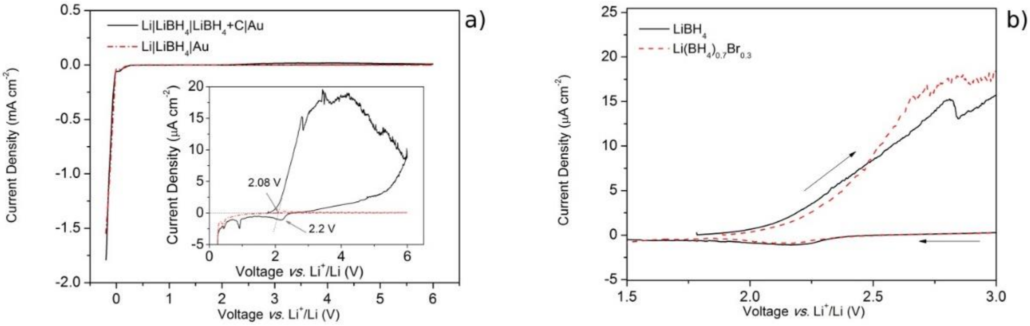

Figure 5.14. *Cyclic voltammetry measured at 120 °C. a) shows the amplification effect of carbon addition for the small oxidative event; b) compares* $LiBH_4$ *(continuous lines) and* $Li(BH_4)_{0.7}Br_{0.3}$ *(dashed lines) in the region 1.5-3.0 V vs.* Li^+/Li. *The onset of decomposition amounts to 2.26 and 2.08 V for* $Li(BH_4)_{0.7}Br_{0.3}$ *and* $LiBH_4$*, respectively.*

Figure 5.15 shows an overview of the electrochemical stability measured at 90 °C as a function of composition, within the monophasic hexagonal solid solution domain. The temperature was set to 90 °C for all compounds (were the conductivity of most of the samples lies above 10^{-5} S cm^{-1}) in order to guarantee a low cell resistance, ensuring the validity of the two-electrodes configuration. $Li(BH_4)_{0.7}Br_{0.3}$ measured at 90 °C revealed a drop of nearly 1.8 V in its electrochemical window and could be explained considering that the electrochemical window is a thermally activated process,[124] so it is straightforward to justify the depletion of the oxidative stability. The results shown in **Figure 5.15** clearly indicate that a deviation of composition from pure $Li(BH_4)_{0.7}Br_{0.3}$ involves a reduction of the electrochemical stability window.

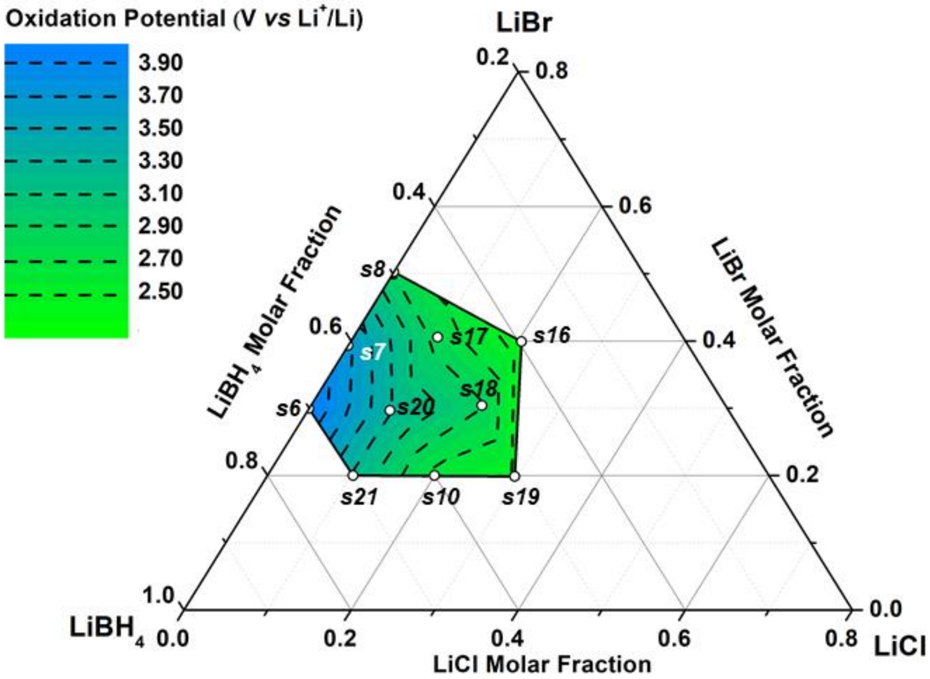

Figure 5.15. Contour map of oxidation potential of samples in the hexagonal solid solution in the $LiBH_4$-LiBr-LiCl system as a function of composition, obtained by cyclic voltammetry measured at 90 °C. Iso-potential dashed lines correspond of the values and lines shown in the legend.

Regarding the binary system $LiBH_4$-LiBr in the studied domain, the oxidative limit systematically lowers with the increasing content of Br^-, moving from a maximum of 4.04 down to 2.85 V for $0.3 < \alpha < 0.5$ ($\beta = 0$). When chloride is added to form a ternary solid solution, the fragility of the system increases, reducing the width of the electrochemical window down to 2.4 V (sample **s16** and **s19**). Nevertheless, a saddle point can be observed in the electrochemical stability map in the phase diagram, when the bromide content is fixed to $\alpha = 0.3$, suggesting an optimum in the composition, less prone to oxidation. It is interesting to note the similar trends in the volume variation as a function of the composition, activation energy for Li^+ mobility and electrochemical window. The dependence of the electrochemical stability from the composition can be discussed analysing the decomposition pathway of pure $LiBH_4$. As already pointed out by the work of Friedrichs *et al.*[125], $LiBH_4$ undergoes hydrogen desorption whilst producing LiH and B_2H_6, the latter further decomposing into B and H_2. Even though the authors stressed that the driving force of such reaction lies on the stability of B_2H_6, it is also worth considering the formation enthalpy ($\Delta_f H$) of LiH (-90.6 kJ/mol)[126]. In the case of the different solid solutions presented in this work, where Br^- and Cl^- partially replace BH_4^-, a similar decomposition pathway can be inferred. However, LiH would be flanked by the formation of LiBr and LiCl, which are more stable ($\Delta_f H$ of -350.9 kJ/mol and -408.7 kJ/mol, respectively)[126]. Consequently, the partial halide replacement affects the electrochemical window, which becomes narrower as the bromide, and more significantly chloride, substitution ratio increases. Nonetheless, a deeper understanding of this effect on the electrochemical stability is necessary and requires further theoretical insight.

5.3. Conclusions

In this chapter, the effect of the anion substitution, promoted by ball milling and thermal treatments, on the Li-ion conductivity in the $LiBH_4$-LiBr-LiCl system has been investigated. For the first time, a ternary hexagonal solid solution containing chloride in the $LiBH_4$ structure was stabilized at *RT* lowering the weight of the electrolyte, therefore increasing the energy density.

The $LiBH_4$-LiBr-LiCl ternary phase diagram has been defined at *RT*, combining PXD data, coupled with a Rietveld refinement and a mass balance. Values of the lattice parameters and volumes of the hexagonal solid solution have been determined as a function of composition. Because LiCl is immiscible in h-$LiBH_4$ at *RT*, it can be deduced that the presence of Br^- in the solid solution promotes the Cl^- solubilisation, confirming that the dimensions of the anion is a fundamental parameter to be considered. Solubility of up to 30 % of Cl^- in the solid solution has been established.

The effect of the composition of the h-$Li(BH_4)_{1-\alpha-\beta}(Br)_\alpha(Cl)_\beta$ solid solution on the Li-ion conductivity has been investigated as a function of temperature using EIS. The h-$Li(BH_4)_{0.7}(Br)_{0.2}(Cl)_{0.1}$ sample showed the highest value of ion conductivity in the ternary solid solution at 30 °C (1.3×10^{-5} S cm^{-1}). The chloride anion substitution in the hexagonal structure increases the activation energy but does not affect the Li-ion conductivity; this compensation effect is well described by the Meyer-Neldel rule. Even though such an effect can be explained in terms of lattice stiffening, it is still debated in the literature and either a theoretical model of the phonon spectra modification induced by anion mixing or a direct measure of the speed of sound could shed light on the Li dynamics in investigated complex hydrides.

The destabilization induced by this anion mixing also has a detrimental impact on the electrochemical stability. The effect of the halogenation on the electrochemical stability of the hexagonal solid solution shows that $Li(BH_4)_{0.7}Br_{0.3}$ offers the best electrochemical results, in terms of oxidative stability and Li^+ conductivity and indicates that a deviation of composition involves a reduction of the electrochemical stability window. On the other hand, the ternary phase

$Li(BH_4)_{0.7}Br_{0.2}Cl_{0.1}$, although paying a narrower electrochemical window, could offer a 10 % gain in weight, with no losses in ionic conductivity.

Chapter 6.

Enhancing Li-Ion Conductivity in $LiBH_4$-Based Solid Electrolytes by Adding Various Nanosized Oxides

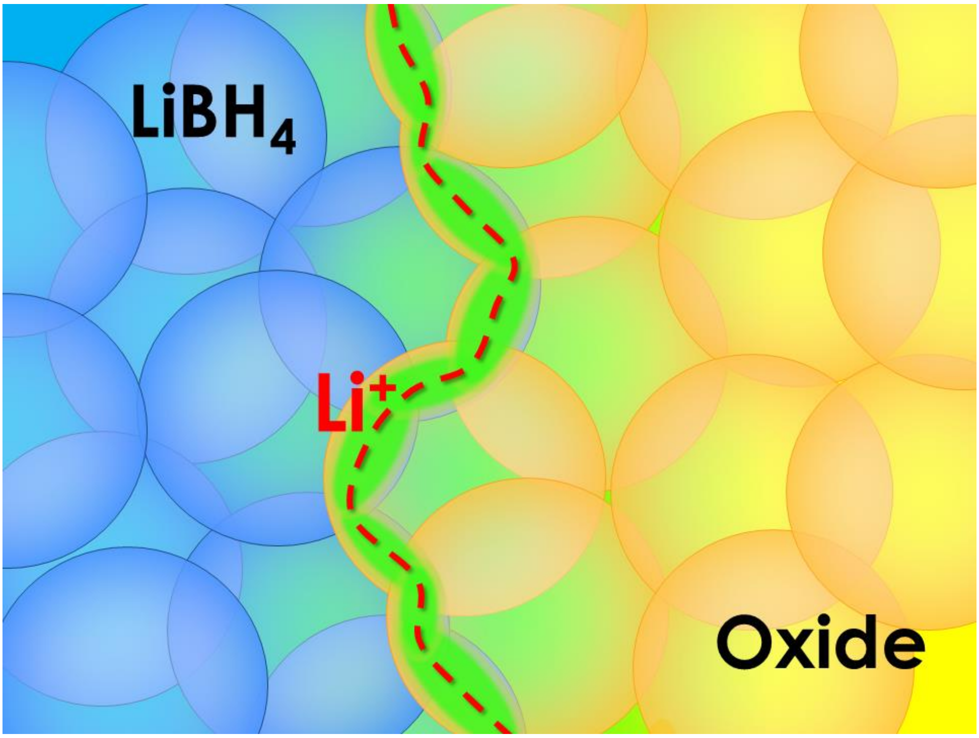

6.1. Introduction

A different approach to increase the ionic conductivity of the LT phase of $LiBH_4$ is by mixing it with oxides to form a composite, *e.g.* by nanoconfinement in suitable scaffolds.[42–44,127–129] Blanchard et al.[45] reported the effect of $LiBH_4$ confinement on Li-ion conductivity and mobility using an ordered mesoporous silica scaffold (MCM-41). In order to explain the increase of ionic conductivity of composites, a core-shell model was proposed, considering two different fractions of $LiBH_4$ present in the pores. The first fraction is positioned in the centre of the pores and, upon heating, similarly to bulk $LiBH_4$, it undergoes to the solid phase transition, but at lower temperatures.[45] The second fraction, which does not undergo a solid-solid phase transition, is located at the interface layer between $LiBH_4$ and SiO_2 and it is responsible for the high ionic conductivity. Suwarno et al.[129] quantified the thickness of the high mobility layer at the interface, which corresponds to 1.94 ± 0.13 nm for a silica nanoscaffold. Afterwards, Choi et al.[42,43] prepared $LiBH_4$-oxide nanocomposites by ball milling, showing as well an increased Li-ion conductivity.

As described above, creating interfaces with an oxide is a successful strategy to increase the Li-ion conductivity of $LiBH_4$ at RT, but it is not yet fully understood. So, the work presented in this chapter is aimed to synthetized novel solid-state fast ionic conductors based on $LiBH_4$-oxide systems. The synthesis of nanocomposites was obtained by ball milling, without any heat treatment afterwards. The effect on Li-ion conductivity of mixing $LiBH_4$ with different oxides has been investigated. For all samples prepared, the Li-ion conductivity was at least three orders of magnitude higher than that observed for the as-received Varying the ratio between SiO_2 and $LiBH_4$ and changing the oxide yielded new insights on how the enhanced conductivity correlates with structural properties of nanocomposites.

6.2. Results and discussion

6.2.1. Synthesis

$LiBH_4$ (purity >95% from Alfa Aesar) was mixed in different *v/v* % with oxides (see **Table 6.1**). SiO_2 (Aerosil 300, Evonik), CaO (Steam Chemicals), MgO (Steam Chemicals), Al_2O_3 (γ-phase, Alfa Aesar), TiO_2 (P90, Evonik) and ZrO_2 (RC 100, Gimex) were pelletized and dried at 300 °C in a furnace, under dynamic vacuum, for 6 hours.

	Oxide		**ρ**[130]	**BET Surface Area**	**V_p**	**Fraction of pore filled**[a]	**Thickness of $LiBH_4$**[b]
	wt. %	**v/v %**	**g/cm³**	**m²/g**	**cm³/g**	**%**	**nm**
SiO_2	30	11	2.20	294	2.30	152	11.9
SiO_2	45	20	2.20	294	2.30	80	6.2
SiO_2	55	27	2.20	294	2.30	53	4.2
SiO_2	63	34	2.20	294	2.30	38	3.0
SiO_2	70	41	2.20	294	2.30	28	2.2
SiO_2	78	52	2.20	294	2.30	18	1.4
ZrO_2	75	25	5.89	94	0.26	193	5.3
TiO_2	68	25	4.10	94	0.48	147	7.5
Al_2O_3	67	25	3.96	67	0.30	247	11.0
MgO	65	25	3.58	215	0.25	323	3.8
CaO	62	25	3.30	20	0.13	708	46.0

Table 6.1. *Composition of investigated mixtures.*
a) Calculation performed dividing the $LiBH_4$ occupied volume per gram of SiO_2 by the pore volume (V_p).
b) Calculation performed considering the BET surface area of the oxides and assuming it a flat geometry.

Before mixing, as-received $LiBH_4$ was ball-milled for 2 hours at 500 r.p.m. and was used as starting material for the $LiBH_4$-oxide mixtures. All samples prepared were milled for three periods of 10 min at 300 r.p.m. 2 min breaks has been used between each period in order to overcome heating effects. Samples with different oxides were prepared with the same volume fraction (~25 *v/v* % of oxide) (see **Table 6.1**). Surface area (S_{BET}) and total pore volumes (V_p) of different oxides (see **Table 6.1**) were obtained by N_2 adsorption at 77 K in a TriStar Plus II gas-volumetric apparatus (Micromeritics, Norcross, GA, USA). The specific surface area of different oxides was derived by fitting with a Brunauer–Emmett–Teller isotherm,[131] whereas the total pore volume was obtained from the absorbed volume of the nitrogen at $p/p_0 = 0.95$.

6.2.2. Effect of ball milling on the Li-ion conductivity of $LiBH_4$

Figure 6.1 shows the Arrhenius plot of the ionic conductivity of as-received and ball-milled $LiBH_4$, measured by EIS.

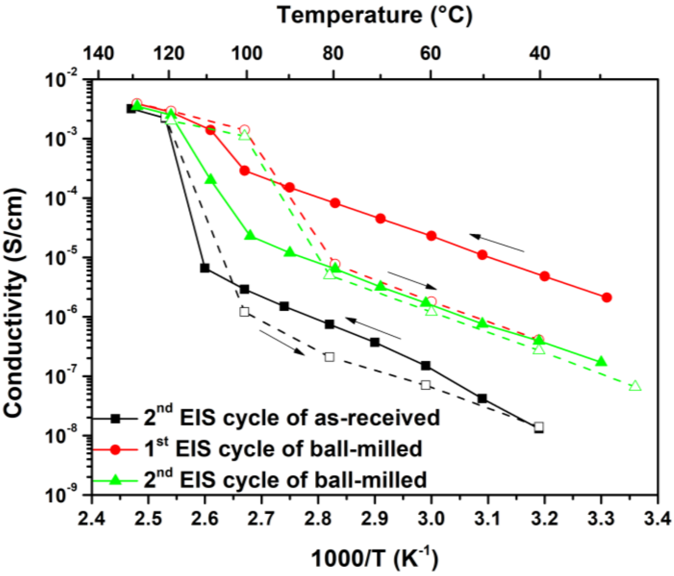

Figure 6.1. *Li-ion conductivity of the second temperature-dependent EIS cycle of as-received* $LiBH_4$ *(black squares), the first and the second temperature-dependent EIS cycle of ball-milled* $LiBH_4$ *(red circles and green triangles, respectively). Closed symbols and solid lines correspond to the heating ramp, while open symbols and dashed lines represent the cooling one.*

Two cycles are reported for the ball-milled sample, in order to clarify the effect of the temperature cycling on the Li-ion conductivity. For the as-received $LiBH_4$, only the second cycle is reported. The impedance spectrum is composed by a single arc in the Nyquist plot. The bulk property was modelled with a constant phase element (CPE_{Bulk}) in parallel with a resistor, representing the Li^+ diffusion.

Below 120 °C, ball-milled $LiBH_4$ shows a much higher ionic conductivity, *i.e.* 4.8×10^{-6} S cm^{-1} at 40 °C for the first cycle and 3.9×10^{-7} S cm^{-1} for the second cycle, than the as-received sample, 1.3×10^{-8} S cm^{-1}. Li-ion conductivity of the ball-milled sample during the first cycle is about three orders of magnitude higher than that of the as-received $LiBH_4$. However, the ionic conductivity is much lower during the subsequent cooling ramp. The Li-ion conductivity measured during the second cycle is similar to that measured during the cooling ramp of the first cycle.

The high conductivity detected directly after ball milling is probably due to structural modifications, most notably because of an increase of defects due to the mechanochemical treatment. The PXD pattern of ball-milled $LiBH_4$ (**Figure 6.2**) shows marginally broader diffraction peaks than those of as-received $LiBH_4$. This can be ascribed to a reduction of crystallites size and/or introduction of strain in the crystal lattice.

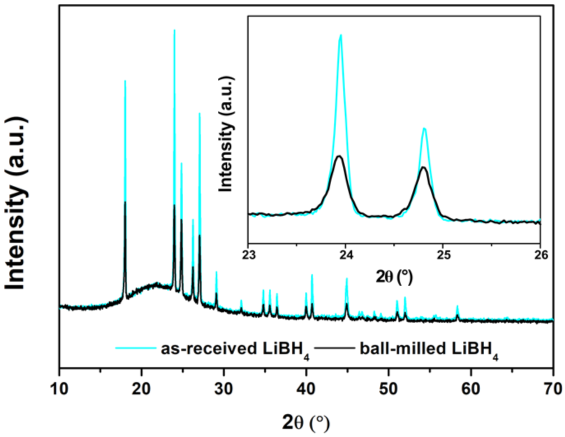

Figure 6.2. *PXD patterns of the as-received $LiBH_4$ and ball-milled (BM) $LiBH_4$. The inset shows a magnification in the 23-26° 2θ range.*

The activation energy was obtained by a linear fit of the data shown in **Figure 6.1**, considering the data of the heating ramps below the transition temperature. Values equal to 0.70 eV, 0.75 eV and 0.91 eV were determined for the first cycle, the second cycle and the second cycle of as-received $LiBH_4$, respectively. The activation energy for the ball-milled $LiBH_4$ is smaller than that obtained for the as-received one, but it increases upon heat thermal cycling.

An increase of the Li-ion conductivity of $LiBH_4$ due the mechanochemical treatment was already reported in the literature (see **Chapter 3**).[37,82] Ball milling increases the defect concentration, leading to an increase of the number of Li interstitials and Li vacancies, that are relevant for Li ion mobility.[83] Recently, S. Breuer et al.[132], using ^{7}Li longitudinal nuclear magnetic relaxation, could detect two different mobility mechanisms of Li-ions in nanocrystalline orthorhombic $LiBH_4$. The surface pathways through defective regions offers activation barriers much lower than that in the crystalline bulk regions.[133] However, the ionic conductivity decreases of one order of magnitude after heating up to the phase transition temperature, presumably because of the annihilation of some defects caused by the mechanochemical treatment, that facilitated the Li-ion mobility. This means that, although ball-milling can induce an increase of conductivity, it depends on non-stable defects, that disappear mostly upon heat treatment. It would therefore be very interesting to find a way to stabilize the enhanced Li-ion conductivity. For this reason, the effect of the composition on Li-ion conductivity in the $LiBH_4$-SiO_2 mixed system was analysed.

6.2.3. $LiBH_4$–SiO_2 composites: influence of the composition

The exact mechanism leading to the increase in Li-ion conduction is not fully understood yet. However, it has been suggested that the nanostructure created at the interface by the interaction of $LiBH_4$ with the oxide generates a fraction of material characterized by preferential pathways for ion conduction.[43,129,134] NEXAFS spectroscopy was employed to explore possible interface changes after ball milling, by analysing the chemical bonding of the constituent elements.[43] A new chemical bond between B and O was identified from NEXAFS spectra, meaning that some oxidation takes place at the interface. The number of B-O bonds could not be linked to the increase of conductivity, but it is clear that Al_2O_3 and SiO_2 are not completely inert during ball milling with $LiBH_4$.[43,135]

In the past decades, several composite ionic conductors have been synthetized by mixing Li-based compounds with an insulator phase, *e.g.* Li_2O ion conductivity has been enhanced by mixing with Al_2O_3 and B_2O_3.[136–138] Frequency and temperature dependent Li^7 solid state NMR spectroscopy measurements performed on different two-phase composites, demonstrated heterogeneous dynamics, reflecting the presence of slow and fast diffusing Li ions, according with the space-charge layer effect,[139,140] which corresponds to carrier redistribution at space charge regions near a two-phases interface. The presence of an insulator could create a defective and highly conducting layer along the interface between the conducting and the insulating phases.[141] However, high mobilities and two different phases were also detected when mixing with conductive carbon powder.[15]

The effect of the composition on Li-ion conductivity in $LiBH_4$-SiO_2 has been evaluated for a composition range (from 11 to 52 *v/v* % of silica) corresponding to a pore filling fraction from 18 to 152 % (see **Table 6.1**). After the synthesis, a PXD analysis was performed at R*T* for each sample, confirming that no new compounds had been formed (**Figure 6.3**). Patterns show the presence of the main diffraction peak of the $LiBH_4$ orthorhombic phase, while Aerosil SiO_2 is X-ray amorphous. No clear indication about the formation of the interface layer could be obtained form this type of analysis. Increasing the amount of SiO2 in the composite the intensity of the Bragg peaks of the orthodromic phase decreases. In any case, PXD analysis confirms that the $LiBH_4$ is still present in the orthorhombic phase after the mechanochemical treatment with oxides.

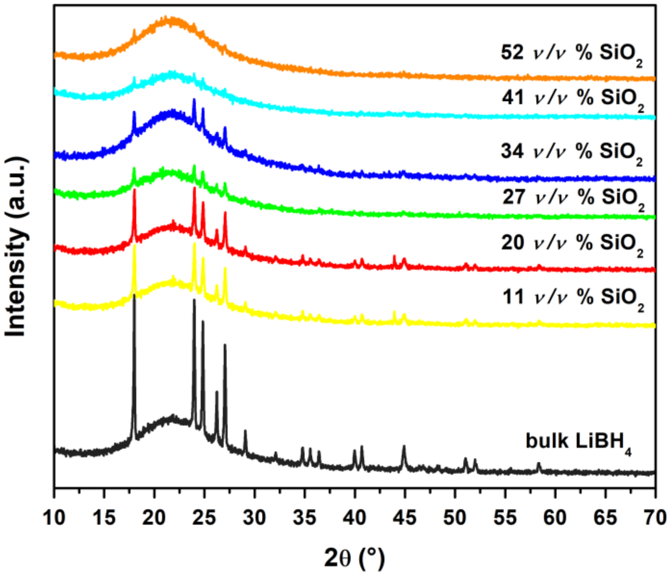

Figure 6.3. *PXD patterns of ball-milled samples for different v/v% ratios and of as-received* $LiBH_4$.

The Arrhenius plots for the conductivity of ball-milled samples with different *v/v* % of SiO_2 are shown in **Figure 6.4a**. Li-ion conductivity values obtained at 30 °C are presented in the **Table 6.2** (see the end of this chapter). In the low temperature range, below 110 °C, the conductivity values for all composite samples are higher than those obtained for the orthorhombic as-received $LiBH_4$. Among all samples, that with 20 *v/v* % of SiO_2 shows the highest ionic conductivity in the whole temperature range before the phase transition. Observed values of Li-ion conductivity are close to those reported by Choi et al.[42] (1.5 $\times 10^{-5}$ S cm^{-1} at 40 °C for 55 *v/v* % of fumed silica), and by Blanchard et al.[45] (1.0 $\times 10^{-5}$ S cm^{-1} at 40 °C for 28 *v/v* % of MCM-41). In **Figure 6.4**, the sudden change of Li-ion conductivity due to the LT-to-HT phase transition is not always observed.

Data for 41 and 52 *v/v* % of SiO_2 mixtures do not show the jump due to the formation of the HT phase, suggesting that the conductive contribution by the bulk $LiBH_4$ in the samples is negligible. On the other hand, around the phase transition temperature, 27 and 34 *v/v* % of SiO_2 samples exhibit a slight change in conductivity and samples containing 11 and 20 *v/v* % of SiO_2 mixtures show an evident jump of the Li-ion conductivity at about 110 °C. In 11 and 20 *v/v* % of SiO_2 samples, above the phase transition, the Li-ion conductivity is higher with respect to the one measured for the hexagonal phase of the as-received $LiBH_4$, meaning that a synergic effect is still observed.

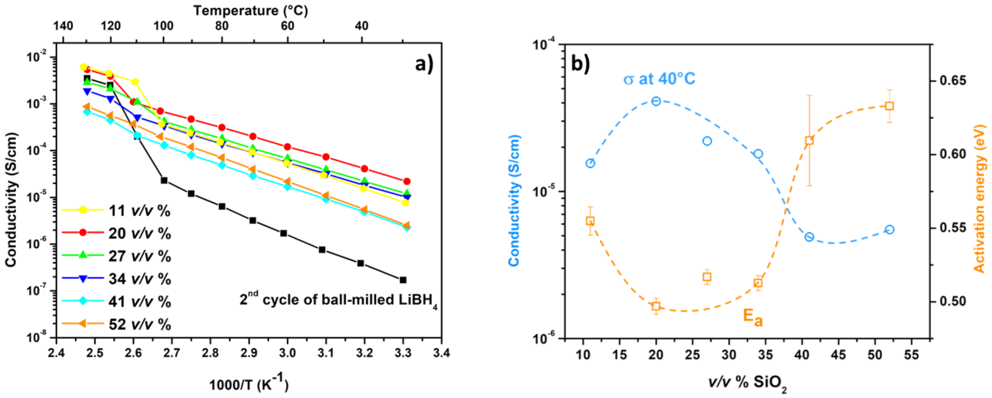

Figure 6.4. *a) Li-ion conductivity of samples containing different v/v % of* SiO_2*. All data were obtained from the second heating temperature-dependent EIS cycle. Li-ion conductivity of the ball-milled* $LiBH_4$ *during the second heating temperature-dependent EIS cycle is shown for comparison. b) Li-ion conductivity at 40 °C and activation energy as a function of the v/v % of* SiO_2*. The activation energy was calculated from data collected during the second heating ramp. Error bars were obtained from the linear fit of Arrhenius plot (95% of confidence). Dashed lines are a guide for the eye.*

Suwarno et al.[129] demonstrated, by pore-size-dependent transition enthalpy measurements, that a fraction of the $LiBH_4$, that is in direct contact with the SiO_2, does not undergo a structural phase transition. The thickness of this interface layer was estimated as 1.94 ± 0.13 nm.[129] The enhancement of Li-ion conductivity due to the phase transition in samples containing silica could be explained considering the estimated values for the thickness of the $LiBH_4$ layer on SiO_2 (see Table 1). The calculation was performed taking into account the surface area of the SiO_2 and assuming that its surface is fully and uniformly covered by $LiBH_4$. Indeed, for samples with 41 and 52 *v/v* % of SiO_2, that do not show the jump of the Li-ion conductivity associated to the phase transition, the calculated thickness of $LiBH_4$ (2.2 and 1.4 nm, respectively), is close to the value estimated by Suwarno et al.[129]. Considering other samples, the calculated thickness is higher than that estimated for the high conductive interface layer, confirming the contribution to Li-ion conductivity from crystalline $LiBH_4$. Data reported by Choi et al.[42] are in agreement with this behaviour, *i.e.* the samples with a calculated $LiBH_4$ thickness lower that about 2 nm do not show an increased Li-ion conductivity after the phase transition.

Figure 6.4b shows the Li-ion conductivity at 40 °C as a function of the amount of silica. A maximum is reached for the sample with 20 *v/v* % of SiO_2 (4.1×10^{-5} S cm^{-1}), with samples containing 27 and 34 *v/v* % of SiO_2 showing conductivity values close to this maximum. A clear decrease of Li-ion conductivity is observed for higher loadings (41 and 52 *v/v* % of SiO_2). In **Figure 6.4b**, the dependence of the activation energy as a function of the amount of silica is also included. The lowest value of activation energy is observed for the sample containing 20 *v/v* % of SiO_2 (*i.e.* 0.49 eV), that, compared to the value of 0.91 eV obtained for pure $LiBH_4$, may be linked to the increased conductivity due to the formation of the composite. An increase of the amount of silica in the mixture led to higher values for the activation energy, as well as for the sample containing 11 *v/v* % of SiO_2. Obtained activation energy values are close to those reported in the literature for similar composite conductors.[42,45]

The relation between conductivity and the fraction of pores filled has been analysed. **Figure 6.5** reports the conductivity at 40 °C for $LiBH_4$-SiO_2 composites as a function of pore filling. Pore filling is here defined as the ratio between the volume of the pores in the oxides powder before addition of the $LiBH_4$ and the volume of the $LiBH_4$ added. As the oxides consist of nanocrystallites, it is not expected that ball milling will greatly modify the effective mesopore volume, which is formed by the interparticle space between the crystallites. SiO_2 itself is an insulator, so without $LiBH_4$ (0% pore filling) the conductivity is negligible. Upon increasing the fraction of interparticle volume filled, the conductivity rapidly increased, most likely because gradually a connected pathway for Li-ion (conducting regions) is formed. The highest Li-ion conductivity was found for the sample closest to a complete pore filling. The conductivity increases with the increasing of pore volume filling and decreases after exceeding the complete pore filling. For the first time, we report a clearly structural parameter, that maximizes the Li-ion conductivity.

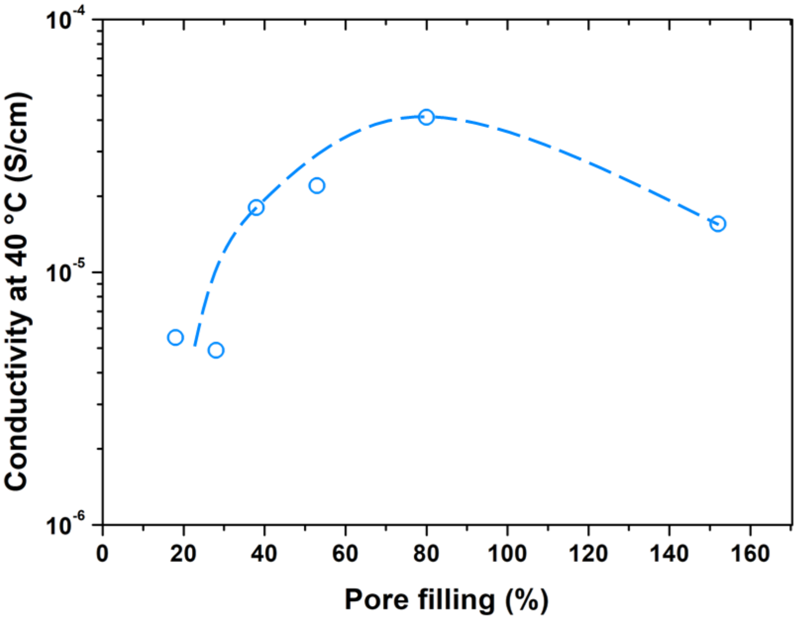

Figure 6.5. *Li-ion conductivity at 40 °C as a function of pore filling (%).*

The occurrence of an optimal volume fraction of insulating material and pore filling which maximizes the conductivity, as shown in **Figure 6.4** and **Figure 6.5**, can be explained considering two forms of $LiBH_4$ (the "core-shell model"),[45] in which highly conductive $LiBH_4$ (the "shell") is within a short distance from the interface with the oxide, while bulk $LiBH_4$, which is further away from the interface ("the "core"), has a much lower conductivity at room temperature. In the sample with 11 *v/v* % of SiO_2, an excess of crystalline $LiBH_4$ is present (pore filling "150 %") therefore the conduction pathway of the highly conductive phase is interrupted by the lower conductivity crystalline $LiBH_4$ regions. On the contrary, in samples containing SiO_2 > 20 *v/v* %, where the pore filling is below 100 %, it is the insulating oxide, or void regions that interrupt the Li-ion pathway. A tailoring of the pore filling allows to optimize the volume ratio between high conductive interface layer and bulk $LiBH_4$. Consequently, a deviation from a complete filling of pores in the composite (thus for both too low and high-volume fractions of insulating materials) cannot provide a well-connected interface layer network. This is the first time that the optimum ratio of ion conductor and oxidic additive has been clearly related to an easily measurable structural parameter, the pore volume of the oxide additive powder. We look forward to its validity being scrutinized by future results (for instance Choi et al.[42] reported a maximum value of Li-ion conductivity for a $LiBH_4$-SiO_2 composite with 55 *v/v* % of fumed silica, but did not mention the pore volume of the oxide powder).

6.2.4. Effect of the heat treatment

The ionic conductivity for each sample was measured during four subsequent heating/cooling cycles. For the whole composition range, the conductivity increased after the first heating ramp, but from the second cycle the Li-ion conductivity remained basically constant. As an example, the Arrhenius plot obtained for the sample with 41 *v/v* % of silica is shown in **Figure 6.6a**, where an increase by one order of magnitude after the first heating step was observed. The ratio between conductivities measured at 40 °C in the first and the second heating ramp increased as a function of the added amount of SiO_2, as reported in **Figure 6.6b**. The increase of the ionic conductivity after the first heating ramp in nanocomposites with a high amount of silica is the opposite of that observed for the pure ball-milled $LiBH_4$ (compare with **Figure 6.1**). In fact, this behaviour was observed for all mixtures, except for the sample containing 11 *v/v* % of SiO_2, where the conductivity decreased after the first cycle (**Figure 6.6b**).

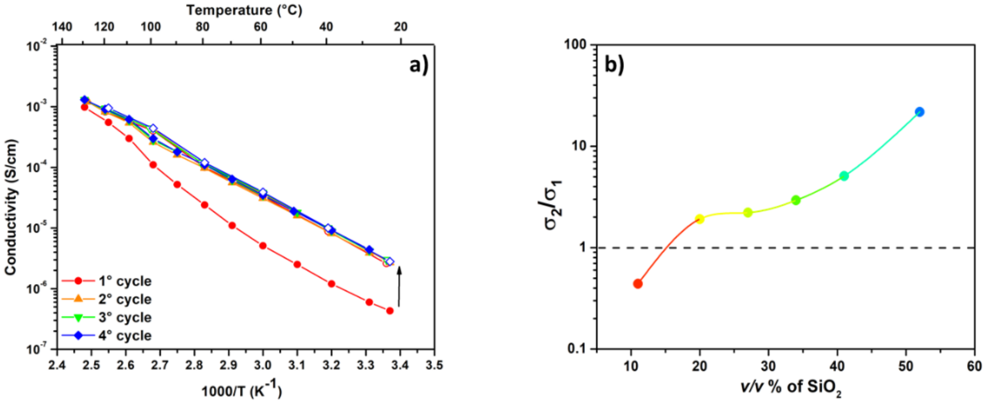

Figure 6.6. *a) Arrhenius plot of the BM samples with 41 v/v % of* SiO_2 *cycled from 30 °C to 130 °C four times. Closed symbols represent the heating ramp, open symbols the cooling one. b) Ratio between the conductivity measured at 40 °C for the second and first heating ramp as a function of the v/v % of* SiO_2.

The observed behaviour can be explained considering the first heating cycle as a heat treatment. Following this heat treatment, defects deriving from the mechanochemical treatment are annihilated in the bulk $LiBH_4$. The behaviour observed for the sample with only 11 *v/v* % of silica, resembles that observed for ball-milled $LiBH_4$, indicating that for this sample the observed conductivity is dominated by the macrocrystalline $LiBH_4$. On the other contrary, the formation of the highly conductive interface region at the $LiBH_4$/oxide interface seems to be promoted and stabilized by heat treatment, giving the highly conductive nanocomposites an excellent resistance against temperature fluctuations.

6.2.5. Effect of different oxides on the Li-ion mobility in $LiBH_4$

In literature, a high ionic conductivity has been reported for $LiBH_4$ nanocomposites obtained not only with silica, but also with alumina.[43] Here a systematic study of the influence of different types of oxides, both insulators, such as CaO, MgO, ZrO_2, as well as semiconductors, such as TiO_2, is presented. Before milling, the same pre-treatment conditions were applied for all oxides, as it is known from $LiBH_4/SiO_2$ nanocomposites that pre-treatment of the oxide can influence the conductivity of the nanocomposite.[142]. In all cases 25 v/v % of oxide in the mixture was added (see **Table 6.1**). The resulting Li-ion conductivities, derived from EIS during the second heating ramp for composites containing different oxides, are shown as an Arrhenius plot in **Figure 6.7**. Values obtained at 30 °C are presented in the **Table 6.2**.

All samples show a Li-ion conductivity higher than that of as-received $LiBH_4$. $LiBH_4$-CaO mixture shows the lowest ionic conductivity in the whole temperature range, with a value equal to 1.6×10^{-6} S cm^{-1} at 40 °C. However this might also be cause by the fact that, due to the low pore volume of CaO, in this case about seven times more $LiBH_4$ is added than corresponding to the pore volume. Very interestingly, the ionic conductivity reaches 2.6×10^{-4} S cm^{-1} and 1.8×10^{-4} S cm^{-1} at 40 °C for samples containing ZrO_2 and MgO, respectively. These values are more than four orders of magnitude higher than that obtained for the as-received $LiBH_4$, and also clearly higher than those observed for nanocomposites with SiO_2 and Al_2O_3. The lowest activation energies, 0.44 and 0.46 eV, were observed for samples containing ZrO_2 and MgO respectively, while samples containing CaO, SiO_2 and Al_2O_3 show an activation energy equal to 0.86, 0.52 and 0.55 eV, respectively.

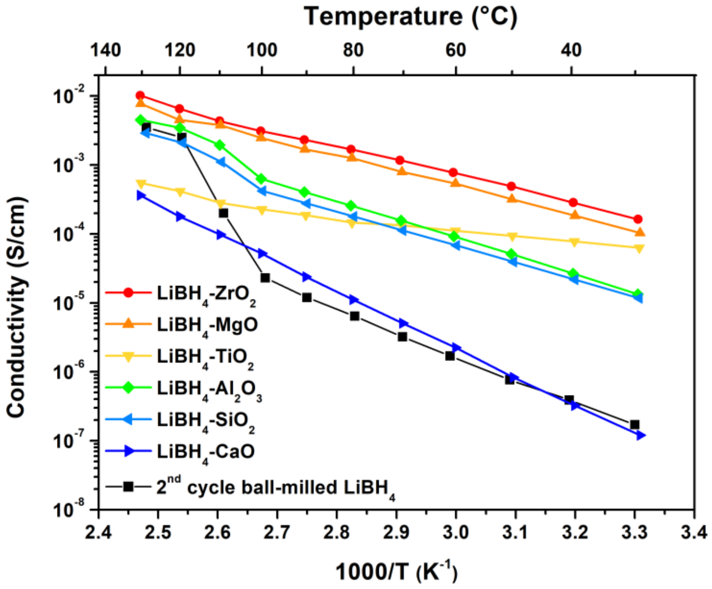

Figure 6.7. *Li-ion conductivity of ball-milled mixtures of $LiBH_4$ with 25 v/v % of different oxides. All data shown were obtained during the second heating temperature-dependent EIS cycle. Li-ion conductivity of the ball-milled $LiBH_4$ and the sample containing 27 v/v % of SiO_2, during the second heating temperature-dependent EIS cycle, are shown for comparison.*

The mixture of $LiBH_4$ with TiO_2 shows a strikingly low activation energy (0.24 eV). The colour of the nanocomposite was blue. TiO_2 is the only oxide in the series that is not an insulator but a semiconductor, and it is known that the blue colour is caused by the presence of Ti^{3+} and oxygen defects.[143] Since $LiBH_4$ is a strong reducing agent, it is likely that some TiO_2 has been reduced by the $LiBH_4$ forming TiO_{2-x}. In the partially reduced form, titanium dioxide has an appreciable electronic n-type conductivity.[144] The conductivity as measured by electrochemical impedance is the sum of ionic conductivity and electronic conductivity. To separate the two components, the electronic conductivity of the samples containing ZrO_2, MgO and TiO_2 has been evaluated by DC voltage polarization,[50,74] and the results are reported in **Figure 6.8**.

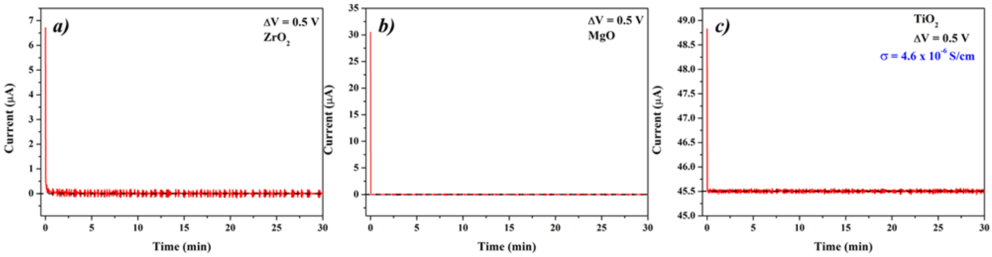

Figure 6.8. *The current as a function of time for samples containing a) ZrO_2, b) MgO and c) TiO_2 using stainless steel blocking electrodes. The plots show the non-filtrated instrumental noise (red line) and the mean value (black line)*

The initial current consists on the sum of the ionic and electronic currents, while the final current corresponds to only the electronic one. In **Figure 6.8a** and **Figure 6.8b**, referring to samples containing ZrO_2 and MgO, respectively, the current decreases rapidly to zero. This type of behavior indicates that the current through the electrolyte is ionic, because there is no remaining current after the initial charging of the system. This is an interesting result, considering the high conductivity observed for these samples and, at the same time, a negligible electronic conductivity. On the contrary, **Figure 6.8c** shows that the sample containing TiO_2 shows an electronic conductivity equal to 4.6×10^{-6} S cm^{-1}, which explains the low activation energy detected for the overall conductivity.

The observed value of the electronic current for this sample demonstrates that the TiO_2 has been partially reduced by $LiBH_4$ during the mechanochemical treatment, making this sample unusable as solid-state-electrolyte. Das et al.[50] already reported a negligible conductivity for the system $LiBH_4$-SiO_2. The electronic conductivity of $LiBH_4$ could be considered negligible, both in base of the results reported in **Figure 6.8**, since in samples pure $LiBH_4$ is still present, and the results about working all-solid-state Li-ion batteries using $LiBH_4$ as solid-state electrolyte.[46] The electronic conductivity for Al_2O_3 and CaO has been already demonstrated to be negligible in literature,[145,146] therefore it is possible to assume that also the electronic conductivity of the samples prepared in this work is negligible. This shows how important it is, in reporting ionic conductivities, to verify whether all conductivity measured by EIS is due to ionic conductivity, and to exclude the possibility of significant electronic conductivity.

Finally, **Table 6.2** reports Li-ion conductivity at 30 °C and activation energy of all the sample synthetized, in order to have a complete overview of the sample analyzed in this chapter.

Hydride	Oxide			σ at 30 °C$^{\#}$	$E_A$$^{\#}$
		wt. %	v/v %	S cm^{-1}	eV
$LiBH_4$ Ball-milled 2nd cycle	/	/	/	1.70×10^{-7}	0.75 ± 0.04
$LiBH_4$	SiO_2	30	11	7.66×10^{-6}	0.555 ± 0.009
$LiBH_4$	SiO_2	45	20	2.24×10^{-5}	0.494 ± 0.005
$LiBH_4$	SiO_2	55	27	1.17×10^{-5}	0.517 ± 0.005
$LiBH_4$	SiO_2	63	34	1.00×10^{-5}	0.513 ± 0.005
$LiBH_4$	SiO_2	70	41	2.29×10^{-6}	0.61 ± 0.03
$LiBH_4$	SiO_2	78	52	2.50×10^{-6}	0.63 ± 0.01
$LiBH_4$	ZrO_2	75	25	1.63×10^{-4}	0.44 ± 0.02
$LiBH_4$	TiO_2	68	25	6.30×10^{-5}	0.24 ± 0.03
$LiBH_4$	Al_2O_3	67	25	1.34×10^{-5}	0.55 ± 0.02
$LiBH_4$	MgO	65	25	1.03×10^{-4}	0.460 ± 0.008
$LiBH_4$	CaO	62	25	1.20×10^{-7}	0.86 ± 0.02

#) Activation energy and Li-ion conductivity related for the second temperature-dependent EIS cycle

Table 6.2: *Li-ion conductivity at 30 °C and activation energy of all the sample synthetized.*

For mixtures with silica, the optimum composition was previously observed to be close to 100 % pore filling. Since the pore volume (V_p) of other oxides (**see Table 6.1**) is much smaller than that of SiO_2, for all samples the fraction of pore filling is much higher than 100 %. Therefore, it is likely that even much higher conductivities can be obtained in these $LiBH_4$-oxide systems when using an optimum ratio between $LiBH_4$ and oxide. For practical applications, the electrochemical stability window is very important. For pure $LiBH_4$ it is report to be around 2 V *vs.* Li^+/Li (see also **Chapter 5**)[77,78]. All-solid-state Li-ion batteries have been prepared using a $LiBH_4$-nanoporous SiO_2 nanocomposite as solid state electrolyte, showing the potential of this type of electrolytes for application in full-cell batteries.[44,46,50]

6.3. Conclusions

The effect of adding various nanosized oxides by ball milling on the solid-state ion conductivity of $LiBH_4$ has been reported. First the effect of heat cycling up to 130 °C was investigated. While for the pure ball-milled $LiBH_4$ the conductivity gradually decreased upon temperature cycling, for the oxide-containing nanocomposites the conductivity actually increased upon the first temperature cycle, and remained remarkably stable upon further cycling. The presence of oxide nanoparticles in the nanocomposite for all oxides investigated greatly enhanced the ionic conductivity, typically with about three orders of magnitude at 40 °C. $LiBH_4$-SiO_2 nanocomposites had been reported before, but we investigated in detail the effect of structural properties and composition on the conductivity. This led to a few guidelines to reach maximum conductivity in these nanocomposites:

- The volume of $LiBH_4$ in the nanocomposite should correspond roughly to the pore volume of the oxide powder before ball milling;
- A heat cycle to 130 °C (slightly above the solid-solid phase transition temperature) is effective to reach maximum conductivity, which is stable upon repeated temperature cycling;
- Although the highest conductivity is found within 2 nm of the $LiBH_4$/oxide interface, nanocomposites with an average $LiBH_4$ thickness of 5-8 nm on the

oxide (as calculated using the oxide BET surface area) give the highest conductivities, which are not limited by low-conductivity macrocrystalline $LiBH_4$ regions. If possible, the porosity of the oxide should be adjusted to optimize this factor;

- The nature of the oxide is important. Nanocomposites with SiO_2 and Al_2O_3 had been reported before, but the highest conductivities (2.6×10^{-4} and 1.8×10^{-4} S cm^{-1} at 40 °C) were observed for nanocomposites with ZrO_2 and MgO respectively, while these conductivities can be further increased by optimizing the composition and morphology. Care has to be taken with reducible oxides like TiO_2, as high conductivities can be partially ascribed to electronic conductitvity, due to partial reduction of the oxide by $LiBH_4$.

These general insights into optimal structural parameters are probably relevant for any $LiBH_4$-oxide system, although of course it remains important to test also practically test the different compositions in full solid-state Li-ion batteries.

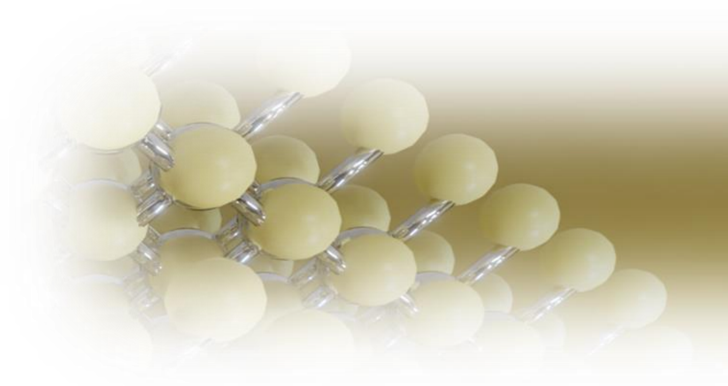

Chapter 7.

Synergic effect between halogenation and oxide addition on the Li-ion conductivity of the $LiBH_4$

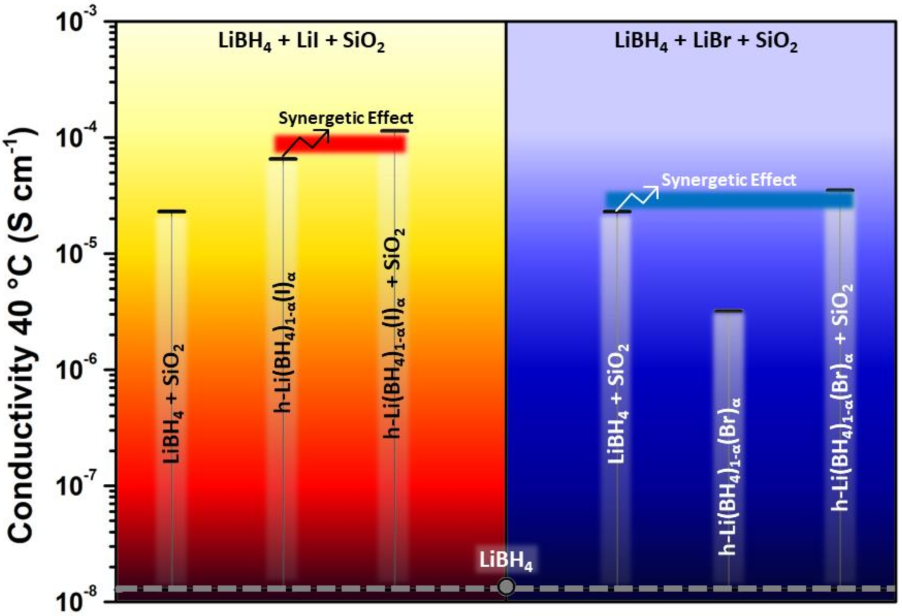

7.1. Introduction

The possibility of a synergic effect between the two different approaches presented in **Chapter 5** and **Chapter 6**, has been investigated by synthetizing the h-$Li(BH_4)_{1-\alpha}(X)_\alpha$ (X = I^- and Br^-) solid solutions and, afterwards, by mixing them with silica. Different compositions in the $LiBH_4$-LiX (X = I^- and Br^-) systems have been synthetized and have been selected considering the solubility limits of the solid solutions reported in literature and in **Chapter 4**. The effect of the halogenation on the Li-ion conductivity has been analysed. Once the most conductive solid solutions h-$Li(BH_4)_{1-\alpha}(X)_\alpha$, have been evidenced, is was mixed, in different ratios, with SiO_2. In addition, also the other h-$Li(BH_4)_{1-\alpha}(X)_\alpha$ solid solutions were mixed with a different quantity of SiO_2, but with a lower *v/v* % of SiO2.

7.2. Results and discussion

7.2.1. Synthesis

$LiBH_4$ (purity >95% from Sigma-Aldrich), LiBr (purity >99% from Sigma-Aldrich) and LiI (purity >99% from Sigma-Aldrich) were mixed in different ratios, as reported in **Table 7.1**. Before mixing, LiBr were dried at 120 °C in a furnace under dynamic vacuum. $LiBH_4$-LiX mixtures were ball milled for 1.5 hours at 350 r.p.m., in steps of 10 min separated by 2 min breaks, following the preparation reported by Gulino et al.[84], *i.e.* **Chapter 5**. In order to reach the equilibrium conditions, all samples were annealed (AN) at 250 °C for 2 h in a quartz tube under static vacuum, with a heating/cooling rate of 5 °C/min.

Name	**Halide**		**Oxide**		$\rho^{a)}$	**Fraction of pore filled**$^{b)}$	**Thickness of h-Li**$(BH_4)_{1-\alpha}(X)_\alpha$ $^{c)}$
	Molar Fraction		***wt. %***	***v/v %***	***g/cm***^{3}	***%***	***nm***
I0.2	I	0.2	/	/	1.30	/	/
I0.2-13	I	0.2	20	13	1.30	134	10.5
I0.2-16	I	0.2	25	16	1.30	100	7.8
I0.2-20	I	0.2	30	20	1.30	78	6.1
I0.2-33	I	0.2	45	33	1.30	41	3.2
I0.2-47	I	0.2	60	47	1.30	22	1.7
I0.3	I	0.3	/	/	1.66	/	/
I0.3-24	I	0.3	30	24	1.66	61	4.8
I0.3-38	I	0.3	45	38	1.66	32	2.5
I0.4	I	0.4	/	/	1.95	/	/
I0.4-28	I	0.4	30	28	1.95	52	4.1
I0.4-42	I	0.4	45	42	1.95	27	2.1
I0.5	I	0.5			2.23		
I0.5-45	I	0.5	45	45	2.23	24	1.9
Br0.3	Br	0.3	/	/	1.36	/	/
Br0.3-13	Br	0.3	20	13	1.36	128	10.0
Br0.3-21	Br	0.3	30	21	1.36	75	5.8
Br0.3-34	Br	0.3	45	34	1.36	39	3.1
Br0.3-48	Br	0.3	60	48	1.36	21	1.7
Br0.4	Br	0.4	/	/	1.60	/	/
Br0.4-24	Br	0.4	30	24	1.60	63	5.0
Br0.4-37	Br	0.4	45	37	1.60	33	2.6
Br0.5	Br	0.5	/	/	1.83	/	/
Br0.5-26	Br	0.5	30	26	1.83	55	4.3
Br0.5-40	Br	0.5	45	40	1.83	29	2.3

Table 7.1*. Composition, fraction of pore filled and thickness of h-Li*$(BH_4)_{1-\alpha}(X)_\alpha$ *of investigated samples.*

a) Calculated density of h-Li$(BH_4)_{1-\alpha}(X)_\alpha$.

a) Calculation performed dividing the h-Li$(BH_4)_{1-\alpha}(X)_\alpha$ *occupied volume per gram of* SiO_2 *by the pore volume (*V_p*).*

b) Calculation performed considering the BET surface area of the SiO_2 *and assuming it as a plane.*

a-b) Calculated similarly to the calculation performed in ***Chapter 6*** *(see* ***Table 6.1****).*

Once, the stabilization of the hexagonal solid solutions and the complete solubilization of the halide have been verified by PXD, the samples were mixed, by ball milling, with SiO_2 (Aerosil 300, Evonik). All h-$Li(BH_4)_{1-\alpha}(X)_\alpha$-$SiO_2$ were ball-milled for three stints of 10 min at 300 r.p.m., separated by 1-min breaks.

The density of SiO_2 has been taken as 2.20 g/cm^3 from the literature.[130] The surface proprieties of SiO2 were obtained by N_2 adsorption at 77 K in a TriStar Plus II gas-volumetric apparatus (Micromeritics, Norcross, GA, USA). The specific surface area (S_{BET}) was calculated by fitting with a Brunauer–Emmett–Teller isotherm,[131] and it turned out equal to 294 m^2/g. The total pore volume (V_p) was derived from the absorbed volume of the nitrogen at p/p_o = 0.95 and it has been determined equal to 2.30 cm^3/g.

7.2.2. h-$Li(BH_4)_{1-X}X_X$ solid solutions

In the literature, the reported values for the solubility limits indicates that the h-$Li(BH_4)_{1-\alpha}(I)_\alpha$ solid solution is stable in the range $0.18 \leq x \leq 0.50$,[37] while the h-$Li(BH_4)_{1-\alpha}(Br)_\alpha$ solid solution is stable in the range $0.30 \leq x \leq 0.55$ as highlighted in **Chapter 4**. Following these limits ***I0.2***, ***I0.3***, ***I0.4***, ***I0.5***, ***Br0.3***, ***Br0.4*** and ***Br0.5*** samples have been synthetized, in order to have a composition inside the solubility limits. Patterns collected after the synthesis (BM+AN) of the samples ***I0.2***, ***I0.3***, ***I0.4***, ***I0.5***, ***Br0.3***, ***Br0.4*** and ***Br0.5*** are shown in **Figure 7.1**.

Figure 7.1 shows that all synthetized samples are monophasic. In fact, the only phase present is the $Li(BH_4)_{1-\alpha}(Br)_\alpha$ (**Figure 7.1a**) or the $Li(BH_4)_{1-\alpha}(I)_\alpha$ (**Figure 7.1b**) hexagonal solid solution and residual Bragg peaks of both the cubic halides (c-LiBr or c-LiI) and o-$LiBH_4$ starting materials were not detected.

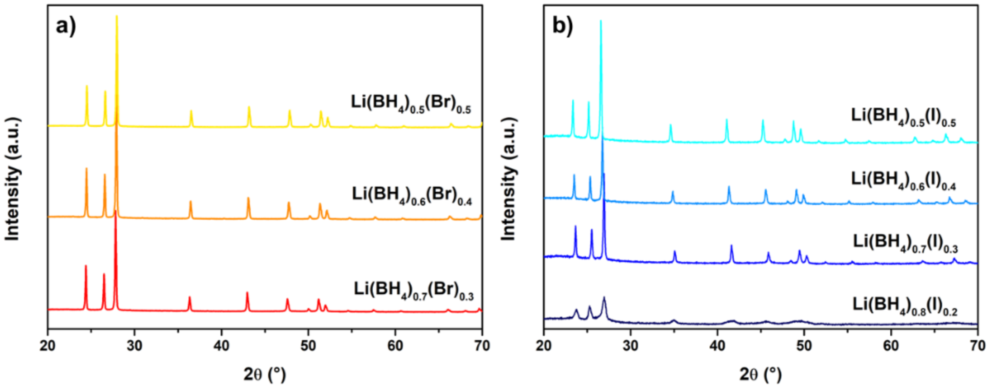

Figure 7.1. *a) PXD patterns of the samples* ***Br0.3***, ***Br0.4*** and ***Br0.5 b1****,* ***b2*** and ***b3*** *b) PXD patterns of the samples* ***I0.2***, ***I0.3***, ***I0.4*** and ***I0.5.***

These results confirm that the composition prepared are inside the solubility limits of the hexagonal solid solution reported in the literature, for both the binary systems. For the Rietveld refinement of the PXD patterns, the structural model of the hexagonal polymorph of $LiBH_4$ (*P63mc*) was used to describe the structure of h-Li$(BH_4)_{1-\alpha}(X)_\alpha$ solid solutions, where Br^- or I^- ions were constrained to lie on the same position of boron (*i.e. 2b* Wyckoff site). The lattice parameters and unit cell volume (*V/Z*) of the hexagonal phases, obtained from the Rietveld refinement of the PXD patterns, are reported in **Figure 7.2** as a function of the halide content.

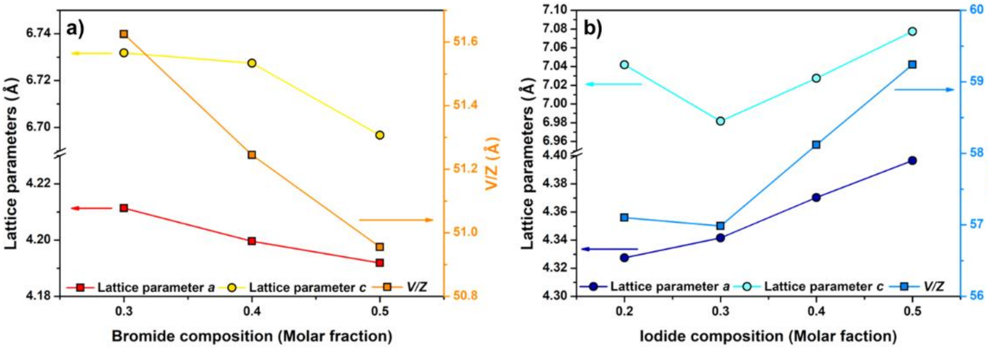

Figure 7.2. *Lattice parameters and unit cell volume (V/Z) as a function of the halide content (molar fraction) inside the monophasic a) h-Li$(BH_4)_{1-\alpha}(Br)_\alpha$ and b) h-Li$(BH_4)_{1-\alpha}(I)_\alpha$ hexagonal solid solutions.*

Figure 7.2a shows that both lattice parameters, as well as the unit cell volume, linearly decrease increasing the bromide concentration. Opposite behavior has been highlighted in **Figure 7.2b**, which demonstrates how the lattice parameters and the unit cell volume expand when the iodide concentration increases above 0.3.

The value of volume of the hexagonal $LiBH_4$ has been extrapolated at R*T* by using the value of the volumetric thermal expansion coefficient (2.9×10^{-4} K^{-1})[99]. The extrapolated volume of the hexagonal phase at R*T* is equal to 106.5 $Å^3$ (corresponding to a unit cell volume (*V/Z*) of 53.3 $Å^3$). The extrapolated R*T* cell volume value, of the h-$LiBH_4$, is higher with respect to that of sample ***Br0.3*** (51.6 $Å^3$). A contraction of the cell volume of the hexagonal solid solution is expected after halogenation, considering the smaller ionic radius of Br anion compared to that of BH_4^- (Br^-=1.96 Å with respect BH_4^-=2.03 Å).[36] On the contrary, considering the h-$Li(BH_4)_{1-\alpha}(I)_\alpha$ solid solutions, the lower volume of sample ***I0.2*** (*i.e.* equal to 57.0 $Å^3$) is higher with respect the R*T* extrapolated volume of h-$LiBH_4$, indicating an expansion of the lattice. The expansion is explained considering that the anion radius of the I^- is higher with respect to that of BH_4^- (I^-=2.20 Å with respect BH_4^-=2.03 Å).

Figure 7.2b shows that the lattice parameter *a* linearly increases with the iodide concentration, while lattice parameter *c* is found to shrink, with increasing the iodide content up to 0.3 and then to expand between 0.3 and 0.5. Considering the anion dimension difference between I^- and BH_4^-, this nonmonotonic evolution of the *c* axis is unexpected, but it was already reported by Sveinbjörnsson et al.[37]. They explained this unexpected behavior of the h-$Li(BH_4)_{0.8}(I)_{0.2}$ with the formation of some intermediate phases,[37,105] that could be the origin of the very asymmetric peak shape and large peak broadening visible in **Figure 7.1b**. A more detailed crystal structure analysis on this sample would be necessary in order to define the structure and to explain this nonmonotonic expansion of the *c*-axis.

Considering the I^- concentration above 0.3, the expansion of the *c* axis is expected, in agreement with values previously reported.[38,98]

The effect of the halogenation on the vibrational properties of lithium borohydride has been explored by IR-ATR spectroscopy. IR-ATR spectra were collected for all synthetized samples and the result are shown in **Figure 7.3**, together with the spectrum for pure o-$LiBH_4$.

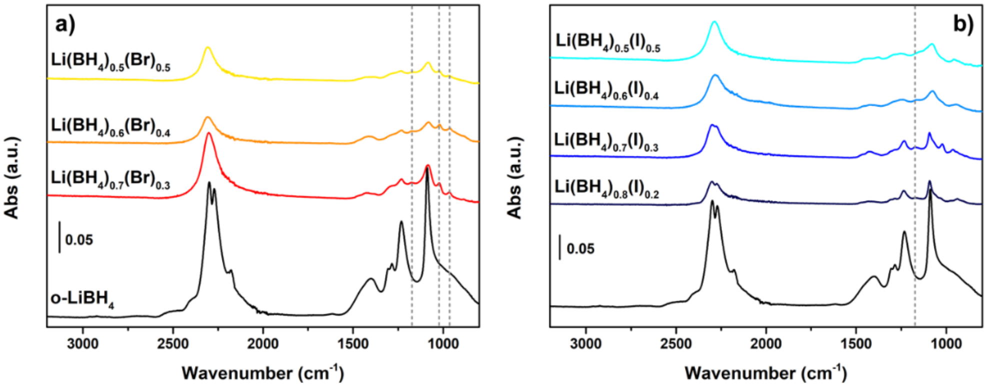

***Figure 7.3**. IR–ATR spectrum of pure $LiBH_4$ (bottom) and sample a) **Br0.3**, **Br0.4** and **Br0.5** b) **I0.2**, **I0.3**, **I0.4** and **I0.5**. Grey lines highlight the presence of new absorption bands.*

IR-ATR spectrum of o-$LiBH_4$ shows the two main sets of IR absorption bands. The bands in the 2400-2000 cm^{-1} region are due to stretching of the B-H bonds, while the bands in the 1600-800 cm^{-1} region are due to the B-H bending vibration modes.[77,94,98] The stabilization of the hexagonal phase of the $LiBH_4$ leads to a change in the corresponding vibrational spectra.[10,12] In particular, the well-defined IR absorption bands, in both B-H stretching and bending regions, become single and broad bands. Furthermore, the IR spectra in the low frequency region (1500-600 cm^{-1}) become even more complex than that of the parent o-$LiBH_4$ and reflects a change in the symmetry of the BH_4 anions. It is worth noting that Li-halide vibrational modes cannot be observed in the investigated spectral range. In the low frequency region, **Figure 7.3a** shows the presence of new peaks at ~1170 cm^-

^{1}, 1020 cm^{-1} and 960 cm^{-1}, according with Rude et al.[94]. In **Figure 7.3b**, only the presence of the peak at ~1170 cm^{-1} can be clearly evidenced in all spectra. In addition, increasing the iodide content, the B-H stretching bands increasingly become a single and broad band, reflecting an increase in the lattice distortion and disordering effects due to the higher iodide concentration.

In order to investigate the trend of Li-ion conductivity as a function of composition and temperature, temperature-dependent EIS measurements were performed in the temperature range 30 < T < 130 °C. The impedance spectroscopy measurements resulted in a Nyquist plot showing a single arc. The Nyquist plots were all fitted using an (RQ) equivalent circuit model, that is a resistor and a constant phase element in parallel. **Figure 7.4** shows an Arrhenius plot of the Li^{+} conductivities measured for all samples.

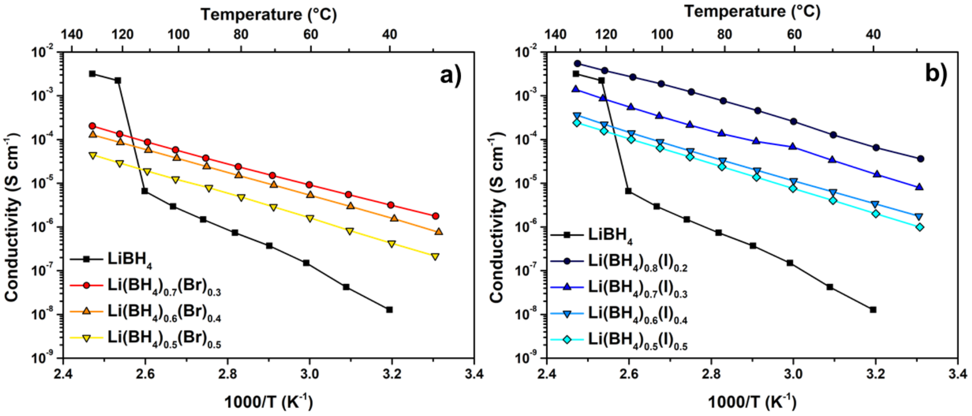

Figure 7.4. *Li-ion conductivity of samples a)* ***Br0.3****,* ***Br0.4*** *and* ***Br0.5*** *b)* ***I0.2****,* ***I0.3****,* ***I0.4*** *and* ***I0.5****. All data were obtained from the second heating temperature-dependent EIS cycle. Li-ion conductivity of the* *$LiBH_4$* *during the second heating temperature-dependent EIS cycle is shown for comparison.*

As expected for a hexagonal solid solution, the change in the conductivity due to the polymorphic transition, as observed for pure $LiBH_4$, disappears. In the h-$Li(BH_4)_{1-\alpha}(Br)_{\alpha}$ system (**Figure 7.4a**), sample ***Br0.3***, *i.e.* h-$Li(BH_4)_{0.7}(Br)_{0.3}$, shows the highest value for conductivity at 30 °C (1.8×10^{-6} S cm^{-1}), in agreement with the data reported in **Chapter 5**, while, in the h-$Li(BH_4)_{1-\alpha}(I)_\alpha$ system, is the sample ***I0.2***, *i.e.* h-$Li(BH4)_{0.8}(I)_{0.2}$, that shows the highest Li-ion conductivity (3.6×10^{-5} S cm^{-1} at 30 °C). It is worth noting that these values are about three orders of magnitude higher than that of pure $LiBH_4$ at *RT*. Before the phase transition, all samples show higher Li-ion conductivity with respect the $LiBH_4$, confirming that halogenation is a robust approach to enhance the Li-ion conductivity of the $LiBH_4$. In the temperature range 120-140 °C, sample ***I0.2*** shows a Li-ion conductivity even higher than the $LiBH_4$, that is stable in the hexagonal phase at these temperatures.

The Li-ion conductivity collected data, shows that a correlation exists between composition and ionic transport properties. The increase of the halide concentration inside the h-$Li(BH_4)_{1-\alpha}(X)_\alpha$ solid solution decreases the Li-ion conductivity, confirming that the presence of BH_4^- anions in the structure promotes the Li-ion mobility (see **Chapter 1**, paragraph 1.5.1). This consideration agrees with results reported in **Chapter 5**. In addition, this dependence of Li-ion conductivity as a function of the BH_4^- content is in good agreement with the calculations reported by Yao et al.[147]. By DFT calculations, Yao et al.[147] highlighted that, in h-$Li(BH_4)_{1-\alpha}(I)_\alpha$ solid solutions, higher I^- concentrations yielded a higher diffusivity but with a lower conductivity, in agreement with our results, where increasing the halide concentration causes a decreasing of the Li-ion conductivity.

As shown in **Figure 7.4**, the conductivity increases with temperature, as expected for a thermally activated process. Plots of ln (σT) as a function of 1000/T show a linear trend, therefore the activation energy (E_A) for Li-ion conductivity was obtained by a linear fit of the Arrhenius plots (see Equation **1.5**). **Figure 7.5** shows the activation energy value as a function of the halide content in h-$Li(BH_4)_{1-\alpha}(X)_\alpha$ solid solutions.

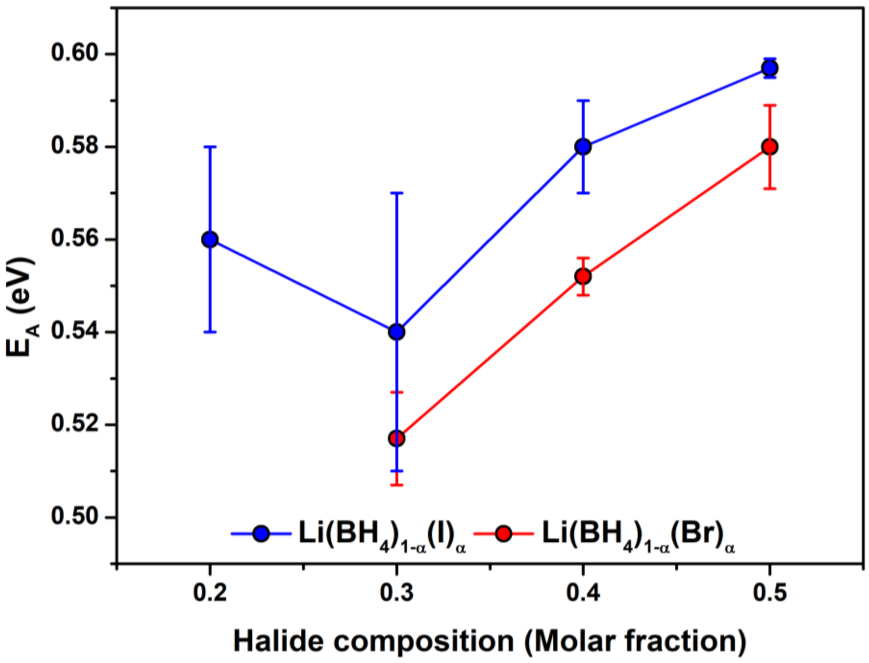

Figure 7.5. *Activation energy as a function of halide concentration in the h-*$Li(BH_4)_{1-\alpha}(X)_\alpha$ *solid solutions. The activation energy was calculated from data collected during the second heating ramp. Error bars were obtained from the linear fit of the Arrhenius plot (95% of confidence).*

The lowest value of activation energy is observed for both h-$Li(BH_4)_{1-\alpha}(X)_\alpha$ solid solutions when $\alpha = 0.3$ (*i.e.* 0.517 ± 0.01 eV for sample ***Br0.3*** and 0.54 ± 0.03 eV for sample ***I0.2***). In both h-$Li(BH_4)_{1-\alpha}(X)_\alpha$ solid solutions, above $\alpha = 0.3$, the activation energy increases. The trend of the activation energy as a function of the composition is in agreement with that reported in **Chapter 5**, for the h-$Li(BH_4)_{1-\alpha}(Br)_\alpha$ solid solutions, and by Miyazak et al.[38], regarding the h-$Li(BH_4)_{1-\alpha}(I)_\alpha$ solid solutions.

An unexpected behavior is evidenced for the sample ***I0.2***, *i.e.* h-$Li(BH_4)_{0.8}(I)_{0.2}$, that shows the highest conductivity, but its calculated activation energy is higher than that obtained for sample ***I0.3***. This behavior could be linked to the nonmonotonic expansion of the *c*-axis of the h-$Li(BH_4)_{1-\alpha}(I)_\alpha$ solid solution (**Figure**

7.2b), since the Li ion conduction occurs along the *c*-axis, as explained in **Chapter 1** (paragraph 1.5.1). The contraction of the *c*-axis detected for sample ***I0.2*** with respect sample ***I0.3*** (see **Figure 7.2b**), may cause a decreasing in the dimension of Li ion pathway, increasing the energy of migration and, consequently, the activation energy.

7.2.3. $(h\text{-}Li(BH_4)_{1-\alpha}(X)_{\alpha})_{1-\beta}\text{-}(SiO_2)_{\beta}$ systems

Recently, it has been reported that nanoconfinement and halogenation can be combined to enhance the ionic conductivity of $LiBH_4$.[148] So, the effect of the $(h\text{-}Li(BH_4)_{1-\alpha}(I)_{\alpha})_{1-\beta}\text{-}(SiO_2)_{\beta}$ system composition on the Li-ion conductivity has been evaluated, in order to understand if a possible synergetic effect is present between the halogenation and the interface engineering. The synthesis has been performed following the procedure suggested by Gulino et al.[84] (see **Chapter 6**). **Table 7.1** shows the samples synthetized with the *v/v* % of SiO_2 and the corresponding pore filling fraction. The *v/v* % of SiO_2 have been obtained by using the density values of the $h\text{-}Li(BH_4)_{1-\alpha}(X)_{\alpha}$ solid solutions, that have been calculated with the cell volume data obtained by Rietveld refinement. The SiO_2 composition range has been analyzed in more details for the $h\text{-}Li(BH_4)_{1-\alpha}(X)_{\alpha}$ solid solutions showing the highest Li-ion conductivity, *i.e.* $h\text{-}Li(BH_4)_{0.7}(Br)_{0.3}$ and $h\text{-}Li(BH_4)_{0.8}(I)_{0.2}$.

After the synthesis, a PXD analysis was performed at R*T* for each sample. **Figure 7.6a** shows the PXD pattern of $h\text{-}Li(BH_4)_{0.7}(Br)_{0.3}$ mixed with different *v/v* % of SiO_2, while **Figure 7.6b** shows the PXD pattern of $h\text{-}Li(BH_4)_{0.8}(I)_{0.2}\text{-}SiO_2$ mixtures.

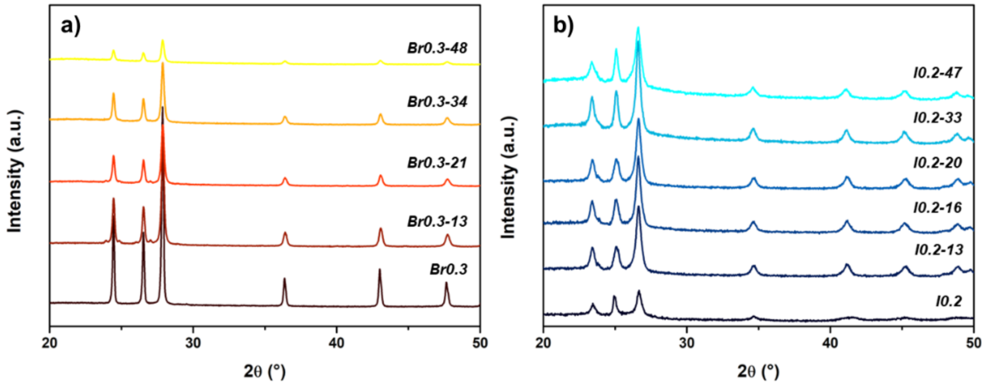

Figure 7.6. *PXD patterns of a) h-$Li(BH_4)_{0.7}(Br)_{0.3}$ b) h-$Li(BH_4)_{0.8}(I)_{0.2}$, with different v/v % of SiO_2.*

Figure 7.6 shows the PXD patterns of the h-$Li(BH_4)_{0.7}(Br)_{0.3}$ and h-$Li(BH_4)_{0.8}(I)_{0.2}$ solid solutions. Considering that SiO_2 is X-ray amorphous, **Figure 7.6** indicates the absence of both structural modifications due to the mechanochemical treatment and possible formation of new compounds.

Figure 7.7 shows that the ATR-IR collected for the (h-$Li(BH_4)_{1-\alpha}(I)_\alpha)_{1-\beta}$-$(SiO_2)_\beta$ mixtures.

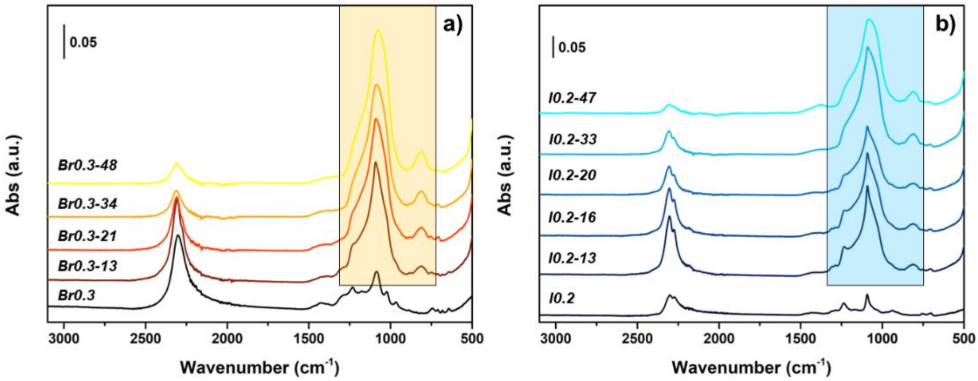

Figure 7.7. *IR–ATR spectra of sample a) h-$Li(BH_4)_{0.7}(Br)_{0.3}$ b) h-$Li(BH_4)_{0.8}(I)_{0.2}$, with different v/v % of SiO_2. The spectrum of sample **Br0.3** and **I0.2** are also reported (bottom).*

The absorption bands related to B-H stretching (2400-2000 cm^{-1} region) of the both h-$Li(BH_4)_{1-\alpha}(X)_\alpha$ solid solutions are not affected significantly by the mechanochemical treatment with SiO_2, showing a rather similar shape of the bands reported in **Figure 7.3**. The presence of the SiO_2 is clearly highlighted by the intense and broad absorption band in the region 1300-750 cm^{-1}.

The Arrhenius plots for the Li-ion conductivity in h-$Li(BH_4)_{0.7}(Br)_{0.3}$ and h-$Li(BH_4)_{0.8}(I)_{0.2}$ solid solutions, with different *v/v* % of SiO_2. are shown in **Figure 7.8**.

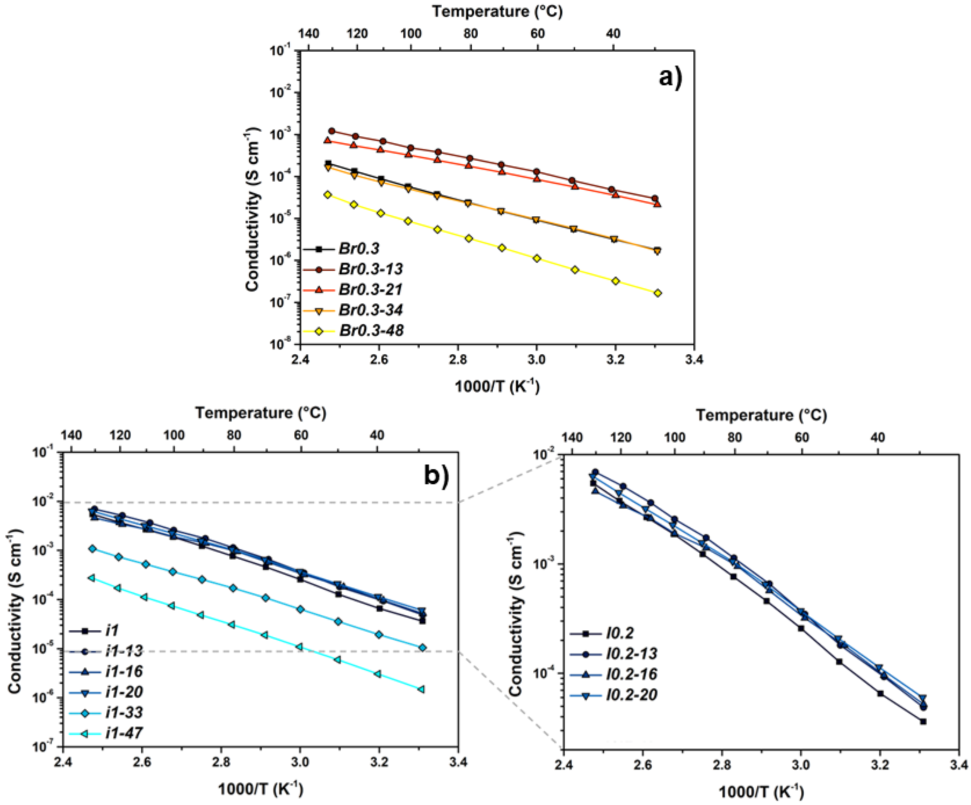

Figure 7.8. *Li-ion conductivity of a) h-$Li(BH_4)_{0.7}(Br)_{0.3}$ b) h-$Li(BH_4)_{0.8}(I)_{0.2}$, with different v/v % of SiO_2. All data were obtained from the second heating temperature-dependent EIS cycle. Li-ion conductivity of the a) h-$Li(BH_4)_{0.7}(Br)_{0.3}$ b) h-$Li(BH_4)_{0.8}(I)_{0.2}$ during the second heating temperature-dependent EIS cycle is shown for comparison.*

An increase of the Li-ion conductivity is achieved when the *v/v* % of SiO_2 is lower than 21 and 20 for h-$Li(BH_4)_{0.7}(Br)_{0.3}$ and h-$Li(BH_4)_{0.8}(I)_{0.2}$, respectively.

These volume fractions corresponds to a pore filling higher than 75 % and 78 % in the case of h-Li$(BH_4)_{0.7}(Br)_{0.3}$ and h-Li$(BH_4)_{0.8}(I)_{0.2}$, respectively. Among all h-Li$(BH_4)_{0.8}(I)_{0.2}$-SiO_2 mixtures (**Figure 7.8b**), those with v/v % of SiO_2 between 13 and 20 showed very similar conductivity ($9.3 \times 10^{-5} \div 1.1 \times 10^{-4}$ S cm^{-1} at 40 °C), indicating that the addition of the silica increases the Li-ion conductivity. The same behavior has been observed by the h-Li$(BH_4)_{0.7}(Br)_{0.3}$-SiO_2 mixtures (**Figure 7.8a**), even though the composite containing 13 v/v % of SiO_2 showed a more evident enhancement of the Li-ion conductivity with respect the h-Li$(BH_4)_{0.7}(Br)_{0.3}$ solid solution, reaching a Li-ion conductivity of 4.9×10^{-5} S cm^{-1} at 40 °C. In both (h-Li$(BH_4)_{1-\alpha}(I)_{\alpha})_{1-\beta}$-$(SiO_2)_{\beta}$ mixtures, for certain compositions, the addition of the oxide increases the Li-ion conductivity, indicating that a synergetic effect is present between the halogenation and interface engineering approaches.

On the other hand, for composites containing *wt.* % of SiO_2 higher than 30 % (*i.e.* 21 and 20 *v/v* % of SiO_2 for h-Li$(BH_4)_{0.7}(Br)_{0.3}$ and h-Li$(BH_4)_{0.8}(I)_{0.2}$, respectively), the Li-ion conductivity decreases.

The dependence on the pore filling of the Li-conductivity at 40 °C is shown in **Figure 7.9**. The Li-ion conductivity increases with the pore filling, reaching a high nearly constant value when it is higher than 80 %. In **Chapter 6** has been reported that the conductivity of the system $LiBH_4$-SiO_2 achieves maxium for a complete pore filling and it has been explained by a core-shell model, where two different $LiBH_4$ fractions are present: the first is at the interface, in direct contact with the oxide, resulting highly conductive, and the second fraction is in the bulk, showing the intrinsic conductivity of the $LiBH_4$.[45,84]

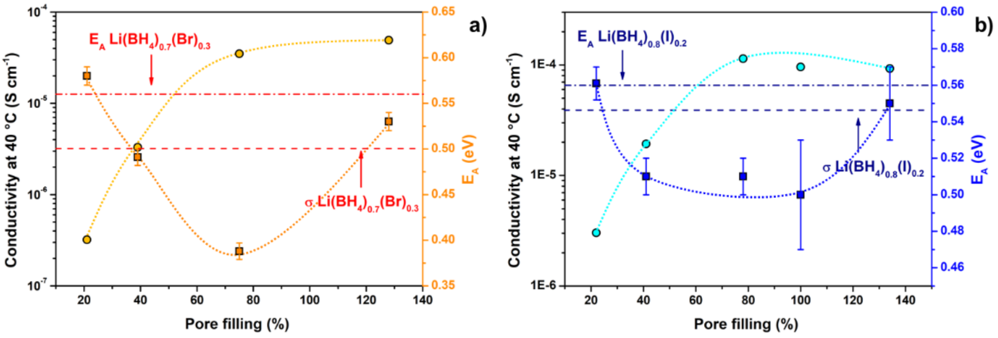

Figure 7.9. *Li-ion conductivity at 40 °C (circles) and activation energy (square) as a function of pore filling (%) for a) h-*$Li(BH_4)_{0.7}(Br)_{0.3}$ *b) h-*$Li(BH_4)_{0.8}(I)_{0.2}$ *solid solutions, with different v/v % of* SiO_2*. Dashed lines indicate the Li-ion conductivity at 40 °C of the h-*$Li(BH_4)_{1-\alpha}(X)_\alpha$ *hexagonal phases without oxide; Dash-dotted lines correspond to the activation energy calculated for the h-*$Li(BH_4)_{1-\alpha}(X)_\alpha$ *hexagonal phases without oxide; Dotted lines are a guide for the eye.*

Suwarno et al.[129] reported that the high conductive fraction of the $LiBH_4$, in direct contact with the oxide, does not undergo a structural phase transition and the thickness of this interface layer has been estimated to be equal to about 2 nm.[84,129] In the h-$Li(BH_4)_{1-\alpha}(X)_\alpha$-$SiO_2$ composites, the formation of the interface layer is confirmed by the enhancement of the Li-ion conductivity with respect the conductivity of h-$Li(BH_4)_{1-\alpha}(X)_\alpha$. Therefore, a core-shell model could be used to describe also these systems.

Figure 7.9 shows that for a pore filling >20 %, the E_A is lower than that obtained for the hexagonal solid solutions without SiO_2 and the lowest value of activation energy is observed for the sample containing an amount of SiO_2 close to a complete pore filling. These results are in agreement with those reported for the $LiBH_4$-SiO_2 (**Chapter 6**).

In samples where the pore filling far below 100 %, the insulator (*i.e.* SiO_2) interrupts the Li-ion pathway of the highly conductive interface layer, leading to a conductivity also lower than the h-$Li(BH_4)_{1-\alpha}(X)_\alpha$ solid solution without silica. The E_A obtained for these samples (*i.e.* containing an excess of silica) is comparable to that of the pure h-$Li(BH_4)_{1-\alpha}(X)_\alpha$ solid solutions. This result indicates that the Li-ion conductivity is dominated by the conduction inside the h-$Li(BH_4)_{1-\alpha}(X)_\alpha$ solid solutions and the amount of oxide is insufficient to form a well-connected interface layer. In addition, for these samples, the calculated thickness of the h-$Li(BH_4)_{1-\alpha}(X)_\alpha$ solid solutions over the oxide (see **Table 7.1**) is lower than the estimated dimension of the interface layer (*i.e.* 2 nm)[129], further confirming that this amount of oxide causes the interruption of the Li-pathway.

Differently form the system $LiBH_4$-SiO_2, when the volume of h-$Li(BH_4)_{1-\alpha}(X)_\alpha$ solid solution exceeded the pore volume (pore filling > 100 %), the interface layer is no more interrupted by the low conductive o-$LiBH_4$, but the connectivity of Li-ion pathway is guaranteed by the high conductive h-$Li(BH_4)_{1-\alpha}(X)_\alpha$.[149] In addition, the calculated values of the E_A show that, when the amount of hydride overcomes the complete pore filling, the E_A value returns to be comparable to that of h-$Li(BH_4)_{1-\alpha}(X)_\alpha$ solid solutions without silica, indicating that the excess of the solid solution dominates the conduction mechanism. Therefore, only in the case of too high-volume fractions of insulating materials (i.e. pore filling < 100 %), a deviation from a complete filling of pores cannot provide a well-connected interface layer network, leading to a decrease of the Li-ion conductivity of the composite.

Finally, **Figure 7.10** shows a complete overview of the synthesized composites, in order to individuate if the composition of the solid solutions could affect the synergetic effect.

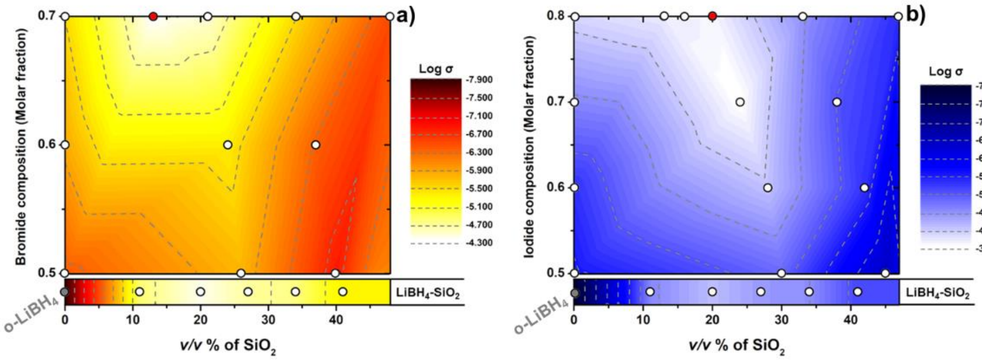

Figure 7.10. *Contour map of Log σ at 40°C as a function of the amount of* SiO_2 *and of a) h-*$Li(BH_4)_{1-\alpha}(Br)_\alpha$ *b) h-*$Li(BH_4)_{1-\alpha}(I)_\alpha$ *composition. Isoconductivity dashed lines correspond to the values and lines shown in the legend. The red circles indicate the highest Log σ reached in each system, while grey circles indicate the Log σ of the o-*$LiBH_4$*. The Log σ values of the sample* $LiBH_4$*-*SiO_2 *has been taken from ref.*[84].

Figure 7.10 show that, for both systems, the synergetic effect occurs when the quantity of SiO_2 is between 20 and 30 v/v % (*i.e.* pore filling between about 50 ÷ 134 %). In any case, the maximum Li-ion conductivity is reached for the samples containing the solid solution with the highest BH_4^- content, that is the principal parameter that affects the conductivity in the h-$Li(BH_4)_{1-\alpha}(X)_\alpha$, as discussed above.

7.3. Conclusions

In this chapter the effect of the halide content has been analyze inside the solubility limits of the h-$Li(BH_4)_{1-\alpha}(X)_\alpha$ for the system $LiBH_4$-LiI and $LiBH_4$-LiBr. The structural proprieties of the h-$Li(BH_4)_{1-\alpha}(X)_\alpha$ solid solution has been studied by PXD and ATR-IR, while the Li-ion conductivity by EIS. Once the more conductive h-$Li(BH_4)_{1-\alpha}(X)_\alpha$ solid solution in each system was individuated, the effect of adding SiO_2 has been analyzed. When the hexagonal solid solution completely fills the pore of the oxide, an increase of the h-$Li(BH_4)_{1-\alpha}(X)_\alpha$ Li-ion conductivity has been highlighted. Therefore, a synergetic effect between these two approaches, *i.e.* halogenation and interface engineering, has been highlighted in this chapter, indicating a promising insight to synthetized novel solid-state electrolytes.

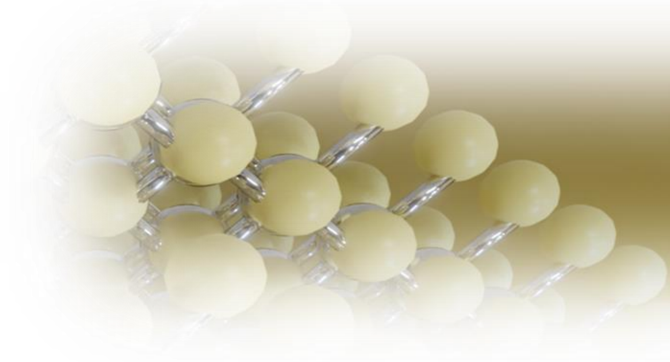

Chapter 8.

Room Temperature Solid-State Lithium-ion Battery using $LiBH_4$-MgO composite Electrolyte

---

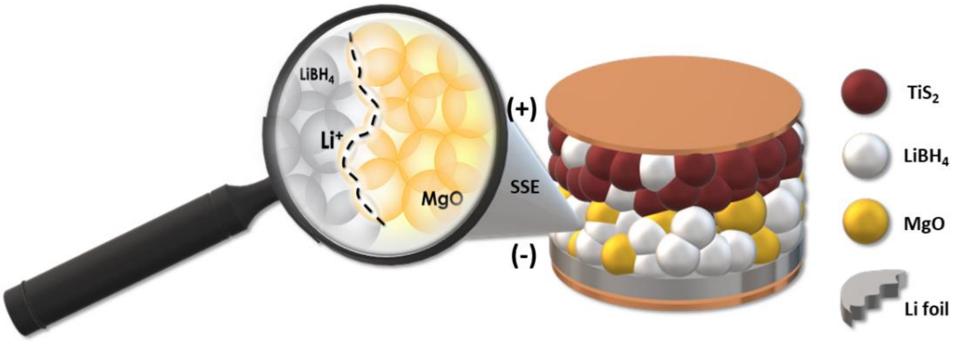

8.1. Introduction

$LiBH_4$ was studied as SSE in several SSB,[46] using TiS_2[47] or sulphur[48] as cathode materials. These SSBs operate at temperature of about 120 °C, allowing a sufficient Li-ion conductivity, given by the hexagonal polymorph. The working potential of both TiS_2 and S is about 2 V *vs.* Li^+/Li,[47,48] close to the oxidative limit of $LiBH_4$, which explains the sluggish, but progressive, observed capacity fading. In order to decrease the working temperature, Unemoto et al.[49] used a $LiBH_4$-P_2S_5 mixture, obtaining a poor cycling, limited to 10 cycles. Das et al.[50] reported a SSB working at 55 °C, using $LiBH_4$ nanoconfined in silica nanoscaffold as SSE, obtaining 60 charge/discharge cycles.

Different approaches and Li-ion conductors has been reported in the previous chapters. **Figure 8.1** reports the Li-ion conductivity of the more promising samples.

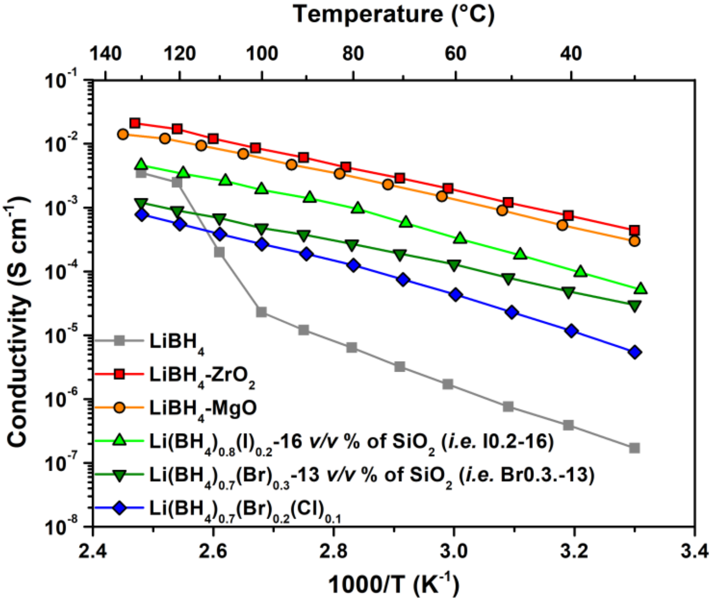

Figure 8.1. *Li-ion conductivity of the second heating temperature-dependent EIS cycle of the most promising samples, as reported in the previous chapters. Grey line corresponds to the Li-ion conductivity of pure* $LiBH_4$.

Increasing the Li-ion conductivity of the $LiBH_4$, by the optimization of the composition of $LiBH_4$-based SSEs, can reduce the working temperature of the $LiBH_4$-based SSBs. Therefore, the aim of this chapter is to design a $LiBH_4$-based system as improved SSE for R*T* SSB.

The $LiBH_4$-MgO system was selected considering the samples reported in **Figure 8.1**, and the effect of the composition on the Li-ion conductivity was first established. The other promising candidate, $LiBH_4$-ZrO_2, is an on-going study in collaboration with the Tohoku University (Professor S. Orimo).

The electrochemical stability window, measured by cyclic voltammetry (CV), was then determined, in order to investigate the effect of the oxide matrix on the electrochemical stability of $LiBH_4$. A solid-state cell configuration, *i.e.* TiS_2|SSE|Li, was selected as electrochemical system, focusing on the characterization of the composite $LiBH_4$-MgO as SSE for SSBs. These composites allowed to decrease the operating temperature of the $LiBH_4$-based SSB down to 60 °C and even down to R*T*, compared to the 120 °C of pure $LiBH_4$. After the formation of a stable solid electrolyte interphase at 60 °C, it was possible to succesfully operate the SSB at R*T* for more than 30 cycles, with a discharge capacity retention of 80 %.8.2. Results and discussion

8.2. Results and discussion

8.2.1. Synthesis

$LiBH_4$ (purity >95 %, Alfa Aesar) was mixed with MgO (Steam Chemicals) in different ratios, as reported in **Table 8.1**. In order to remove the physisorbed/chemisorbed water, MgO was pelletized and dried at 300 °C in a furnace, under dynamic vacuum (by rotative pump), for 6 hours. As-received $LiBH_4$ was ball-milled for 2 hours at 500 r.p.m. and was used as starting material for the $LiBH_4$-oxide composite. All samples were ball-milled for three stints of 10 min at 300 r.p.m., separated by 1-min breaks.

The density of MgO has been taken as 3.58 g/cm^3 from the literature.[130] The surface proprieties of MgO were obtained by N_2 adsorption at 77 K in a TriStar Plus II gas-volumetric apparatus (Micromeritics, Norcross, GA, USA). The specific surface area (S_{BET}) was calculated by fitting with a Brunauer–Emmett–Teller isotherm,[131] and it turned out equal to 215 m^2/g. The total pore volume (V_p) was derived from the absorbed volume of the nitrogen at $p/p_0 = 0.95$ and it has been determined equal to 0.25 cm^3/g.

Sample name	**Oxide fraction**		**Fraction of pore filled**[a)]	**Thickness of $LiBH_4$**[b)]
	wt. %	**v/v %**	**%**	**nm**
26CE	65.0	26	323	3.8
53CE	85.7	53	100	1.2
74CE	94.0	74	38	0.4

Table 8.1. *Composition, fraction of pore filled and thickness of $LiBH_4$ of investigated samples.*
a) Calculation performed dividing the $LiBH_4$ occupied volume per gram of MgO by the pore volume (V_p).
b) Calculation performed considering the BET surface area of the oxides and assuming it as a plane.

8.2.2. Optimization of the composition

The effect of the composition on the Li-ion conductivity in $LiBH_4$-MgO system has been evaluated following the procedure suggested in ref.[84], *i.e.* **Chapter 6**. Three samples have been synthetized, with a v/v % of MgO corresponding to a pore filling fraction of 1/3, 1 and 3 (**CE26**, **CE53** and **CE74**, respectively), as reported in **Table 8.1**.

The AC-conductivity of the composites as a function of the inverse temperature is shown in **Figure 8.2a**.

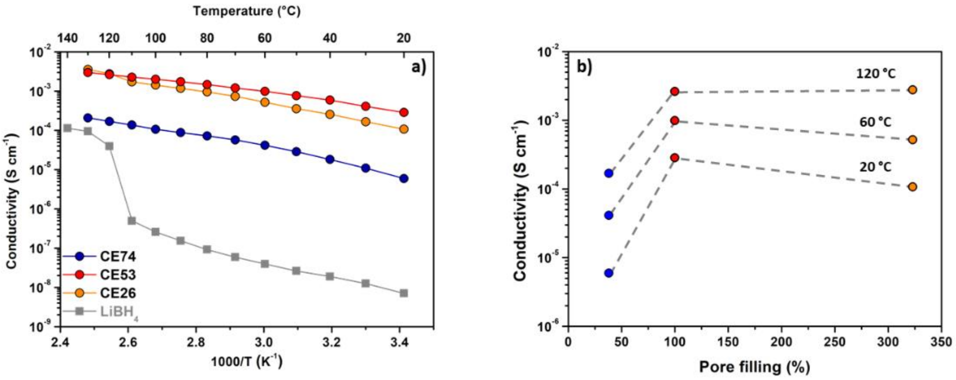

Figure 8.2. *a) Li-ion conductivity of the second heating temperature-dependent EIS cycle of* $LiBH_4$*-MgO composites with different oxide fractions. Grey line corresponds to the Li-ion conductivity of pure* $LiBH_4$*.*[77] *b) Li-ion conductivity at 20, 60 and 120 °C as a function of the pore filling. Dashed lines are a guide for the eyes.*

Figure 8.2a shows that at RT sample **CE53** shows the highest Li-ion conductivity (2.86 $\times 10^{-4}$ S cm^{-1} at 20 °C), about four orders of magnitude higher than pure $LiBH_4$. The 20 °C Li-ion conductivity of **CE26** and **CE74** were 1.07 $\times 10^{-4}$ and 5.94 $\times 10^{-6}$ S cm^{-1}, respectively. The Li-ion conductivity of sample **CE26** at 40 °C (2.57 $\times 10^{-4}$S cm^{-1}) is in agreement with the data already reported for the same composition and at the same temperature (1.80 $\times 10^{-4}$ S cm^{-1})[84]. The dependence on the pore filling of the Li-conductivity at various temperatures is shown in **Figure 8.2b**. The maximum σ value is observed for a 100 % pore volume filling (**Figure 8.2b**), confirming the trend previously reported by Gulino *et al.*[84]. The 20 °C impedance spectra (composed by a single arc and a low frequency linear dispersion) are plotted together in the Nyquist plot in **Figure 8.3**.

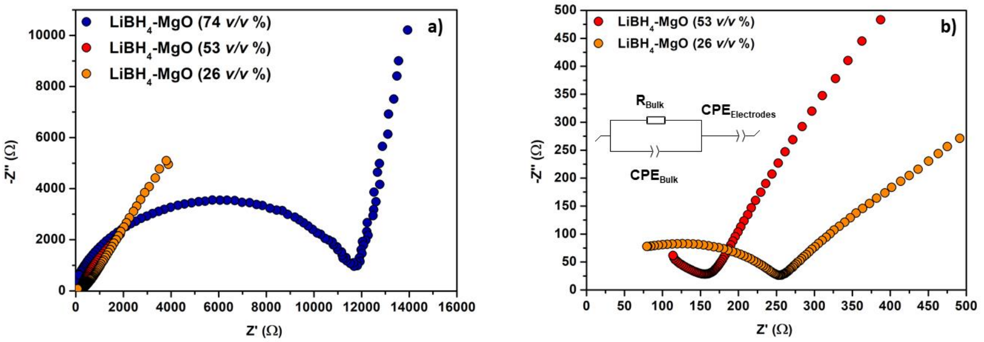

Figure 8.3. *a) Impedance spectra shown on the Nyquist plot for the different LiBH$_4$-MgO compositions at 20 °C. b) Impedance spectra shown on the Nyquist plot for* ***CE26*** *and* ***CE53****. The insets show the equivalent electrical circuits used to fit the data.*

In order to explore the phase composition of the different composite, after synthesis, the Powder X-Ray Diffraction (PXD) patterns were collected (**Figure 8.4**). Orthorhombic LiBH$_4$ was detected only for sample **CE26**, *i.e.* for a pore filling higher than 100 %, indicating that the excess of hydride contained in this composite is partially present as R*T* polymorph.

From the trend of data reported in **Figure 8.2a**, it is worth noting that different conductive regimes are likely present, indicating a complex temperature-dependent Li-ion conduction mechanism in the investigated temperature range. This type of behaviour has been previously reported for complex hydrides,[150] as well as for different classes of materials studied as SSE,[151] and can be assigned to different ion-ion interaction regimes. Further investigation, *i.e.* combining solid-state NMR and large frequency and temperature range EIS measurements,[149,150] is needed in order to clarify this aspects.

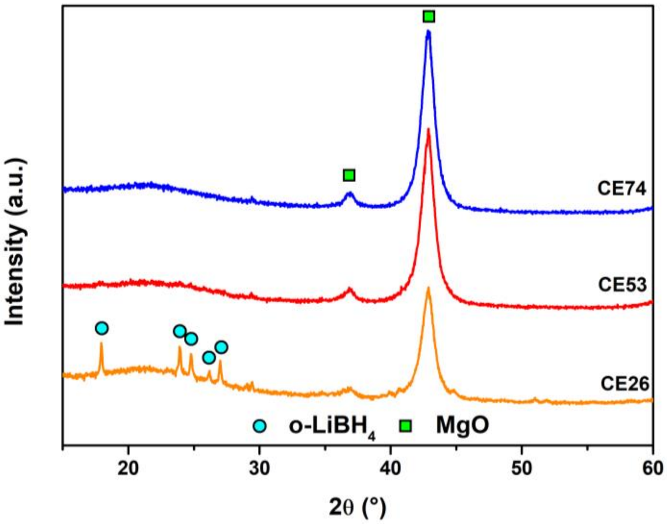

Figure 8.4. *a) PXD patterns of LiBH$_4$-MgO composites with different compositions.*

The activation energy for **CE53** sample was obtained by fitting linearly ($R^2 > 0.999$) the $\ln(\sigma T)$ *vs.* $1/T$ data shown in **Figure 8.2a** below 60 °C, where data suggests an Arrhenius-type temperature dependence. The so-obtained E_a is equal to 0.29 ± 0.03 eV below 60 °C, a similar value as found for other SSEs.[152] The obtained E_a is considerably lower than to the average value reported in the literature for pure LiBH$_4$ (0.75 ± 0.07 eV, see **Chapter 3**)[153]. The E_a for Li-ion conductivity is composed of two contributions: the energy needed for the Li$^+$ jump, *i.e.* the energy of migration (E_m), and the energy of defect formation (E_f).[14,154] The observed low value of E_a for sample **CE53** can be explained considering a reduction of the energy for defect formation (E_f) established by the interface layer,[30] since the calculated migration energy of the o-LiBH$_4$ (*i.e.* 0.10-0.30 eV)[30] is similar to that of the hexagonal phase (*i.e.* 0.31 eV)[29]. This behavior might be explained by the space charge layer (SCL) model, that has been proposed to describe the interface between semiconductors and insulators.[155,156] Nevertheless, Lambregts *et al.*[157] demonstrated, by solid-state NMR, that the interface layer between LiBH$_4$ and silica is characterized by a high ion dynamics, for both BH$_4^-$ and Li$^+$, and cannot be defined with a clear structure, so that it is not possible to directly refer to the SCL model. The exact relation between the interface layer structure and the dynamics of ions needs further investigation.

For sample **CE74**, the pore filling fraction is lower than 100 %, therefore the highly conductive phase does not percolate throughout the sample and the conductive pathway is interrupted by the oxide. A similar effect occurs in the sample **CE26**, where the excess of the low conductive orthorhombic $LiBH_4$ interrupts the conductive pathway.

The Li-ion conductivity for the **CE53** sample is about one order of magnitude higher than values previously reported for $LiBH_4$-SiO_2-based composites SSEs: at 40 °C Blanchard *et al.* obtained 1.0×10^{-5} S cm^{-1} for 28 *v/v* % of MCM-41,[45] Choi *et al.* 1.5×10^{-5} S cm^{-1} for 55 *v/v* % of fumed silica[42] and Gulino *et al.* 4.1×10^{-5} S cm^{-1} for 20 *v/v* % of SiO_2[84] (see **Chapter 6**).

CE74 and **CE53** composites do not show, at 110 °C, the typical step in the Li-ion conductivity due to the phase transition of the $LiBH_4$, which is slightly visible for the **CE26** sample, as shown in **Figure 8.5**.

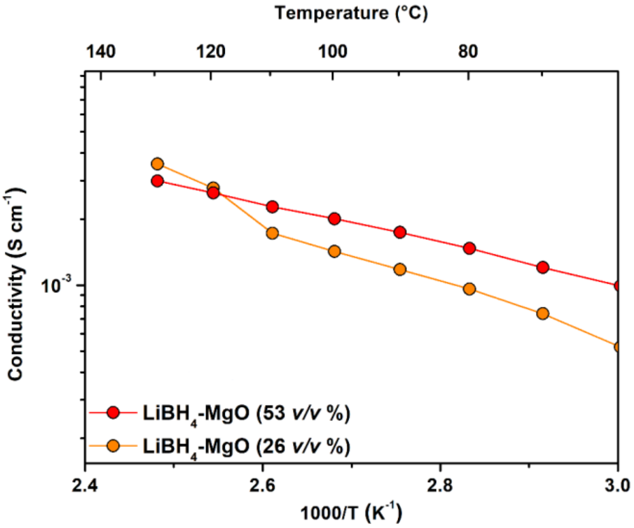

Figure 8.5. *Li-ion conductivity of the second heating temperature-dependent EIS cycle of $LiBH_4$-MgO composites with different compositions.*

This suggests that the contribution of the hexagonal phase of $LiBH_4$ is negligible in the **CE74** and **CE53** samples at high temperatures, whereas it is relevant for the **CE26** sample.[84] This behaviour can be explained by considering the estimated values for the thickness of the $LiBH_4$ layer on MgO (see **Table 8.1**). The calculation was performed taking into account the surface area of the MgO and assuming that it is fully and uniformly covered by $LiBH_4$.[84] The highly conductive layer of $LiBH_4$ in direct contact with the oxide, the thickness of which has been estimated to be about 2 nm, does not undergo a structural phase transition.[84,129] Indeed, for samples **CE74** and **CE53**, the calculated thickness of $LiBH_4$ is 0.4 and 1.2 nm, respectively (see **Table 8.1**), which are close to values estimated in the literature.[84,129] On the other hand, the calculated thickness of $LiBH_4$ for the composite **CE26** amounts to 3.8 nm, explaining the slight increase of the Li-ion conductivity above 110 °C (**Figure 8.2a**) and confirming that the bulk $LiBH_4$ contributes to the Li-ion conductivity after the phase transition.

8.2.3. Electrochemical stability

Next to a high Li-ion conductivity, a suitable SSE should have a wide electrochemical stability window and a good chemical compatibility with electrodes. The electrochemical stability of the **CE53** sample has been evaluated by CV at 60 °C (**Figure 8.6a**). The interface between a solid electrolyte pellet and a flat metallic Au working electrode can result in a low contact surface area and thus a high interface resistance, which can cause difficulty in the signal detection, *e.g.* overestimating the electrochemical stability window. Therefore, in order to increase the probed surface, carbon material was added, as described elsewehere.[79,158]

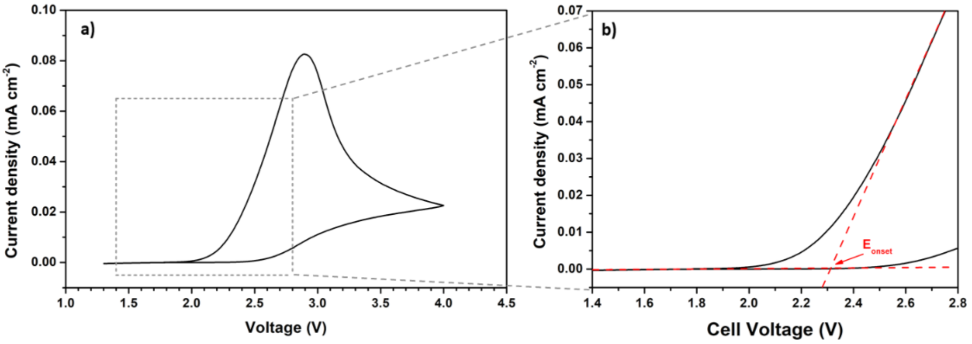

Figure 8.6. *a) Linear sweep voltammograms of Li|**CE53**|CE53-C|stainless steel cells at scan rates of 20 µV s^{-1} from 1.3 to 4.0 V vs Li$^+$/Li at 60 °C. b) E_{onset} estimation from two linear regression lines of the non-faradaic background current and faradaic anodic current.*

The oxidative limit (E_{onset}) was determined from the intersection of two linear regression lines ($R^2 > 0.99$) of the background current and the faradaic oxidative current at positive potential *vs.* Li$^+$/Li (**Figure 8.6b**), following the approach suggested by Asakura *et al.*[78] It falls at about 2.3 V *vs.* Li$^+$/Li, which is in agreement with values reported for $LiBH_4$ by Asakura *et al.*[78] and Gulino *et al.*[77] (see **Chapter 5**). This result suggests that the addition of MgO matrix only affects the ionic conductivity, leaving the electrochemical stability of $LiBH_4$ unchanged.

The chemical compatibility towards metallic lithium was evaluated with galvanostatic cycling in a Li|**CE53**|Li symmetrical cell at 60 °C, allowing to determine also the extent of the reversible lithium plating/stripping at the SSE surface and, at the same time, its reductive stability. The results, shown in **Figure 8.7**, demonstrate that lithium is plated and stripped reversibly for over 90 hours.

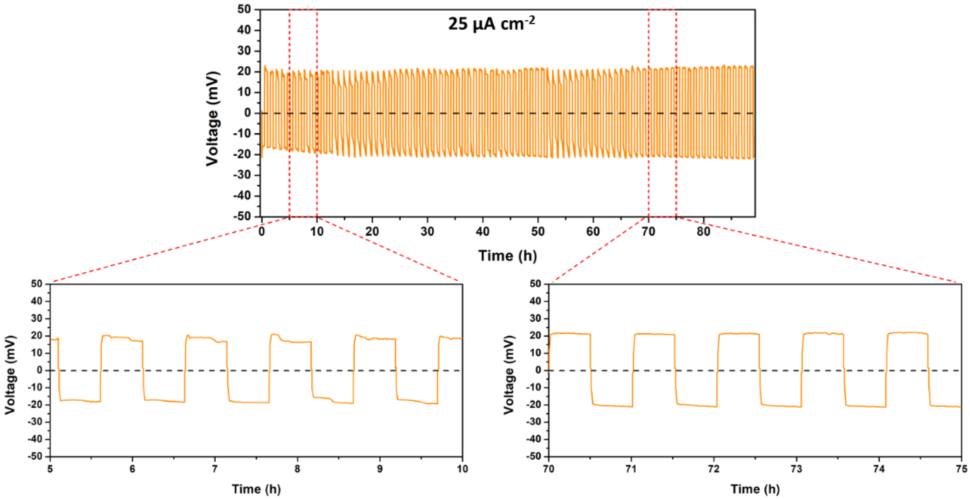

Figure 8.7. *Galvanostatic cycling profiles of symmetrical Li|**CE53**|Li cell at 60 °C with current density of 25 µA cm^{-2}for 30 min sweeps.*

The cell polarization is rather steady at 20 mV for the whole period, indicating a long-term stability and that no parasitic reactions between SSE and lithium occur in this low potential region. Indeed, a well-performing electrochemical material should show a stable polarization, reflecting the electrolyte resistivity and interfacial effects, in case they are present.

The contact resistance of the cell was calculated by multiplying the cell resistance (after having subtracted the SSE contribution), divided by a factor two (since the two interfaces are considered equivalent), by the contact surface. It turns out to be about 565 Ω cm^2, a much higher value than that reported by Kim *et al.*[23] on carboranes SSEs (<1 Ω cm^2). In the absence of a proper cell stack pressure, which would guarantee an intimate contact between lithium and the SSE surfaces, a high contact resistance, increasing during cycling, is expected,[159,160] explaining the observed value.

8.2.4. Battery test

The elecrochemical properties of the **CE53** composite SSE was tested in a SSB, selecting TiS_2 and Li as positive and negative electrode, respectively. Lithium increases the energy density with respect to the commercial graphitic anodes,[161,162] while TiS_2 is widely used for $LiBH_4$-based SSBs.[47] In the current study, TiS_2 has been selected also to obtain a valid comparision with the system reported by Unemoto *et al.*[47].

The Li-ion conductivity of **CE53** at 20 °C amounts to 2.86×10^{-4} S cm^{-1} and it is sufficient to operate the battery at R*T* at low current regimes.[8,163] Therefore, a freshly-prepared cell was built and cycled at R*T*, without any conditioning. **Figure 8.8** depicts the Galvanostatic Cycling with Potential Limitation (GCPL) profile of the Li|**CE53**|TiS_2 cell, operating with a current density of 24 mA g^{-1} (C/10).

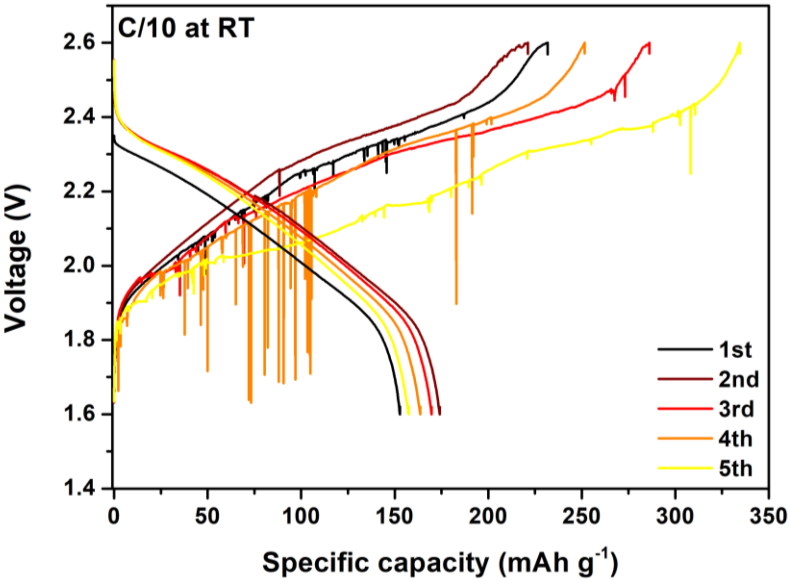

Figure 8.8. *Voltage profiles of Li|**CE53**|TiS cell for a rate of C/10 (i.e. 24 mA/g) at RT.*

Figure 8.8 shows that it was possible to collect data for only 5 cycles before the cell failure and several spikes are visible in the charge profiles, but they are completely missing during discharges. This results suggest an inhomogeneous Li-plating and it may be induced by the imposition of a current density exceeding the so-called critical current density (CCD),[164,165] which is also a function of the cell stack pressure.[160]

A significant difference was observed between the discharge capacity at the first and the second cycle; 52 and 173 mA h g^{-1}, respectively. A similar behaviour has been observed by Unemoto *et al.*[47] for the Li|$LiBH_4$|TiS_2 battery, operating at 120 °C. By probing the evolution of $LiBH_4$ into $Li_2B_{12}H_{12}$, it has been related to a partial instability of the TiS_2/$LiBH_4$ interface, forming H_2 and additional Li, that self-diffuses into TiS_2, self-discharging the battery.[47] The recently reported electrochemical window of $LiBH_4$ of 2.2/2.3 V *vs.* Li^+/Li, clarifies that the TiS_2/$LiBH_4$ interfacial instability arises when the $LiBH_4$ oxidation potential is exceeded.[77,78] In the present case, the self-discharging reaction to form a solid electrolyte interface (SEI), as evidence by the capacity difference between the first and the second cycle, is much less extended than that reported by Unemoto *et al.*[47] (*i.e.* discharge capacity of 80 and 205 mA h g^{-1} for the first and the second cycle, respectively). This is probably due to a kinetic limitation in the reaction of $LiBH_4$ to form $Li_2B_{12}H_{12}$, as a consequence of the lower temperature.

In order to gain further insights into the effect of the temperature on the formation of the SEI, a freshly-prepared cell was built and cycled at 60 °C. **Figure 8.9a** shows the GCPL profile of the Li|**CE53**|TiS_2 cell operating at 60 °C and with a current density of 11.8 mA g^{-1} (corresponding to C/20).

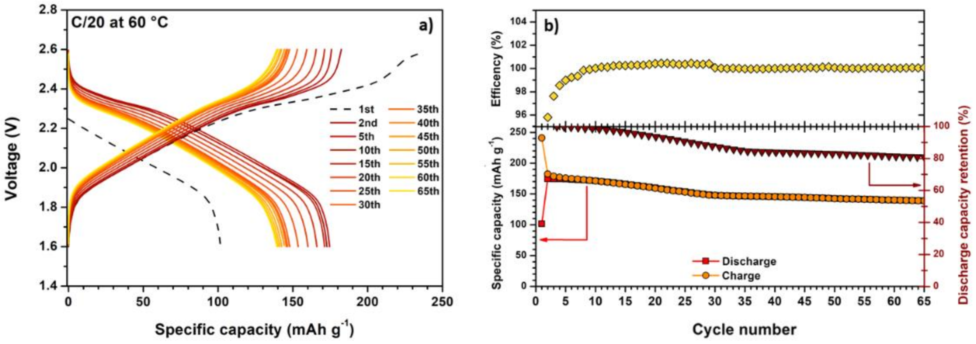

Figure 8.9. *a) Voltage profiles of Li|**CE53**|TiS_2 cell for a rate of C/20 (11.8 mA g^{-1}) at 60 °C. b) Discharge/Charge specific capacity, Coulombic efficiency (discharge capacity over charge capacity), and discharge capacity retention ratio as a function of cycle number for the same cell. The capacity of the battery is expressed per g of TiS_2.*

For the sake of clarity, only selected galvanostatic profiles are shown. A high capacity retention was observed over 65 cycles when the battery operated at 60 °C. A rather low discharge capacity has been observed at the first cycle (101 mA h g^{-1}). On the other hand, its value at the second cycle amounts to 175 mA h g^{-1}, that corresponds to about 73 % of the theoretical capacity of TiS_2 (239 mA h g^{-1}).[166–168]

The self-discharge due to the formation of $Li_2B_{12}H_{12}$ SEI is observed also in this case, but with a higher extent with respect to the test performed at R*T* (**Figure 8.8**). The higher self-discharge observed is consistent with a faster kinetics of the reaction of $LiBH_4$ to form $Li_2B_{12}H_{12}$ which is favoured by the higher temperature.

Figure 8.9b shows the discharge/charge capacity, Coulombic efficiency, and discharge capacity retention ratio to the second discharge, as a function of cycle number. The capacity retention has been calculated with respect to the second discharge capacity, since in the first run the capacity is overestimated, due the self-discharge reaction occurring at the TiS_2/$LiBH_4$ interface. The discharge capacity retention is more that 80 % after 65 cycles, which is promising for a stable battery operation at this temperature.

It is worth noting that after the 30th cycle (**Figure 8.9a**), a pronounced decrease of the capacity is observed (*i.e.* discharge capacity of 174, 147 and 139 mA h g^{-1} for the 2nd, the 30th and the 65th cycle, respectively). On the other hand, the Coulombic efficiency is always close to 99.9 % up to the 10th cycle (**Figure 8.9b**), indicating that the capacity fading occurs during the charge, namely at voltage higher than the oxidative stability of $LiBH_4$.

To clarify the cause of this effect, the cell impedance was monitored after each charge/discharge cycle and results are reported in **Figure 8.10**.

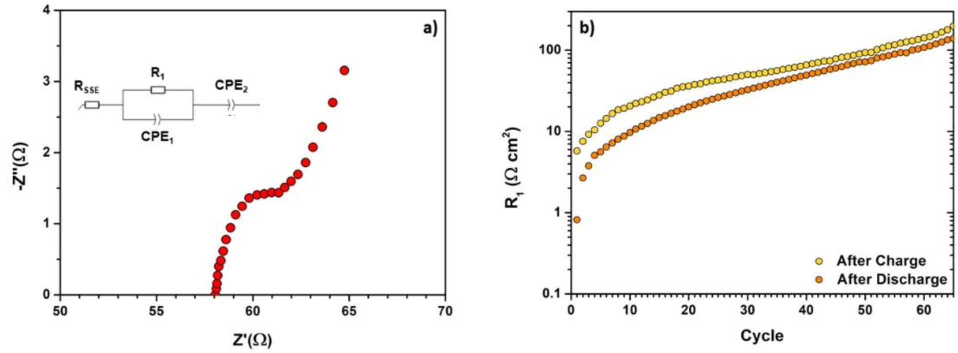

Figure 8.10. *a) Nyquist plot of Li|CE53|TiS_2 cell before the first discharge. The inset shows the equivalent electrical circuit used to fit the data. R_{SSE} is the electrolyte resistance, while R_1 correspond to the contact resistance b) Contact resistance (R_1) evolution obtained by in situ EIS for the same cell, plotted in logarithmic scale.*

Figure 8.10a shows the Nyquist plot before the first discharge cycle of the cell. The impedance spectra was fitted using the equivalent circuit shown in the inset. It was not possible to resolve the SSE relaxation because of the limited instrumental high frequency range (20 kHz). Therefore, R_{SSE} accounts for the electrolyte and all the fast processes that can occur and its value was considered constant during cycling. A second contibution to the circuit is present at lower frequency (labelled R_1) and it was assigned to the contact resistance. **Figure 8.10b**

shows the evolution of the contact resistance (R_1) as a function of the charge/discharge cycles.

The contact resistance (R_1), at the very first discharge, is <1 Ω (similar to that obtained by Kim *et al.*)[23], and afterwards it quickly increases in the first ten cycles, reaching then a steady exponential increase. This behaviour can be understood considering the sum of two contributions. The first one is the formation of the $Li_2B_{12}H_{12}$-based SEI layer, that is poor conductive at 60 °C (lower than 10^{-6} S cm^{-1})[169]. The decrease of the capacity fading at the 30th cycle could correspond to the achievement of the maximal SEI thickness. The second contribution, being the cell not supported by an appropriate stack pressure, is likley due to a continuous loss of contact at the electrodes interfaces. In fact, during the de-lithiation of TiS_2, a volume contraction of $\Delta V/V = -9.7$ % is experienced, which also explains the rather high contact resistance after each charge cycle (**Figure 8.10**), *i.e.* after Li plating at the negative electrode. The Li_xTiS_2 $\Delta V/V$ value was estimated assuming a complete de-intercalation, so considering the unit cell volume at the two intercalation extremes, $x = 0$ and at $x = 1$. In addition, considering the negative side of the cell, a similar trend of the contact resistance has been reported by Krauskopf *et al.*[170], when the current density is higher than a critical value (*i.e.* 200 μA cm^{-1} at R*T*) without a suitable external applied pressure. Therefore, we assume that the contact degradation happens at both cathode and anode and that it is the main reason of the capacity fading after the 30th cycle.

In order to investigate a possible dependence of SEI formation from the amount of $LiBH_4$ in the SSE, *i.e.* from the $LiBH_4$/MgO volume ratio, a similar cell was built using the **CE26** composite as electrolyte. **Figure 8.11** shows the GCPL profile of Li|**CE26**|TiS_2 at 60 °C, with a current density of 4.8 mA g^{-1} (corresponding to C/50).

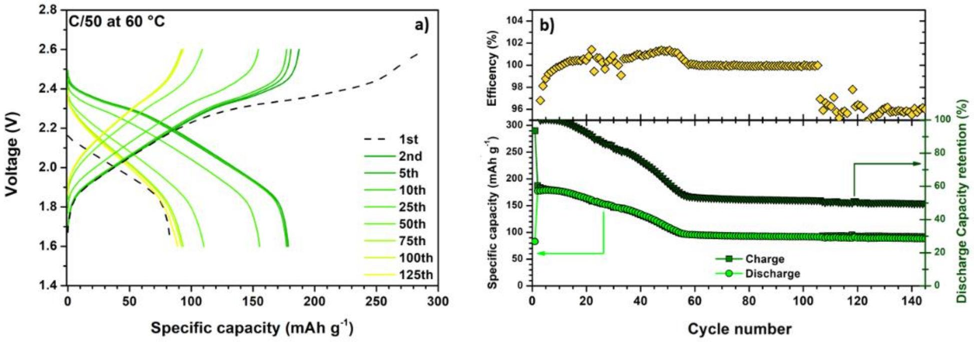

Figure 8.11. *a) Voltage profiles of Li|***CE26***|TiS$_2$ cell for a rate of C/50 (4.8 mA/g) at 60 °C. b) Discharge and charge capacity, Coulombic efficiency (discharge/charge capacity), and discharge capacity retention ratio (to the second discharge capacity) for the same cell.*

Also in this case, the capacity obtained on the second cycle (176 mA h g^{-1}) is higher compared than observed for the fist one (82 mA h g^{-1}), confirming the occurrence of a self-discharge reaction, as described above. Interestingly, when comparing the properties of cells with **CE26** and **CE53** as SSE, the same behviour is observed, *i.e.* a stabilization of the capacity fading after a certain number of cycles. In this case, the change is observed at the 58th cycle, a time-shift that can likely be due to the slower kinetcs imposed by a lower current rates (C/50 instead of C/20).

The high Li-ion conductivity of the **CE53** composite and the formation of a SEI at high temperature allow the battery to operate at R*T*. Therefore, after 65 cycles performed at 60 °C, the temperature of test for the Li|**CE53**|TiS$_2$ cell was decreased to R*T*. 4 hours rest have been applied in order to equilibrate the temperature. **Figure 8.12a** shows the galvanostatic profiles, using the same current density of 11.8 mA g^{-1} (C/20). For the sake of clarity, only selected galvanostatic profiles are shown. **Figure 8.12b** shows the discharge/charge capacity, Coulombic efficiency, and capacity retention ratio to the second discharge, as a function of cycle number.

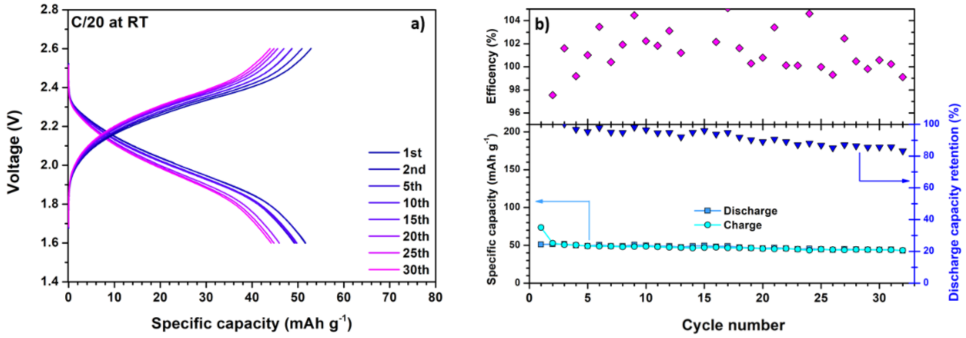

Figure 8.12. *a) Voltage profiles of Li|**CE53**|TiS_2 cell for a rate of C/20 at RT after 65 cycles at 60 °C at the C/20 rate. b) Discharge/Charge specific capacity, Coulombic efficiency (discharge capacity over charge capacity), and discharge capacity retention ratio (to the second discharge capacity) as a function of cycle number for the same cell.*

It is worth noting that the battery succesfully operates at R*T* for more than 30 cycles, with a discharge capacity retention of 80 %.

The capacity of Li|**CE26**|TiS_2 cell at R*T* for the first cycle is 51 mA h g^{-1} (**Figure 8.12**), to be compared with the value of 139 mA h g^{-1} obtained for the 65th cycle at 60 °C. In order to clarify this difference, **Figure 8.13** shows the voltage profiles of the 65th charge and discharge cycle shown in **Figure 8.9** compared with those corresponding to the 1st cycle at R*T* (**Figure 8.12**).

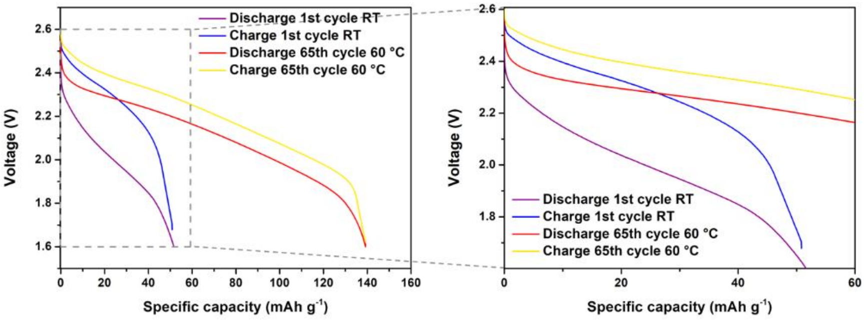

Figure 8.13. *Voltage profiles of the 65th charge and discharge cycle of Li|CE26|TiS_2 cell working at 60 °C and the 1st charge and discharge cycle of Li|CE26|TiS_2 cell working at RT.*

It is clear that decreasing of the working temperature causes an increase of the cell polarization, indicating that the capacity drop (*i.e.* between the last cycle at 60 °C and the fist at R*T*) can be assigned to kinetic limitations due to the low temperature. During the 4 hours rest, the evolution of the cell resistance was monitored by means of *in situ* EIS (**Figure 8.14a**).

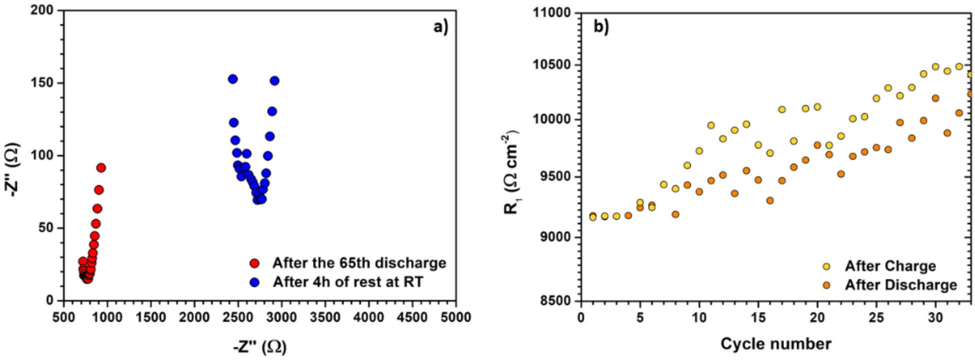

Figure 8.14. *a) Nyquist plot of Li|CE53|TiS$_2$ cell after the 65th discharge (red circles) and after 4 h of rest at RT (blue circles). b) Contact resistance (R$_1$) evolution obtained by in situ EIS for the same cell at RT, plotted in logarithmic scale.*

The increase of the cell resistance during the 4 hours rest at R*T* is mainly related to the decrease of the ionic conductivity of SSE. **Figure 8.14b** shows the contact resistance (R_1) after each charge discharge cycle at R*T*. Assuming that the formation of the SEI was completed during the first cycles at 60 °C, the steady increase of R_1 can be assigned to just a continuous contact loss, as observed also after the 30th cycle at 60 °C (**Figure 8.10b**). Despite this, **CE53** allowed to operate the Li|**CE53**|TiS$_2$ system at R*T*, once the SEI was formed.

Comparing the behaviour of the battery previously conditioned at 60 °C with respect to that operating directly at R*T* (**Figure 8.8**), it is evident that the high temperature treatment stabilises the interface, *i.e.* forming the $Li_2B_{12}H_{12}$-based SEI, allowing the cell to operate at R*T*. The longer life cycle suggests the prevention electrolyte decomposition.

As mentioned above, Unemoto *et al.*[47] reported results on a SSB very similar to that investigated in the present study, but using pure $LiBH_4$ instead of a composite as solid state electrolyte and operating at 120 °C, since h-$LiBH_4$ was necessary to achieve the high Li-ion conductivity. The obtained capacity retention was 88 % after 300 cycles at a C/5 rate. It has been reported that the higher working temperature increses the Li diffusion,[170,171] strongly limiting the voids formation at the electrode interface during the stripping process. This effect limits the contact resistance evolution, significantly reducing the capacity fading, as observed by Unemoto *et al.*[47] even in absence of an appropriate stack pressure, unlike the here reported case at 60 °C. In contrast, the results here reported, show that a drastical decrease of the operating temperature (*i.e.* from 120 °C to R*T*) is possible thanks to a $LiBH_4$-MgO nanocomposite as solid electrolyte and the formation, at 60 °C, of a stable SEI. It is the first time that the formation of a stable SEI at a temperature (60 °C) higher than the operating one (R*T*) is applied to a hydride solid-electrolyte and it is probably relevant also for other SSE working in full solid-state Li-ion batteries, as already reported by Rodrigues *et al.*[172].

Clearly, optimization of the battery, to realize a long cycle-life SSB, would lead to a different electrode choice. For instance, elemental sulfur, which has high theoretical capacity (1672 mA h g^{-1})[173] and a redox potential of ~2.2 V, similar to the oxidative limit of $LiBH_4$ electrochemical window (*i.e.* 2.2 V *vs.* Li^+/Li), would be a suitable electrode, possibly adopting infiltration procedure for the electrode preparation, *i.e.* dissolving the SSE in an opportune solvent and crystallizing it directly on the cathode material.[174,175] In addition, the optimization of the external cell stack pressure, recently suggested to be rather small (*i.e.* 5 MPa)[176], would reduce the contact resistance, leading to a lower capacity fading.[159,170]

Finally, the cost of solid electrolyte materials is important, as well as effective large scale production. The U.S. Department of Energy’s Advanced Research Projects Agency–Energy (ARPA-E) has adopted an ambitious target of 10 $/m^2 for the cost area of solid electrolyte materials,[177,178] considering a 10 μm thickness. The SSE synthetized in this work is composed by easily available raw material making the cost less than 2 $/g, corresponding to about 80 $/m^2. Considering that the up-scaling might decrease the cost, $LiBH_4$-based composites could be considered as competitive candidates to be used in a Li-ion SSBs.

8.3. Conclusions

In this work, solid-state fast ionic conductors, based on $LiBH_4$-MgO system, were investigated. The samples were mechanochemically synthetized. The Li-ion conductivity of $LiBH_4$ was improved in all cases and the samples containing 53 v/v % of MgO showed the best enhancement (2.86×10^{-4} S cm^{-1} at 20 °C), since the volume fraction of $LiBH_4$ allowed to completely fill the pore volume of MgO. The formation of a highly conductive layer does not affect the electrochemical stability window, which is similar to that of pure $LiBH_4$ (*i.e.* about 2.2 V *vs.* Li^+/Li).

A test at room termperature in a TiS_2/Li SSB allowed only 5 cycles before the cell failure. From a battery test at 60 °C, the incorporation of the solid electrolyte in the battery showed that a stable SEI is formed during the first charge/discharge cycles, causing an initial increase in contact resistance, but limiting a further decomposition of the composite electrolyte. Afterwards, the battery worked at room temperature for up to 30 cycles, with a specific capacity of about 50 mA h g^{-1}.

In conclusion, it has been demonstrated that the SEI, formed at 60 °C, allowed to reduce the operating temperature of the SSB down to R*T*. Therefore, a possible novel strategy to obtain a SSB working at room temperature, using complex hydrides as electrolyte, can be established by the formation of a stable SEI at higher temperatures. Despite this proof-of-concept, further optimization is mandatory to obtain an efficient battery (*e.g.* electrode choice and casting, cell stack pressure).

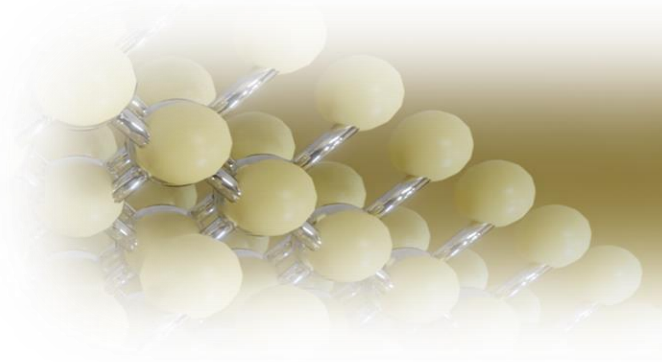

Chapter 9.

Conclusions and Outlook

The contribution of this thesis to the project was to search, characterize and provide a suitable $LiBH_4$-based ion-conductor as solid electrolyte for all-solid-state secondary batteries. In the last 10 years, the interest on complex hydrides as SSEs increased, thanks to strong research efforts and their interesting proprieties. Considering only materials properties, these compounds exhibit a particularly promising combination of high ionic conductivity, high thermal, chemical and electrochemical stability as well as favourable mechanical properties in view of device integration.[9,179,180] However, research gaps remain to be filled, such as studies on device integration are still at an early stage, when compared to more established materials classes.

The studies performed during this PhD project were carried out at the Department of Chemistry of the University of Turin, under the supervision of Prof. Marcello Baricco, aimed to explore different approaches to increase the R*T* Li-ion conductivity of the complex hydrides. This thesis involved structural and electrochemistry methods to characterize and provide a suitable ion-conductor as solid electrolyte for all-solid-state Li-ion batteries.

$LiBH_4$ has been selected as based material, since it is the more widely studied complex hydride as SSE,[9,46] but still gaps on the optimization of the Li-ion conductivity are present. Other complex hydrides, such as closoborates, have recently demonstrate interesting proprieties as SSE, but still the material cost is an issue,[9] and the structural proprieties of this materials are not completely understood.[9,23,180,181]

The starting point of this thesis was a statistical analysis of the literature EIS measurements of $LiBH_4$, in order to obtain the average values for the activation energy, ln σ_0 and Li-ion conductivity at 30 °C, that have been used as a reference in this work. The calculation of energies involved in the Li ion movement of the orthorhombic $LiBH_4$ were compared with the average values obtained from the statistical analysis, reaching an appreciable agreement. In addition, the correlation between the experimental and calculated values for Li-ion mobility has been evidenced also for $LiNH_2$ and Li_2NH complex hydrides, suggesting that the used topological analysis can adequately predict the ion conductivity in complex hydrides.

Anion modification, *e.g.* halogenation, represented the strategy to stabilize at R*T* the high temperature phase of the $LiBH_4$, but the phase diagram of most of the binary system reported in literature are still to be defined. Therefore, the binary phase diagram $LiBH_4$-LiBr has been explored by means of PXD, *in situ* SR-PXD and DSC. The monophasic zone of the hexagonal $Li(BH_4)_{1-x}(Br)_x$ solid solution has been defined to be equal to $0.3 < x < 0.55$ at R*T*, that is the solubility limits of interest to study the Li-ion conductivity. The insertion of the Br^- in the hexagonal structure increases the thermal stability of the $LiBH_4$, since, up to 300 °C, a decomposition of the hexagonal solid solution occurs. In order to perform the assessment of the phase diagram, a value of the enthalpy of mixing has been determined. The combination of calorimetric analysis and PXD, allowed to define a ΔH_{Mix} used to describe the $LiBH_4$-LiBr binary system in all composition and temperature range, considering the liquid phase as an ideal solution.

The hexagonal phase can be successfully stabilized at R*T* by the heavy Br^- and I^- anions, while the use of the lighter Cl^- would be preferred. For this reason, in order to reduce the mass of the electrolyte, *i.e.* increase the energy density of the battery, the miscibility of the LiCl in the studied $LiBH_4$-LiBr system has been investigated. The $LiBH_4$-LiBr-LiCl ternary phase diagram has been defined at *RT*, combining PXD data, coupled with a Rietveld refinement and a mass balance. The definition of the ternary phase diagram in the whole range of temperature and composition is an ongoing study. Then, the effect of the composition of the h-$Li(BH_4)_{1-\alpha-\beta}(Br)_\alpha(Cl)_\beta$ solid solution on the Li-ion conductivity has been investigated as a function of temperature using EIS. The h-$Li(BH_4)_{0.7}(Br)_{0.2}(Cl)_{0.1}$ sample showed the highest value of ion conductivity in the ternary solid solution at 30 °C (1.3×10^{-5} S cm^{-1}), offering a 10 % gain in weight, with no losses in ionic conductivity, with respect the binary solid solution with Br. The chloride anion substitution in the hexagonal structure increases the activation energy, but does not affect the Li-ion conductivity. Even though such an effect can be explained in terms of lattice stiffening, it is still debated the effect of anions dynamics on the Li-ion conductivity in complex hydrides. Finally, the amount of halide anions on the electrochemical stability of the hexagonal solid solution shows that $Li(BH_4)_{0.7}Br_{0.3}$ offers the best electrochemical results.

The second approach to increase the RT conductivity of the $LiBH_4$ used in this thesis is the formation of mixtures of $LiBH_4$ with oxides. The effect of adding various oxides on the solid-state ion conductivity of $LiBH_4$ has been reported and all oxides investigated greatly enhanced the ionic conductivity. Results on $LiBH_4$-SiO_2 composites had been already reported before, but few guidelines to reach maximum conductivity in these composites have been presented, *e.g.* the volume of $LiBH_4$ in the composite should roughly correspond to the pore volume of the oxide. Novel interesting SSE $LiBH_4$-oxide-based have been synthetized in this work. The highest conductivities, *i.e.* 2.6×10^{-4} and 1.8×10^{-4} S cm^{-1} at 40 °C, were observed for composites with ZrO_2 and MgO, respectively, and the optimization of the composition in this system can even increase the Li-ion conductivity of the composite.

Since the two different approaches to increase the Li-ion conductivity of the $LiBH_4$, presented showed successfully results, the possibility of a synergic effect between them has been investigated. Firstly, the effect of the halide content has been analyze inside the solubility limits of the h-$Li(BH_4)_{1-\alpha}(X)_\alpha$ for the system $LiBH_4$-LiI and again for $LiBH_4$-LiBr. Once the more conductive h-$Li(BH_4)_{1-\alpha}(X)_\alpha$ solid solution in each system was individuated, the effect of adding SiO_2 has been analyzed. When the hexagonal solid solution completely fills the pore of the oxide, an increase of the h-$Li(BH_4)_{1-\alpha}(X)_\alpha$ Li-ion conductivity has been highlighted, so the guideline to optimize the composite composition, proposed previously in this work, has been confirmed. A synergetic effect between these two approaches, *i.e.* halogenation and interface engineering, has therefore been highlighted in this study, indicating a promising insight to synthetized novel solid-state electrolytes.

Finally, after the selection of a promising SSE synthetized during the PhD project, the incorporation of a $LiBH_4$-base SSE in a solid-state Li-ion battery was studied. Among them, solid-state fast ionic conduction, based on $LiBH_4$-MgO system, were selected. After an optimization of the $LiBH_4$-MgO composition, the samples containing 53 v/v % of MgO showed the best enhancement (2.86×10^{-4} S cm^{-1} at 20 °C), since the volume fraction of $LiBH_4$ allowed to completely fill the pore volume of MgO. This fast ion conductor possesses an electrochemical stability window of about 2.2 V *vs.* Li^+/Li, which is similar to that of pure $LiBH_4$. The incorporation of the solid-state electrolyte in a TiS_2/Li SSB allowed only 5 cycles before the cell failure at R*T*. However, it has been demonstrated that a solid electrode interface, formed at higher temperature (60 °C), allowed to cycle the SSB at R*T*, with a nearly stable capacity and a rather small fading. Therefore, a possible novel strategy to obtain a SSB working at room temperature, using complex hydrides as electrolyte, has been established by the formation of a stable SEI at higher temperatures. Despite this proof-of-concept, further optimization is mandatory to obtain an efficient battery.

In view of the results achieved, hopefully, this work could suggest some new discoveries or further successful investigation in the development of $LiBH_4$-based ion-conductors. The proficient results from this PhD project have been possible thanks to a wide scientific network and different international collaborators, especially Prof. Petra de Jongh and Dr. Peter Ngene form the University of Utrecht and Radovan Cerny, Dr. Matteo Brighi and Dr. Fabrizio Murgia form the University of Geneva. It must be underlined how much these international collaborations were important to further enlarge the knowledge on these topics.

Some analysis result still incomplete, but promising novel ion conductors, characterized as solid electrolyte were presented and, maybe, they could represent a starting point for new developments in solid-state batteries field.

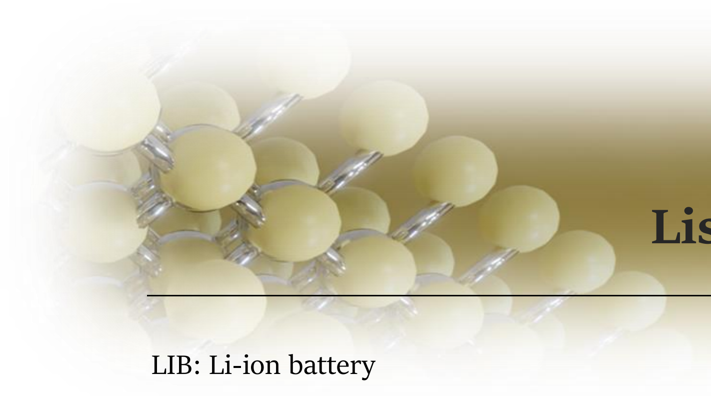

List of Abbreviations

LIB: Li-ion battery

SSB: all-solid-state battery

SSE: solid-state electrolyte

E_A: Activation energy

E_m: Energy of migration

E_f: Energy of defect formation

s.g.: space group

BM: ball milling

HP-DSC: High Pressure Difference Scanning Calorimetric

ATR-IR: Attenuated Total Reflection-Infrared Spectroscopy

EIS: Electrochemical Impedance Spectroscopy

CV: Cyclic Voltammetry

GCPL: Galvanostatic Cycling with Potential Limitation (ATR-IR)

CB: Carbon Black

C_p: heat capacity at constant pressure or volume

DFT: Density Function Theory

DSC: Differential Scanning Calorimeter

PXD: Powder X-ray Diffraction

RT: room temperature

SR: Synchrotron Radiation

SS: stainless steel

WC: tungsten carbide

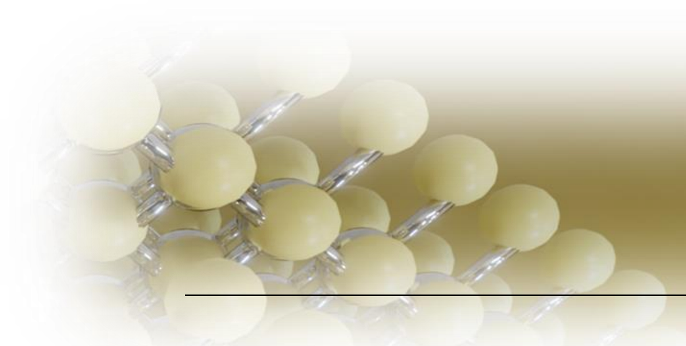

References

(1) Zuttel, A.; Remhof, A.; Borgschulte, A.; Friedrichs, O. Hydrogen: The Future Energy Carrier. *Philos. Trans. R. Soc. A Math. Phys. Eng. Sci.* **2010**, *368* (1923), 3329–3342. https://doi.org/10.1098/rsta.2010.0113.

(2) Armaroli, N.; Balzani, V. The Future of Energy Supply: Challenges and Opportunities. *Angew. Chemie Int. Ed.* **2007**, *46* (1–2), 52–66. https://doi.org/10.1002/anie.200602373.

(3) World Economic Forum; Global Battery Alliance. *A Vision for a Sustainable Battery Value Chain in 2030*; 2019.

(4) Zubi, G.; Dufo-López, R.; Carvalho, M.; Pasaoglu, G. The Lithium-Ion Battery: State of the Art and Future Perspectives. *Renew. Sustain. Energy Rev.* **2018**, *89* (March), 292–308. https://doi.org/10.1016/j.rser.2018.03.002.

(5) Xu, K. Nonaqueous Liquid Electrolytes for Lithium-Based Rechargeable Batteries. *Chem. Rev.* **2004**, *104* (10), 4303–4417. https://doi.org/10.1021/cr030203g.

(6) Xu, W.; Wang, J.; Ding, F.; Chen, X.; Nasybulin, E.; Zhang, Y.; Zhang, J.-G. Lithium Metal Anodes for Rechargeable Batteries. *Energy Environ. Sci.* **2014**, *7* (2), 513–537. https://doi.org/10.1039/C3EE40795K.

(7) Goodenough, J. B.; Park, K. The Li-Ion Rechargeable Battery: A Perspective. *J. Am. Chem. Soc.* **2013**, *135* (4), 1167–1176. https://doi.org/10.1021/ja3091438.

(8) Goodenough, J. B.; Kim, Y. Challenges for Rechargeable Li Batteries †. *Chem. Mater.* **2010**, *22* (3), 587–603. https://doi.org/10.1021/cm901452z.

(9) Duchêne, L.; Remhof, A.; Hagemann, H.; Battaglia, C. Status and Prospects of Hydroborate Electrolytes for All-Solid-State Batteries. *Energy Storage Mater.* **2019**, No. May. https://doi.org/10.1016/j.ensm.2019.08.032.

(10) Culver, S. P.; Koerver, R.; Krauskopf, T.; Zeier, W. G. Designing Ionic Conductors: The Interplay between Structural Phenomena and Interfaces in Thiophosphate-Based Solid-State Batteries. *Chem. Mater.* **2018**, *30* (13), 4179–4192. https://doi.org/10.1021/acs.chemmater.8b01293.

(11) Jansen, M. Volume Effect or Paddle-Wheel Mechanism—Fast Alkali-Metal Ionic Conduction in Solids with Rotationally Disordered Complex Anions. *Angew. Chemie Int. Ed. English* **1991**, *30* (12), 1547–1558. https://doi.org/10.1002/anie.199115471.

(12) C.Kittel. *Introduction to Solid State Physics*; Wiley, Ed.; 2005.

(13) Goodenough, J. B. Oxide-Ion Electrolytes. *Annu. Rev. Mater. Res.* **2003**, *33* (1), 91–128. https://doi.org/10.1146/annurev.matsci.33.022802.091651.

(14) Habasaki, J.; Leon, C.; Ngai, K. L. *Dynamics of Glassy, Crystalline and Liquid Ionic Conductors*; Springer, Ed.; Topics in Applied Physics; Springer International Publishing: Cham, 2017; Vol. 132. https://doi.org/10.1007/978-3-319-42391-3.

(15) Liu, X.; Majzoub, E. H.; Stavila, V.; Bhakta, R. K.; Allendorf, M. D.; Shane, D. T.; Conradi, M. S.; Verdal, N.; Udovic, T. J.; Hwang, S.-J. Probing the Unusual Anion Mobility of $LiBH_4$ Confined in Highly Ordered Nanoporous Carbon Frameworks via Solid State NMR and Quasielastic Neutron Scattering. *J. Mater. Chem. A* **2013**, *1*

(34), 9935. https://doi.org/10.1039/c3ta12051a.

(16) Stramare, S.; Thangadurai, V.; Weppner, W. Lithium Lanthanum Titanates: A Review. *Chem. Mater.* **2003**, *15* (21), 3974–3990. https://doi.org/10.1021/cm0300516.

(17) Inaguma, Y.; Liquan, C.; Itoh, M.; Nakamura, T.; Uchida, T.; Ikuta, H.; Wakihara, M. High Ionic Conductivity in Lithium Lanthanum Titanate. *Solid State Commun.* **1993**, *86* (10), 689–693. https://doi.org/10.1016/0038-1098(93)90841-A.

(18) Tan, J.; Tiwari, A. LLZO Synthesis of Cubic Phase Li7La3Zr2O12 Electrolyte for Solid-State Lithium-Ion Batteries. *Electrochem. Solid-State Lett.* **2012**, *15* (3), A37. https://doi.org/10.1149/2.003203esl.

(19) Sanjuán, M. L.; Laguna, M. A.; Belous, A. G.; V'yunov, O. I. On the Local Structure and Lithium Dynamics of $La_{0.5}(Li,Na)_{0.5}TiO_3$ Ionic Conductors. A Raman Study. *Chem. Mater.* **2005**, *17* (23), 5862–5866. https://doi.org/10.1021/cm0517770.

(20) Manthiram, A.; Yu, X.; Wang, S. Lithium Battery Chemistries Enabled by Solid-State Electrolytes. *Nat. Rev. Mater.* **2017**, *2* (4), 16103. https://doi.org/10.1038/natrevmats.2016.103.

(21) Krauskopf, T.; Culver, S. P.; Zeier, W. G. Bottleneck of Diffusion and Inductive Effects in $Li_{10}Ge_{1-x}Sn_xP_2S_{12}$. *Chem. Mater.* **2018**, *30* (5), 1791–1798. https://doi.org/10.1021/acs.chemmater.8b00266.

(22) Sakuda, A.; Hayashi, A.; Tatsumisago, M. Sulfide Solid Electrolyte with Favorable Mechanical Property for All-Solid-State Lithium Battery. *Sci. Rep.* **2013**, *3* (1), 2261. https://doi.org/10.1038/srep02261.

(23) Kim, S.; Oguchi, H.; Toyama, N.; Sato, T.; Takagi, S.; Otomo, T.; Arunkumar, D.; Kuwata, N.; Kawamura, J.; Orimo, S. A Complex Hydride Lithium Superionic Conductor for High-Energy-Density All-Solid-State Lithium Metal Batteries. *Nat. Commun.* **2019**, *10* (1), 1081. https://doi.org/10.1038/s41467-019-09061-9.

(24) Schlesinger, H. I.; Brown, H. C. Metallo Borohydrides. III. Lithium Borohydride. *J. Am. Chem. Soc.* **1940**, *62* (12), 3429–3435. https://doi.org/10.1021/ja01869a039.

(25) El Kharbachi, A.; Pinatel, E.; Nuta, I.; Baricco, M. A Thermodynamic Assessment of $LiBH_4$. *Calphad* **2012**, *39*, 80–90. https://doi.org/10.1016/j.calphad.2012.08.005.

(26) Soulie, J.; Renaudin, G.; Černý, R.; Yvon, K. Lithium Boro-Hydride $LiBH_4$ I. Crystal Structure. *J. Alloys Compd.* **2002**, *346*, 200–205. https://doi.org/https://doi.org/10.1016/S0925-8388(02)00521-2.

(27) Matsuo, M.; Orimo, S. Lithium Fast-Ionic Conduction in Complex Hydrides: Review and Prospects. *Adv. Energy Mater.* **2011**, *1* (2), 161–172. https://doi.org/10.1002/aenm.201000012.

(28) Matsuo, M.; Nakamori, Y.; Orimo, S.; Maekawa, H.; Takamura, H. Lithium Superionic Conduction in Lithium Borohydride Accompanied by Structural Transition. *Appl. Phys. Lett.* **2007**, *91* (22), 224103. https://doi.org/10.1063/1.2817934.

(29) Ikeshoji, T.; Tsuchida, E.; Morishita, T.; Ikeda, K.; Matsuo, M.; Kawazoe, Y.; Orimo, S. Fast-Ionic Conductivity of Li^+ in $LiBH_4$. *Phys. Rev. B* **2011**, *83* (14), 144301. https://doi.org/10.1103/PhysRevB.83.144301.

(30) Lee, Y.-S.; Cho, Y. W. Fast Lithium Ion Migration in Room Temperature LiBH 4. *J. Phys. Chem. C* **2017**, *121* (33), 17773–17779. https://doi.org/10.1021/acs.jpcc.7b06328.

(31) Buchter, F.; Łodziana, Z.; Mauron, P.; Remhof, A.; Friedrichs, O.; Borgschulte, A.; Züttel, A.; Sheptyakov, D.; Strässle, T.; Ramirez-Cuesta, A. J. Dynamical Properties and Temperature Induced Molecular Disordering of $LiBH_4$ and $LiBD_4$. *Phys. Rev. B* **2008**, *78* (9), 094302. https://doi.org/10.1103/PhysRevB.78.094302.

(32) Martelli, P.; Remhof, A.; Borgschulte, A.; Ackermann, R.; Strässle, T.; Embs, J. P.; Ernst, M.; Matsuo, M.; Orimo, S.-I.; Züttel, A. Rotational Motion in $LiBH_4$/LiI Solid Solutions. *J. Phys. Chem. A* **2011**, *115* (21), 5329–5334. https://doi.org/10.1021/jp201372b.

(33) Wolczyk, A.; Pinatel, E. R.; Chierotti, M. R.; Nervi, C.; Gobetto, R.; Baricco, M. Solid-State NMR and Thermodynamic Investigations on $LiBH_4LiNH_2$ System. *Int. J. Hydrogen Energy* **2016**, *41* (32), 14475–14483. https://doi.org/10.1016/j.ijhydene.2016.03.040.

(34) Davies, R. A.; Hewett, D. R.; Anderson, P. A. Enhancing Ionic Conductivity in Lithium Amide for Improved Energy Storage Materials. *Adv. Nat. Sci. Nanosci. Nanotechnol.* **2014**, *6* (1), 015005. https://doi.org/10.1088/2043-6262/6/1/015005.

(35) Matsuo, M.; Remhof, A.; Martelli, P.; Caputo, R.; Ernst, M.; Miura, Y.; Sato, T.; Oguchi, H.; Maekawa, H.; Takamura, H.; Borgschulte, A.; Züttel, A.; Orimo, S. Complex Hydrides with $(BH_4)^-$ and $(NH_2)^-$ Anions as New Lithium Fast-Ion Conductors. *J. Am. Chem. Soc.* **2009**, *131* (45), 16389–16391. https://doi.org/10.1021/ja907249p.

(36) Paskevicius, M.; Jepsen, L. H.; Schouwink, P.; Černý, R.; Ravnsbæk, D. B.; Filinchuk, Y.; Dornheim, M.; Besenbacher, F.; Jensen, T. R. Metal Borohydrides and Derivatives – Synthesis, Structure and Properties. *Chem. Soc. Rev.* **2017**, *46* (5), 1565–1634. https://doi.org/10.1039/C6CS00705H.

(37) C, D.; Myrdal, J. S. G.; Blanchard, D.; Bentzen, J. J.; Hirata, T.; Mogensen, M. B.; Norby, P.; Orimo, S.; Vegge, T. Effect of Heat Treatment on the Lithium Ion Conduction of the $LiBH_4$–LiI Solid Solution. *J. Phys. Chem. C* **2013**, *117* (7), 3249–3257. https://doi.org/10.1021/jp310050g.

(38) I, R. M.; Karahashi, T.; Kumatani, N.; Noda, Y.; Ando, M.; Takamura, H.; Matsuo, M.; Orimo, S.; Maekawa, H. Room Temperature Lithium Fast-Ion Conduction and Phase Relationship of LiI Stabilized $LiBH_4$. *Solid State Ionics* **2011**, *192* (1), 143–147. https://doi.org/10.1016/j.ssi.2010.05.017.

(39) Cascallana-Matias, I.; Keen, D. A.; Cussen, E. J.; Gregory, D. H. Phase Behavior in the $LiBH_4$–LiBr System and Structure of the Anion-Stabilized Fast Ionic, High Temperature Phase. *Chem. Mater.* **2015**, *27* (22), 7780–7787. https://doi.org/10.1021/acs.chemmater.5b03642.

(40) Zhou, Y.; Matsuo, M.; Miura, Y.; Takamura, H.; Maekawa, H.; Remhof, A.; Borgschulte, A.; Zuttel, A.; Otomo, T.; Orimo, S. Enhanced Electrical Conductivities of Complex Hydrides $Li_2(BH_4)(NH_2)$ and $Li_4(BH_4)(NH_2)_3$ by Melting. *Mater. Trans.* **2011**, *52* (4), 654–657. https://doi.org/10.2320/matertrans.MA201003.

(41) Wolczyk, A.; Paik, B.; Sato, T.; Nervi, C.; Brighi, M.; GharibDoust, S. P.; Chierotti, M.; Matsuo, M.; Li, G.; Gobetto, R.; Jensen, T. R.; Černý, R.; Orimo, S.; Baricco, M. $Li_5(BH_4)_3NH$: Lithium-Rich Mixed Anion Complex Hydride. *J. Phys. Chem. C* **2017**, *121* (21), 11069–11075. https://doi.org/10.1021/acs.jpcc.7b00821.

(42) Choi, Y. S.; Lee, Y.-S.; Oh, K. H.; Cho, Y. W. Interface-Enhanced Li Ion Conduction

in a $LiBH_4$–SiO_2 Solid Electrolyte. *Phys. Chem. Chem. Phys.* **2016**, *18* (32), 22540–22547. https://doi.org/10.1039/C6CP03563A.

(43) Choi, Y. S.; Lee, Y.-S.; Choi, D.-J.; Chae, K. H.; Oh, K. H.; Cho, Y. W. Enhanced Li Ion Conductivity in $LiBH_4$–Al_2O_3 Mixture via Interface Engineering. *J. Phys. Chem. C* **2017**, *121* (47), 26209–26215. https://doi.org/10.1021/acs.jpcc.7b08862.

(44) Lefevr, J.; Cervini, L.; Griffin, J. M.; Blanchard, D. Lithium Conductivity and Ions Dynamics in $LiBH_4$/SiO_2 Solid Electrolytes Studied by Solid-State NMR and Quasi-Elastic Neutron Scattering and Applied in Lithium–Sulfur Batteries. *J. Phys. Chem. C* **2018**, *122* (27), 15264–15275. https://doi.org/10.1021/acs.jpcc.8b01507.

(45) Blanchard, D.; Nale, A.; Sveinbjörnsson, D.; Eggenhuisen, T. M.; Verkuijlen, M. H. W.; Suwarno; Vegge, T.; Kentgens, A. P. M.; de Jongh, P. E. Nanoconfined $LiBH_4$ as a Fast Lithium Ion Conductor. *Adv. Funct. Mater.* **2015**, *25* (2), 184–192. https://doi.org/10.1002/adfm.201402538.

(46) Latroche, M.; Blanchard, D.; Cuevas, F.; El Kharbachi, A.; Hauback, B. C.; Jensen, T. R.; de Jongh, P. E.; Kim, S.; Nazer, N. S.; Ngene, P.; Orimo, S.; Ravnsbæk, D. B.; Yartys, V. A. Full-Cell Hydride-Based Solid-State Li Batteries for Energy Storage. *Int. J. Hydrogen Energy* **2019**, *44* (15), 7875–7887. https://doi.org/10.1016/j.ijhydene.2018.12.200.

(47) Unemoto, A.; Ikeshoji, T.; Yasaku, S.; Matsuo, M.; Stavila, V.; Udovic, T. J.; Orimo, S. Stable Interface Formation between TiS_2 and $LiBH_4$ in Bulk-Type All-Solid-State Lithium Batteries. *Chem. Mater.* **2015**, *27* (15), 5407–5416. https://doi.org/10.1021/acs.chemmater.5b02110.

(48) Unemoto, A.; Yasaku, S.; Nogami, G.; Tazawa, M.; Taniguchi, M.; Matsuo, M.; Ikeshoji, T.; Orimo, S. I. Development of Bulk-Type All-Solid-State Lithium-Sulfur Battery Using $LiBH_4$ electrolyte. *Appl. Phys. Lett.* **2014**, *105* (8), 103–107. https://doi.org/10.1063/1.4893666.

(49) Unemoto, A.; Wu, H.; Udovic, T. J.; Matsuo, M.; Ikeshoji, T.; Orimo, S. Fast Lithium-Ionic Conduction in a New Complex Hydride–Sulphide Crystalline Phase. *Chem. Commun.* **2016**, *52* (3), 564–566. https://doi.org/10.1039/C5CC07793A.

(50) Das, S.; Ngene, P.; Norby, P.; Vegge, T.; de Jongh, P. E.; Blanchard, D. All-Solid-State Lithium-Sulfur Battery Based on a Nanoconfined $LiBH_4$ Electrolyte. *J. Electrochem. Soc.* **2016**, *163* (9), A2029–A2034. https://doi.org/10.1149/2.0771609jes.

(51) Mal'tseva, N. N.; Generalova, N. B.; Masanov, A. Y.; Zhizhin, K. Y.; Kuznetsov, N. T. Mechanochemical Synthesis of Complex Hydrides. *Russ. J. Inorg. Chem.* **2012**, *57* (13), 1631–1652. https://doi.org/10.1134/S0036023612130049.

(52) Ravnsbæk, D. B.; Filinchuk, Y.; Cerný, R.; Jensen, T. R. Powder Diffraction Methods for Studies of Borohydride-Based Energy Storage Materials. *Zeitschrift für Krist.* **2010**, *225* (12), 557–569. https://doi.org/10.1524/zkri.2010.1357.

(53) Møller, K. T.; Hansen, B. R. S.; Dippel, A.-C.; Jørgensen, J.-E. E.; Jensen, T. R. Characterization of Gas-Solid Reactions Using In Situ Powder X-Ray Diffraction. *Zeitschrift für Anorg. und Allg. Chemie* **2014**, *640* (15), 3029–3043. https://doi.org/10.1002/zaac.201400262.

(54) Hammersley, A. P. FIT2D: An Introduction and Overview. *Eur. Synchrotron Radiat. Facil. Intern. Rep. ESRF97HA02T* **1997**, *68* (58).

(55) Hammersley, A. P.; Svensson, S. O.; Hanfland, M.; Fitch, A. N.; Hausermann, D.

Two-Dimensional Detector Software: From Real Detector to Idealised Image or Two-Theta Scan. *High Press. Res.* **1996**, *14* (4–6), 235–248. https://doi.org/10.1080/08957959608201408.

(56) Thompson, P.; Cox, D. E.; Hastings, J. B. Rietveld Refinement of Debye–Scherrer Synchrotron X-Ray Data from Al_2O_3. *J. Appl. Crystallogr.* **1987**, *20* (2), 79–83. https://doi.org/10.1107/S0021889887087090.

(57) Lutterotti, L., Matthies, S., Wenk, H. R. MAUD: A Friendly Java Program for Material Analysis Using Diffraction. *MAUD A Friendly Java Progr. Mater. Anal. Using Diffr.* **1999**, 14–15.

(58) Hans Leo Lukas, S. G. F. and B. S. *Computational Thermodynamics: The Calphad Method*; Cambridge University Press: Cambridge, 2007.

(59) Andersson, J. O.; Helander, T.; Hoglund, L.; Shi, P.; Sundman, B. THERMO-CALC & DICTRA, Computational Tools For Materials Science. *Calphad* **2002**, *26* (2), 273–312.

(60) Bölle, F. T.; Mathiesen, N. R.; Nielsen, A. J.; Vegge, T.; Garcia-Lastra, J. M.; Castelli, I. E. Autonomous Discovery of Materials for Intercalation Electrodes. *Batter. Supercaps* **2020**, *3* (6), 488–498. https://doi.org/10.1002/batt.201900152.

(61) Henkelman, G.; Uberuaga, B. P.; Jónsson, H. A Climbing Image Nudged Elastic Band Method for Finding Saddle Points and Minimum Energy Paths. *J. Chem. Phys.* **2000**, *113* (22), 9901–9904. https://doi.org/10.1063/1.1329672.

(62) Shi, S.; Gao, J.; Liu, Y.; Zhao, Y.; Wu, Q.; Ju, W.; Ouyang, C.; Xiao, R. Multi-Scale Computation Methods: Their Applications in Lithium-Ion Battery Research and Development. *Chinese Phys. B* **2016**, *25* (1), 018212. https://doi.org/10.1088/1674-1056/25/1/018212.

(63) Deng, Z.; Zhu, Z.; Chu, I.-H.; Ong, S. P. Data-Driven First-Principles Methods for the Study and Design of Alkali Superionic Conductors. *Chem. Mater.* **2017**, *29* (1), 281–288. https://doi.org/10.1021/acs.chemmater.6b02648.

(64) Xiao, R.; Li, H.; Chen, L. Candidate Structures for Inorganic Lithium Solid-State Electrolytes Identified by High-Throughput Bond-Valence Calculations. *J. Mater.* **2015**, *1* (4), 325–332. https://doi.org/10.1016/j.jmat.2015.08.001.

(65) Anurova, N. A.; Blatov, V. A.; Ilyushin, G. D.; Blatova, O. A.; Ivanov-Schitz, A. K.; Dem'yanets, L. N. Migration Maps of Li^+ cations in Oxygen-Containing Compounds. *Solid State Ionics* **2008**, *179* (39), 2248–2254. https://doi.org/10.1016/j.ssi.2008.08.001.

(66) Brighi, M.; Schouwink, P.; Sadikin, Y.; Černý, R. Fast Ion Conduction in Garnet-Type Metal Borohydrides $Li_3K_3Ce_2(BH_4)_{12}$ and $Li_3K_3La_2(BH_4)_{12}$. *J. Alloys Compd.* **2016**, *662*, 388–395. https://doi.org/10.1016/j.jallcom.2015.11.218.

(67) Kresse, G.; Furthmüller, J. Efficient Iterative Schemes for Ab Initio Total-Energy Calculations Using a Plane-Wave Basis Set. *Phys. Rev. B* **1996**, *54* (16), 11169–11186. https://doi.org/10.1103/PhysRevB.54.11169.

(68) Blatov, V. A.; Shevchenko, A. P.; Proserpio, D. M. Applied Topological Analysis of Crystal Structures with the Program Package ToposPro. *Cryst. Growth Des.* **2014**, *14* (7), 3576–3586. https://doi.org/10.1021/cg500498k.

(69) Van de Walle, C. G.; Neugebauer, J. First-Principles Calculations for Defects and Impurities: Applications to III-Nitrides. *J. Appl. Phys.* **2004**, *95* (8), 3851–3879. https://doi.org/10.1063/1.1682673.

(70) E. Barsoukov, J. R. M. *Impedance Spectroscopy: Theory, Experiment, and Applications*, Wiley and.; 2005.

(71) Duchêne, L. Thesis Development of a New Closo-Borate Solid Electrolyte and Its Implementation in All-Solid-State Batteries Laboratory Materials for Energy Conversion Development of a New Closo -Borate Solid Electrolyte and Its Implementation in All-Solid-State Batter, Université de Genève, 2019. https://doi.org/10.13097/archive-ouverte/unige:126129.

(72) Boukamp, B. A. Electrochemical Impedance Spectroscopy in Solid State Ionics: Recent Advances. *Solid State Ionics* **2004**, *169* (1–4), 65–73. https://doi.org/10.1016/j.ssi.2003.07.002.

(73) Boukamp, B. A. A Package for Impedance/Admittance Data Analysis. *Solid State Ionics* **1986**, *19*, 136–140.

(74) Agrawal, R. C. Dc Polarisation: An Experimental Tool in the Study of Ionic Conductors. *Indian J. Pure Appl. Phys.* **1999**, *37* (4), 294–301.

(75) Elgrishi, N.; Rountree, K. J.; McCarthy, B. D.; Rountree, E. S.; Eisenhart, T. T.; Dempsey, J. L. A Practical Beginner's Guide to Cyclic Voltammetry. *J. Chem. Educ.* **2018**, *95* (2), 197–206. https://doi.org/10.1021/acs.jchemed.7b00361.

(76) Nam, Y. J.; Park, K. H.; Oh, D. Y.; An, W. H.; Jung, Y. S. Diagnosis of Failure Modes for All-Solid-State Li-Ion Batteries Enabled by Three-Electrode Cells. *J. Mater. Chem. A* **2018**, *6* (30), 14867–14875. https://doi.org/10.1039/C8TA03450H.

(77) Gulino, V.; Brighi, M.; Dematteis, E. M.; Murgia, F.; Nervi, C.; Černý, R.; Baricco, M. Phase Stability and Fast Ion Conductivity in the Hexagonal $LiBH_4$–LiBr–LiCl Solid Solution. *Chem. Mater.* **2019**, *31* (14), 5133–5144. https://doi.org/10.1021/acs.chemmater.9b01035.

(78) Asakura, R.; Duchêne, L.; Kühnel, R.-S.; Remhof, A.; Hagemann, H.; Battaglia, C. Electrochemical Oxidative Stability of Hydroborate-Based Solid-State Electrolytes. *ACS Appl. Energy Mater.* **2019**, *2* (9), 6924–6930. https://doi.org/10.1021/acsaem.9b01487.

(79) Han, F.; Zhu, Y.; He, X.; Mo, Y.; Wang, C. Electrochemical Stability of $Li_{10}GeP_2S_{12}$ and $Li_7La_3Zr_2O_{12}$ Solid Electrolytes. **2016**, 1–9. https://doi.org/10.1002/aenm.201501590.

(80) Kim, G.-T.; Appetecchi, G. B.; Montanino, M.; Alessandrini, F.; Passerini, S. Long-Term Cyclability of Lithium Metal Electrodes in Ionic Liquid-Based Electrolytes at Room Temperature. *ECS Trans.* **2019**, *25* (36), 127–138. https://doi.org/10.1149/1.3393847.

(81) Ikeshoji, T.; Tsuchida, E.; Ikeda, K.; Matsuo, M.; Li, H. Diffuse and Doubly Split Atom Occupation in Hexagonal $LiBH_4$ Diffuse and Doubly Split Atom Occupation in Hexagonal $LiBH_4$. **2009**, No. May 2014, 4–7. https://doi.org/10.1063/1.3264953.

(82) Matsuo, M.; Takamura, H.; Maekawa, H.; Li, H.-W.; Orimo, S. Stabilization of Lithium Superionic Conduction Phase and Enhancement of Conductivity of $LiBH_4$ by LiCl Addition. *Appl. Phys. Lett.* **2009**, *94* (8), 084103. https://doi.org/10.1063/1.3088857.

(83) Sveinbjörnsson, D.; Blanchard, D.; Myrdal, J. S. G.; Younesi, R.; Viskinde, R.; Riktor, M. D.; Norby, P.; Vegge, T. Ionic Conductivity and the Formation of Cubic CaH2 in the $LiBH_4$–$Ca(BH_4)_2$ Composite. *J. Solid State Chem.* **2014**, *211*, 81–89. https://doi.org/10.1016/j.jssc.2013.12.006.

(84) Gulino, V.; Barberis, L.; Ngene, P.; Baricco, M.; de Jongh, P. E. Enhancing Li-Ion Conductivity in $LiBH_4$-Based Solid Electrolytes by Adding Various Nanosized Oxides. *ACS Appl. Energy Mater.* **2020**, *3* (5), 4941–4948. https://doi.org/10.1021/acsaem.9b02268.

(85) Hoang, K.; Janotti, A.; Van De Walle, C. G. The Particle-Size Dependence of the Activation Energy for Decomposition of Lithium Amide. *Angew. Chemie - Int. Ed.* **2011**, *50* (43), 10170–10173. https://doi.org/10.1002/anie.201100810.

(86) Hazrati, E.; Brocks, G.; Buurman, B.; De Groot, R. A.; De Wijs, G. A. Intrinsic Defects and Dopants in $LiNH_2$: A First-Principles Study. *Phys. Chem. Chem. Phys.* **2011**, *13* (13), 6043–6052. https://doi.org/10.1039/c0cp01540g.

(87) Wang, J.; Du, Y.; Xu, H.; Jiang, C.; Kong, Y.; Sun, L.; Liu, Z. K. Native Defects in $LiNH_2$: A First-Principles Study. *Phys. Rev. B - Condens. Matter Mater. Phys.* **2011**, *84* (2), 21–24. https://doi.org/10.1103/PhysRevB.84.024107.

(88) Miceli, G.; Cucinotta, C. S.; Bernasconi, M.; Parrinello, M. First Principles Study of the $LiNH_2/Li_2NH$ Transformation. *J. Phys. Chem. C* **2010**, *114* (35), 15174–15183. https://doi.org/10.1021/jp100723p.

(89) Li, W.; Wu, G.; Xiong, Z.; Feng, Y. P.; Chen, P. Li^+ Ionic Conductivities and Diffusion Mechanisms in Li-Based Imides and Lithium Amide. *Phys. Chem. Chem. Phys.* **2012**, *14* (5), 1596–1606. https://doi.org/10.1039/C2CP23636B.

(90) Hoang, K.; Van De Walle, C. G. Mechanism for the Decomposition of Lithium Borohydride. *Int. J. Hydrogen Energy* **2012**, *37* (7), 5825–5832. https://doi.org/10.1016/j.ijhydene.2012.01.002.

(91) Dematteis, E. M.; Jensen, S. R.; Jensen, T. R.; Baricco, M. Heat Capacity and Thermodynamic Properties of Alkali and Alkali-Earth Borohydrides. *J. Chem. Thermodyn.* **2020**, *143*, 106055. https://doi.org/10.1016/j.jct.2020.106055.

(92) Dematteis, E. M.; Roedern, E.; Pinatel, E. R.; Corno, M.; Jensen, T. R.; Baricco, M. A Thermodynamic Investigation of the $LiBH_4$–$NaBH_4$ System. *RSC Adv.* **2016**, *6* (65), 60101–60108. https://doi.org/10.1039/C6RA09301A.

(93) Dematteis, E. M.; Pinatel, E. R.; Corno, M.; Jensen, T. R.; Baricco, M. Phase Diagrams of the $LiBH_4$–$NaBH_4$–KBH_4 System. *Phys. Chem. Chem. Phys.* **2017**, *19* (36), 25071–25079. https://doi.org/10.1039/C7CP03816J.

(94) Rude, L. H.; Zavorotynska, O.; Arnbjerg, L. M.; Ravnsbæk, D. B.; Malmkjær, R. A.; Grove, H.; Hauback, B. C.; Baricco, M.; Filinchuk, Y.; Besenbacher, F.; Jensen, T. R. Bromide Substitution in Lithium Borohydride, $LiBH_4$–LiBr. *Int. J. Hydrogen Energy* **2011**, *36* (24), 15664–15672. https://doi.org/10.1016/j.ijhydene.2011.08.087.

(95) Hagemann, H.; Gomes, S.; Renaudin, G.; Yvon, K. Raman Studies of Reorientation Motions of $[BH_4]^-$ Anionsin Alkali Borohydrides. *J. Alloys Compd.* **2004**, *363* (1–2), 129–132. https://doi.org/10.1016/S0925-8388(03)00468-7.

(96) D'Anna, V.; Spyratou, A.; Sharma, M.; Hagemann, H. FT-IR Spectra of Inorganic Borohydrides. *Spectrochim. Acta Part A Mol. Biomol. Spectrosc.* **2014**, *128*, 902–906. https://doi.org/10.1016/j.saa.2014.02.130.

(97) Hagemann, H.; Filinchuk, Y.; Chernyshov, D.; Van Beek, W. Lattice Anharmonicity and Structural Evolution of $LiBH_4$: An Insight from Raman and X-Ray Diffraction Experiments. *Phase Transitions* **2009**, *82* (4), 344–355. https://doi.org/10.1080/01411590802707688.

(98) Rude, L. H.; Groppo, E.; Arnbjerg, L. M.; Ravnsbæk, D. B.; Malmkjær, R. A.;

Filinchuk, Y.; Baricco, M.; Besenbacher, F.; Jensen, T. R. Iodide Substitution in Lithium Borohydride, $LiBH_4$–LiI. *J. Alloys Compd.* **2011**, *509* (33), 8299–8305. https://doi.org/10.1016/j.jallcom.2011.05.031.

(99) Filinchuk, Y.; Chernyshov, D.; Cerny, R. Lightest Borohydride Probed by Synchrotron X-Ray Diffraction: Experiment Calls for a New Theoretical Revision. *J. Phys. Chem. C* **2008**, *112* (28), 10579–10584. https://doi.org/10.1021/jp8025623.

(100) Arnbjerg, L. M.; Ravnsbæk, D. B.; Filinchuk, Y.; Vang, R. T.; Cerenius, Y.; Besenbacher, F.; Jørgensen, J.-E.; Jakobsen, H. J.; Jensen, T. R. Structure and Dynamics for $LiBH_4$−LiCl Solid Solutions. *Chem. Mater.* **2009**, *21* (24), 5772–5782. https://doi.org/10.1021/cm902013k.

(101) Kumar, M.; Upadhyay, S. P. Pressure Dependence of Thermal Expansivity for Alkali Halides. *J. Phys. Chem. Solids* **1993**, *54* (6), 773–776. https://doi.org/10.1016/0022-3697(93)90140-M.

(102) El Kharbachi, A.; Nuta, I.; Hodaj, F.; Baricco, M. Above Room Temperature Heat Capacity and Phase Transition of Lithium Tetrahydroborate. *Thermochim. Acta* **2011**, *520* (1–2), 75–79. https://doi.org/10.1016/j.tca.2011.02.043.

(103) Hakansson, B.; Ross, R. G. Thermal Conductivity and Heat Capacity of Solid LiBr and RbF under Pressure. *J. Phys. Condens. Matter* **1989**, *1* (25), 3977–3985. https://doi.org/10.1088/0953-8984/1/25/009.

(104) J. Sangster, A. P. Phase Diagrams and Thermodynamic Properties of the 70 Binary Alkali Halide Systems Having Common Ions. *J. Phys. Chem. C* **1987**, *16*, 511–561.

(105) Oguchi, H.; Matsuo, M.; Hummelshøj, J. S.; Vegge, T.; Nørskov, J. K.; Sato, T.; Miura, Y.; Takamura, H.; Maekawa, H.; Orimo, S. Experimental and Computational Studies on Structural Transitions in the $LiBH_4$–LiI Pseudobinary System. *Appl. Phys. Lett.* **2009**, *94* (14), 141912. https://doi.org/10.1063/1.3117227.

(106) Shannon, R. D. Revised Effective Ionic Radii and Systematic Studies of Interatomic Distances in Halides and Chalcogenides. *Acta Crystallogr. Sect. A* **1976**, *32* (5), 751–767. https://doi.org/10.1107/S0567739476001551.

(107) Abrahams, S. C.; Kalnajs, J. The Lattice Constants of the Alkali Borohydrides and the Low-Temperature Phase of Sodium Borohydride. *J. Chem. Phys.* **1954**, *22* (3), 434–436. https://doi.org/10.1063/1.1740085.

(108) Černý, R.; Schouwink, P. The Crystal Chemistry of Inorganic Metal Boro-Hydrides and Their Relation to Metal Oxides. *Acta Crystallogr. Sect. B Struct. Sci. Cryst. Eng. Mater.* **2015**, *71*, 619–640. https://doi.org/10.1107/S2052520615018508.

(109) Pistorius, C. W. F. T. Melting and Polymorphism of $LiBH_4$ to 45 Kbar. *Z. Phys. Chem. Neue Folge* **1974**, *88*, 253–263.

(110) Tomkinson, J.; Waddington, T. C. Inelastic Neutron Scattering from the Alkali Metal Borohydrides and Calcium Borohydride. *J. Chem. Soc. Faraday Trans. 2* **1976**, *72*, 528. https://doi.org/10.1039/f29767200528.

(111) GharibDoust, S. H. P.; Brighi, M.; Sadikin, Y.; Ravnsbæk, D. B.; Černý, R.; Skibsted, J.; Jensen, T. R. Synthesis, Structure, and Li-Ion Conductivity of $LiLa(BH_4)_3X$, X = Cl, Br, I. *J. Phys. Chem. C* **2017**, *121* (35), 19010–19021. https://doi.org/10.1021/acs.jpcc.7b04905.

(112) Davies, P. K.; Navrotsky, A. Quantitative Correlations of Deviations from Ideality in Binary and Pseudobinary Solid Solutions. *J. Solid State Chem.* **1983**, *46* (1), 1–22. https://doi.org/10.1016/0022-4596(83)90122-6.

(113) Zavorotynska, O.; Corno, M.; Pinatel, E.; Rude, L. H.; Ugliengo, P.; Jensen, T. R.; Baricco, M. Theoretical and Experimental Study of $LiBH_4$-LiCl Solid Solution. *Crystals* **2012**, *2* (4), 144–158. https://doi.org/10.3390/cryst2010144.

(114) Morse, S. A. Binary Solutions and the Lever Rule Revisited. *J. Geol.* **1997**, *105* (4), 471–482. https://doi.org/10.1086/515940.

(115) Kraft, M. A.; Culver, S. P.; Calderon, M.; Böcher, F.; Krauskopf, T.; Senyshyn, A.; Dietrich, C.; Zevalkink, A.; Janek, J.; Zeier, W. G. Influence of Lattice Polarizability on the Ionic Conductivity in the Lithium Superionic Argyrodites Li_6PS_5X (X = Cl, Br, I). *J. Am. Chem. Soc.* **2017**, *139* (31), 10909–10918. https://doi.org/10.1021/jacs.7b06327.

(116) Krauskopf, T.; Pompe, C.; Kraft, M. A.; Zeier, W. G. Influence of Lattice Dynamics on Na^+ Transport in the Solid Electrolyte $Na_3PS_{4-x}Se_x$. *Chem. Mater.* **2017**, *29* (20), 8859–8869. https://doi.org/10.1021/acs.chemmater.7b03474.

(117) Martelli, P.; Remhof, A.; Borgschulte, A.; Ackermann, R.; Strässle, T.; Embs, J. P.; Ernst, M.; Matsuo, M.; Orimo, S.; Züttel, A. Rotational Motion in $LiBH_4$/LiI Solid Solutions. *J. Phys. Chem. A* **2011**, *115* (21), 5329–5334. https://doi.org/10.1021/jp201372b.

(118) Tilley, R. J. D. *Defects in Solids*, 10th ed.; John Wiley & Sons, Ed.; 2008.

(119) Altshuller, A. P. Lattice Energies and Related Thermodynamic Properties of the Alkali Metal Borohydrides and of the Borohydride Ion. *J. Am. Chem. Soc.* **1955**, *77* (21), 5455–5457. https://doi.org/10.1021/ja01626a001.

(120) Viščor, P. Comment on "Origin and Consequences of the Compensation (Meyer-Neldel) Law." *Phys. Rev. B* **2002**, *65* (7), 077201. https://doi.org/10.1103/PhysRevB.65.077201.

(121) Culver, S. P.; Koerver, R.; Krauskopf, T.; Zeier, W. G. Designing Ionic Conductors : The Interplay between Structural Phenomena and Interfaces in Thiophosphate-Based Solid-State Batteries. *7* (4). https://doi.org/10.1021/acs.chemmater.8b01293.

(122) Yelon, A.; Movaghar, B. Reply to "Comment on 'Origin and Consequences of the Compensation (Meyer-Neldel) Law' ." *Phys. Rev. B* **2002**, *65* (7), 077202. https://doi.org/10.1103/PhysRevB.65.077202.

(123) Yazami, R.; Universitaire, D. A Reversible Graphite-Lithium Electrochemical Generators. **1983**, *9*, 365–371.

(124) Turk, M. C.; Johnson, C. A.; Roy, D. Electroanalytical Evaluation of Temperature Dependent Electrolyte Functions for Lithium Ion Batteries : Investigation of Selected Mixed Carbonate Solvents Using a Lithium Titanate Electrode. *J. Energy Storage* **2018**, *20* (September), 395–408. https://doi.org/10.1016/j.est.2018.10.013.

(125) Friedrichs, O.; Remhof, A.; Hwang, S.-J.; Züttel, A. Role of $Li_2B_{12}H_{12}$ for the Formation and Decomposition of LiBH4. *Chem. Mater.* **2010**, *22* (10), 3265–3268. https://doi.org/10.1021/cm100536a.

(126) Chase, M. W. *NIST-JANAF Thermochemical Tables*, 4th editio.; [Washington, D.C.]: American Chemical Society, 1998.

(127) Fichtner, M. Nanoconfinement Effects in Energy Storage Materials. *Phys. Chem. Chem. Phys.* **2011**, *13* (48), 21186. https://doi.org/10.1039/c1cp22547b.

(128) Verkuijlen, M. H. W.; Ngene, P.; de Kort, D. W.; Barré, C.; Nale, A.; van Eck, E. R.

H.; van Bentum, P. J. M.; de Jongh, P. E.; Kentgens, A. P. M. Nanoconfined $LiBH_4$ and Enhanced Mobility of Li^+ and BH_4^- Studied by Solid-State NMR. *J. Phys. Chem. C* **2012**, *116* (42), 22169–22178. https://doi.org/10.1021/jp306175b.

(129) Suwarno; Ngene, P.; Nale, A.; Eggenhuisen, T. M.; Oschatz, M.; Embs, J. P.; Remhof, A.; De Jongh, P. E. Confinement Effects for Lithium Borohydride: Comparing Silica and Carbon Scaffolds. *J. Phys. Chem. C* **2017**, *121* (8), 4197–4205. https://doi.org/10.1021/acs.jpcc.6b13094.

(130) Dimitrov, V.; Sakka, S. Electronic Oxide Polarizability and Optical Basicity of Simple Oxides. I. *J. Appl. Phys.* **1996**, *79* (3), 1736–1740. https://doi.org/10.1063/1.360962.

(131) Brunauer, S.; Emmett, P. H.; Teller, E. Adsorption of Gases in Multimolecular Layers. *J. Am. Chem. Soc.* **1938**, *60* (2), 309–319. https://doi.org/10.1021/ja01269a023.

(132) Breuer, S.; Uitz, M.; Wilkening, H. M. R. Rapid Li Ion Dynamics in the Interfacial Regions of Nanocrystalline Solids. *J. Phys. Chem. Lett.* **2018**, *9* (8), 2093–2097. https://doi.org/10.1021/acs.jpclett.8b00418.

(133) Breuer, S.; Uitz, M.; Wilkening, H. M. R. Rapid Li Ion Dynamics in the Interfacial Regions of Nanocrystalline Solids. *J. Phys. Chem. Lett.* **2018**, *9* (8), 2093–2097. https://doi.org/10.1021/acs.jpclett.8b00418.

(134) Verdal, N.; Udovic, T. J.; Rush, J. J.; Liu, X.; Majzoub, E. H.; Vajo, J. J.; Gross, A. F. Dynamical Perturbations of Tetrahydroborate Anions in $LiBH_4$ Due to Nanoconfinement in Controlled-Pore Carbon Scaffolds. *J. Phys. Chem. C* **2013**, *117* (35), 17983–17995. https://doi.org/10.1021/jp4063737.

(135) Ngene, P.; Adelhelm, P.; Beale, A. M.; de Jong, K. P.; de Jongh, P. E. $LiBH_4$/SBA-15 Nanocomposites Prepared by Melt Infiltration under Hydrogen Pressure: Synthesis and Hydrogen Sorption Properties. *J. Phys. Chem. C* **2010**, *114* (13), 6163–6168. https://doi.org/10.1021/jp9065949.

(136) Indris, S.; Heitjans, P. Heterogeneous ^7Li NMR Relaxation in Nanocrystalline Li_2O:B_2O_3 Composites. *J. Non. Cryst. Solids* **2002**, *307–310* (3), 555–564. https://doi.org/10.1016/S0022-3093(02)01486-2.

(137) Wilkening, M.; Indris, S.; Heitjans, P. Heterogeneous Lithium Diffusion in Nanocrystalline Li_2O:Al_2O_3 Composites. *Phys. Chem. Chem. Phys.* **2003**, *5* (11), 2225–2231. https://doi.org/10.1039/b300908d.

(138) Indris, S.; Heitjans, P.; Roman, H. E.; Bunde, A. Nanocrystalline versus Microcrystalline Composites: Anomalous Ionic Conductivities and Percolation Theory. *Phys. Rev. Lett.* **2000**, *84* (13), 2889–2892. https://doi.org/10.1103/PhysRevLett.84.2889.

(139) Breuer, S.; Pregartner, V.; Lunghammer, S.; Wilkening, H. M. R. Dispersed Solid Conductors: Fast Interfacial Li-Ion Dynamics in Nanostructured LiF and LiF:γ-Al_2O_3 Composites. *J. Phys. Chem. C* **2019**, *123* (9), 5222–5230. https://doi.org/10.1021/acs.jpcc.8b10978.

(140) Epp, V.; Wilkening, M. Motion of Li^+ in Nanoengineered $LiBH_4$ and $LiBH_4$:Al_2O_3 Comparison with the Microcrystalline Form. *ChemPhysChem* **2013**, *14* (16), 3706–3713. https://doi.org/10.1002/cphc.201300743.

(141) Maier, J. Ionic Conduction in Space Charge Regions. *Prog. Solid State Chem.* **1995**, *23* (3), 171–263. https://doi.org/10.1016/0079-6786(95)00004-E.

(142) Ngene, P.; Lambregts, S. F. H.; Blanchard, D.; Vegge, T.; Sharma, M.; Hagemann, H.; de Jongh, P. E. The Influence of Silica Surface Groups on the Li-Ion Conductivity of $LiBH_4/SiO_2$ Nanocomposites. *Phys. Chem. Chem. Phys.* **2019**, *21* (40), 22456–22466. https://doi.org/10.1039/c9cp04235k.

(143) Barzan, C.; Groppo, E.; Bordiga, S.; Zecchina, A. Defect Sites in H_2-Reduced TiO_2 Convert Ethylene to High Density Polyethylene without Activator. *ACS Catal.* **2014**, *4* (3), 986–989. https://doi.org/10.1021/cs500057s.

(144) Kim, K. H.; Oh, E. J.; Choi, J. S. Electrical Conductivity of “Hydrogen-Reduced” Titanium Dioxide (Rutile). *J. Phys. Chem. Solids* **1984**, *45* (11–12), 1265–1269. https://doi.org/10.1016/0022-3697(84)90026-X.

(145) Surplice, N. A. The Electrical Conductivity of Calcium and Strontium Oxides. *Br. J. Appl. Phys.* **1966**, *17* (2), 175–180. https://doi.org/10.1088/0508-3443/17/2/303.

(146) Groner, M. D.; Elam, J. W.; Fabreguette, F. H.; George, S. M. Electrical Characterization of Thin Al_2O_3 Films Grown by Atomic Layer Deposition on Silicon and Various Metal Substrates. *Thin Solid Films* **2002**, *413* (1–2), 186–197. https://doi.org/10.1016/S0040-6090(02)00438-8.

(147) Yao, Z.; Kim, S.; Michel, K.; Zhang, Y.; Aykol, M.; Wolverton, C. Stability and Conductivity of Cation- and Anion-Substituted $LiBH_4$-Based Solid-State Electrolytes. *Phys. Rev. Mater.* **2018**, *2* (6), 37–39. https://doi.org/10.1103/PhysRevMaterials.2.065402.

(148) Zettl, R.; de Kort, L.; Gombotz, M.; Wilkening, H. M. R.; de Jongh, P. E.; Ngene, P. Combined Effects of Anion Substitution and Nanoconfinement on the Ionic Conductivity of Li-Based Complex Hydrides. *J. Phys. Chem. C* **2020**, *124* (5), 2806–2816. https://doi.org/10.1021/acs.jpcc.9b10607.

(149) Zettl, R.; Gombotz, M.; Clarkson, D.; Greenbaum, S. G.; Ngene, P.; de Jongh, P. E.; Wilkening, H. M. R. Li-Ion Diffusion in Nanoconfined $LiBH_4$-LiI/Al_2O_3: From 2D Bulk Transport to 3D Long-Range Interfacial Dynamics. *ACS Appl. Mater. Interfaces* **2020**, *12* (34), 38570–38583. https://doi.org/10.1021/acsami.0c10361.

(150) Duchêne, L.; Lunghammer, S.; Burankova, T.; Liao, W. C.; Embs, J. P.; Copéret, C.; Wilkening, H. M. R.; Remhof, A.; Hagemann, H.; Battaglia, C. Ionic Conduction Mechanism in the $Na_2(B_{12}H_{12})_{0.5}(B_{10}H_{10})_{0.5}$ Closo-Borate Solid-State Electrolyte: Interplay of Disorder and Ion-Ion Interactions. *Chem. Mater.* **2019**, *31* (9), 3449–3460. https://doi.org/10.1021/acs.chemmater.9b00610.

(151) Okada, Y.; Ikeda, M.; Aniya, M. Non-Arrhenius Ionic Conductivity in Solid Electrolytes: A Theoretical Model and Its Relation with the Bonding Nature. *Solid State Ionics* **2015**, *281*, 43–48. https://doi.org/10.1016/j.ssi.2015.08.020.

(152) Zhao, W.; Yi, J.; He, P.; Zhou, H. Solid-State Electrolytes for Lithium-Ion Batteries: Fundamentals, Challenges and Perspectives. *Electrochem. Energy Rev.* **2019**, *2* (4), 574–605. https://doi.org/10.1007/s41918-019-00048-0.

(153) Gulino, V.; Wolczyk, A.; Golov, A. A.; Eremin, R. A.; Palumbo, M.; Nervi, C.; Blatov, V. A.; Proserpio, D. M.; Baricco, M. Combined DFT and Geometrical–Topological Analysis of Li-Ion Conductivity in Complex Hydrides. *Inorg. Chem. Front.* **2020**, *7* (17), 3115–3125. https://doi.org/10.1039/D0QI00577K.

(154) Goodenough, J. B. Oxide-Ion Electrolytes. *Annu. Rev. Mater. Res.* **2003**, *33* (1), 91–128. https://doi.org/10.1146/annurev.matsci.33.022802.091651.

(155) Chen, C.; Guo, X. Space Charge Layer Effect in Solid State Ion Conductors and

Lithium Batteries: Principle and Perspective. *Acta Chim. Slov.* **2016**, 489–495. https://doi.org/10.17344/acsi.2016.2286.

(156) Maier, J. Ionic Conduction in Space Charge Regions. *Prog. Solid State Chem.* **1995**, *23* (3), 171–263. https://doi.org/10.1016/0079-6786(95)00004-E.

(157) Lambregts, S. F. H.; van Eck, E. R. H.; Suwarno; Ngene, P.; de Jongh, P. E.; Kentgens, A. P. M. Phase Behavior and Ion Dynamics of Nanoconfined $LiBH_4$ in Silica. *J. Phys. Chem. C* **2019**, *123* (42), 25559–25569. https://doi.org/10.1021/acs.jpcc.9b06477.

(158) Brighi, M.; Murgia, F.; Łodziana, Z.; Schouwink, P.; Wołczyk, A.; Cerny, R. A Mixed Anion Hydroborate/Carba-Hydroborate as a Room Temperature Na-Ion Solid Electrolyte. *J. Power Sources* **2018**, *404* (August), 7–12. https://doi.org/10.1016/j.jpowsour.2018.09.085.

(159) Sakamoto, J. More Pressure Needed. *Nat. Energy* **2019**, *4* (10), 827–828. https://doi.org/10.1038/s41560-019-0478-z.

(160) Wang, M. J.; Choudhury, R.; Sakamoto, J. Characterizing the Li-Solid-Electrolyte Interface Dynamics as a Function of Stack Pressure and Current Density. *Joule* **2019**, *3* (9), 2165–2178. https://doi.org/10.1016/j.joule.2019.06.017.

(161) Goodenough, J. B.; Kim, Y. Challenges for Rechargeable Li Batteries †. *Chem. Mater.* **2010**, *22* (3), 587–603. https://doi.org/10.1021/cm901452z.

(162) Goodenough, J. B.; Singh, P. Review—Solid Electrolytes in Rechargeable Electrochemical Cells. *J. Electrochem. Soc.* **2015**, *162* (14), A2387–A2392. https://doi.org/10.1149/2.0021514jes.

(163) Schnell, J.; Günther, T.; Knoche, T.; Vieider, C.; Köhler, L.; Just, A.; Keller, M.; Passerini, S.; Reinhart, G. All-Solid-State Lithium-Ion and Lithium Metal Batteries – Paving the Way to Large-Scale Production. *J. Power Sources* **2018**, *382* (December 2017), 160–175. https://doi.org/10.1016/j.jpowsour.2018.02.062.

(164) Sharafi, A.; Meyer, H. M.; Nanda, J.; Wolfenstine, J.; Sakamoto, J. Characterizing the Li–$Li_7La_3Zr_2O_{12}$ Interface Stability and Kinetics as a Function of Temperature and Current Density. *J. Power Sources* **2016**, *302*, 135–139. https://doi.org/10.1016/j.jpowsour.2015.10.053.

(165) Kasemchainan, J.; Zekoll, S.; Spencer Jolly, D.; Ning, Z.; Hartley, G. O.; Marrow, J.; Bruce, P. G. Critical Stripping Current Leads to Dendrite Formation on Plating in Lithium Anode Solid Electrolyte Cells. *Nat. Mater.* **2019**, *18* (10), 1105–1111. https://doi.org/10.1038/s41563-019-0438-9.

(166) Dahn, J.; Haering, R. R. Lithium Intercalation in TiS2. *Mater. Res. Bull.* **1979**, *14* (10), 1259–1262. https://doi.org/10.1016/0025-5408(79)90002-3.

(167) Dahn, J. R.; McKinnon, W. R.; Haering, R. R.; Buyers, W. J. L.; Powell, B. M. Structure Determination of Li_xTiS_2 by Neutron Diffraction. *Can. J. Phys.* **1980**, *58* (2), 207–213. https://doi.org/10.1139/p80-033.

(168) Dahn, J. R.; Haering, R. R. Anomalous Bragg Peak Widths in Li_xTiS_2. *Solid State Commun.* **1981**, *40* (3), 245–248. https://doi.org/10.1016/0038-1098(81)90750-X.

(169) Yan, Y.; Rentsch, D.; Battaglia, C.; Remhof, A. Synthesis, Stability and Li-Ion Mobility of Nanoconfined $Li_2B_{12}H_{12}$. *Dalt. Trans.* **2017**, *46* (37), 12434–12437. https://doi.org/10.1039/c7dt02946b.

(170) Krauskopf, T.; Hartmann, H.; Zeier, W. G.; Janek, J. Toward a Fundamental Understanding of the Lithium Metal Anode in Solid-State Batteries - An

Electrochemo-Mechanical Study on the Garnet-Type Solid Electrolyte $Li_{6.25}Al_{0.25}La_3Zr_2O_{12}$. *ACS Appl. Mater. Interfaces* **2019**, *11* (15), 14463–14477. https://doi.org/10.1021/acsami.9b02537.

(171) Krauskopf, T.; Mogwitz, B.; Rosenbach, C.; Zeier, W. G.; Janek, J. Diffusion Limitation of Lithium Metal and Li–Mg Alloy Anodes on LLZO Type Solid Electrolytes as a Function of Temperature and Pressure. *Adv. Energy Mater.* **2019**, *9* (44). https://doi.org/10.1002/aenm.201902568.

(172) Rodrigues, M.-T. F.; Sayed, F. N.; Gullapalli, H.; Ajayan, P. M. High-Temperature Solid Electrolyte Interphases (SEI) in Graphite Electrodes. *J. Power Sources* **2018**, *381* (January), 107–115. https://doi.org/10.1016/j.jpowsour.2018.01.070.

(173) Bruce, P. G.; Freunberger, S. A.; Hardwick, L. J.; Tarascon, J.-M. Li–O_2 and Li–S Batteries with High Energy Storage. *Nat. Mater.* **2012**, *11* (1), 19–29. https://doi.org/10.1038/nmat3191.

(174) Murgia, F.; Brighi, M.; Černý, R. Room-Temperature-Operating Na Solid-State Battery with Complex Hydride as Electrolyte. *Electrochem. commun.* **2019**, *106* (July), 106534. https://doi.org/10.1016/j.elecom.2019.106534.

(175) Duchêne, L.; Kim, D. H.; Song, Y. B.; Jun, S.; Moury, R.; Remhof, A.; Hagemann, H.; Jung, Y. S.; Battaglia, C. Crystallization of Closo-Borate Electrolytes from Solution Enabling Infiltration into Slurry-Casted Porous Electrodes for All-Solid-State Batteries. *Energy Storage Mater.* **2020**, *26*, 543–549. https://doi.org/10.1016/j.ensm.2019.11.027.

(176) Doux, J.; Nguyen, H.; Tan, D. H. S.; Banerjee, A.; Wang, X.; Wu, E. A.; Jo, C.; Yang, H.; Meng, Y. S. Stack Pressure Considerations for Room-Temperature All-Solid-State Lithium Metal Batteries. *Adv. Energy Mater.* **2020**, *10* (1), 1903253. https://doi.org/10.1002/aenm.201903253.

(177) Sendek, A. D.; Cheon, G.; Pasta, M.; Reed, E. J. Quantifying the Search for Solid Li-Ion Electrolyte Materials by Anion: A Data-Driven Perspective. *J. Phys. Chem. C* **2020**, *124* (15), 8067–8079. https://doi.org/10.1021/acs.jpcc.9b10650.

(178) McCloskey, B. D. Attainable Gravimetric and Volumetric Energy Density of Li–S and Li Ion Battery Cells with Solid Separator-Protected Li Metal Anodes. *J. Phys. Chem. Lett.* **2015**, *6* (22), 4581–4588. https://doi.org/10.1021/acs.jpclett.5b01814.

(179) Unemoto, A.; Matsuo, M.; Orimo, S. I. Complex Hydrides for Electrochemical Energy Storage. *Adv. Funct. Mater.* **2014**, *24* (16), 2267–2279. https://doi.org/10.1002/adfm.201303147.

(180) Brighi, M.; Murgia, F.; Černý, R. Closo-Hydroborate Sodium Salts as an Emerging Class of Room-Temperature Solid Electrolytes. *Cell Reports Phys. Sci.* **2020**, 100217. https://doi.org/10.1016/j.xcrp.2020.100217.

(181) Brighi, M.; Murgia, F.; Łodziana, Z.; Schouwink, P.; Wołczyk, A.; Cerny, R. A Mixed Anion Hydroborate/Carba-Hydroborate as a Room Temperature Na-Ion Solid Electrolyte. *J. Power Sources* **2018**, *404* (August), 7–12. https://doi.org/10.1016/j.jpowsour.2018.09.085.